Nanosynthesis of Iron Based Material for Green Energy

By

Alec W. Kirkeminde

Submitted to the graduate degree program in Chemistry and the Graduate Faculty of the University of Kansas in partial fulfillment of the requirements for the degree of Doctor of Philosophy.

_____

Chair Person Shenqiang Ren, PhD, Assistant Professor

_____

Mikhail V. Barybin, PhD, Professor

_____

Ward H. Thompson, PhD, Professor

_____

Robert C. Dunn, PhD, Professor

_____

Judy Z. Wu, PhD, University Distinguished Professor

Date Defended: 4-2-15

The Dissertation Committee for Alec W. Kirkeminde

certifies that this is the approved version of the following dissertation:

Nanosynthesis of Iron Based Material for Green Energy

_____

Chairperson Shenqiang Ren, PhD, Assistant Professor

Date approved: 4-2-15

Abstract

In this work, nanosynthesis of multiple iron-based materials are explored to further their use in green renewable-energy applications. First, the nanosynthesis of the abundant, non-toxic semi-conductor Iron Disulfide (Iron Pyrite, Fool's Gold, FeS_2) is investigated. Within these studies, it became possible to tune the shape of the FeS_2 nanoparticles easily by modifying injection temperatures and iron precursors. From here, the growth mechanisms of the different shapes were elucidated by examining different time points within the synthesis. It was discovered that the FeS_2 did not grow by Ostwald Ripening, but instead by Oriented Attachment. Knowing this, it was possible to not only further the shapes of FeS_2 nanoparticles, but also manipulate the size and crystallinity. Focus was then shifted to creating larger micron sized FeS_2 crystals. Larger crystals where achieved by a unique FeS nanowire precursor followed by sulfurization. The dominant crystal surface of these crystals could be regulated simply by the time and temperature of the sulfurization.

Second, synthetic control of magnetic nanoparticles was examined. A novel synthesis of Iron Palladium (FePd) made possible by interdiffusion of iron into palladium nanocores was identified. Furthermore, a shell of Iron oxide (Fe_2O_3) could facilely be grown on the FePd nanoparticles, generating a FePd/Fe_2O_3 core/shell nanoparticle. These FePd/Fe_2O_3 core/shell particles provided an excellent foundation to create an $L1_0$-FePd/α-Fe exchange-coupled nanocomposite that exhibited improved magnetic properties compared to its single phase FePd counterpart. However, the stabilizing ligand used within this FePd synthesis doped into the final nanoparticles, degraded the magnetic properties.

To overcome the dopant ligand problem, a novel nanoalloy synthetic strategy of Metal Redox was developed. The Metal Redox strategy utilized the inherent reducing power of zero-valent metal sources to create a vast sampling of metal nanoalloys without the need of ligands or excess reducing agents. Stoichiometry of these nanoalloys could be readily adjusted by temperature and explained by simple chemical equilibrium concepts. The Metal Redox methodology was then expanded to shape control and tri-metallic alloys. Finally, the unique MnBi nanoalloy system was created using Metal Redox, making it the first ever reported solution processed formation of this material.

Acknowledgements

First and foremost I want to thank my fiancé Cara Katzer for the never-ending support she has provided over the past years. For without her, none of this would have occurred. I would also like to thank my family for their encouraging words and praise I have received throughout.

I would like to thank Dr. Ren for the freedom and support he has provided me during my research time at Kansas University. Thank you for always being available and teaching me that failed results are not always useless and that there is always something to learn from it. The Ren group members also deserve recognition and thanks. My fellow graduate students, Jessica and Dan have been clever sounding boards for many different topics over the years. Dr. Maogang Gong, a post-doc in the Ren group, deserves recognition for his assistance in many different parts of my projects, and I thank him for his eagerness to always help.

Many thanks to the professors that I have had the opportunity to work with here at KU. I would like to especially thank both Dr. Ward Thompson and Dr. Mikhail V. Barybin. Dr. Thompson was always available to help simplify even the most complex subjects to me, and provided wisdom throughout my training. Dr. Barybin showed me that it is ok to not be right immediately, and that small steps from basic knowledge can quickly build.

The MAI lab at KU deserve recognition, especially Heather Shinogle, The staff have been key in training me in the many different electron microscopes, which was instrumental to my research. I also want to thank Dr. Victor Day for always making time

for me on the x-ray diffraction instrument. I always looked forward to our discussions during data acquirement.

Finally, I need to thank my friends for their support throughout the years. They were always there to help me relax. I would like to thank Dr. Jeffery Lange for his insight on many different science topics, and always willing to question my conclusions, challenging me to become a better scientist in the process.

List of Abbreviations

Acetylacetonate – Acac
Activation Energy – E_a
Atomic Number – Z
Chemical Vapor Deposition – CVD
Coercivity – H_c
Crystalline Silicon – C-Si
Cyclooctadiene – COD
Energy Dispersive Spectroscopy – EDS
Enthalpy – H
Entropy – S
Equilibrium Constant - K_{eq}
Fast Fourier Transform – FFT
Gas Constant – R
Gibbs Free Energy - G
Hard/Soft Acid-base – HSAB
Hexafluoroacetylacetone – Hfac
High Resolution Transmission Electron Microscope – HRTEM
Inductively Coupled Plasma Atomic Emission Spectroscopy – ICP-AES
Magnetic Energy Product – $(BH)_{max}$
Magnetic Hysteresis – M-H
Magnetic Saturation – M_s
Magnetocrystalline Anisotropy Constant – K_u
Metal Organic Chemical Vapor Deposition – MOCVD
Near Infrared – NIR
Octadecene – ODE
Octadecylamine – ODA
Oriented Attachment – OA
Power Conversion Efficiency – PCE
Quantum Dots – QD
Rare Earth – RE
Rotation Per Minute – RPM
Scanning Electron Microscope – SEM
Scanning Transmission Electron Microscope – STEM
Temperature – T
Time - t
Transmission Electron Microscope – TEM
Tributylphosphine – TBP
Trioctalphosphine Oxide – TOPO
Turn Over Frequency – TOF
Ultra-Violet/Visible – Uv-Vis
Vibrating Sample Magnetometer – VSM
Wavelength – λ
X-Ray Diffraction – XRD
X-Ray Photoelectron Spectroscopy – XPS

Table of Contents

1 Introduction

1.1 Goals

The all-encompassing goal of this dissertation is to expand the knowledge of the synthesis of nanoparticles containing the earth-abundant element Iron (Fe) for uses in energy-critical applications. Within this considerably broad goal, there are two main focuses that I have attempted to expand upon. First, the nanosynthesis of the semi-conductor Iron Disulfide (Pyrite, Fool's Gold, FeS_2) is explored in order to control shape and morphology. Crystal growth mechanisms are then carefully studied both in solution based processing and solid-state. Secondly, new developments in magnetic metal nanoparticle synthesis are explored. These include creating novel iron based core-shell magnetic nanoparticles via standard nanoparticle synthetic methods, and then comparing their magnetic properties to their single-phase counterparts. Slight deviation from standard methods then lead into the development of a completely new methodology for the generation of zero-valent nanoalloy structures. Finally, this novel synthetic strategy is further developed resulting in easily generated unique structures and nanoalloys that are unique to this new technique.

1.2 World's Energy Needs and Renewable Energy

Renewable energy is classified as energy that will not run out and which will meet the needs for future generations. Within renewable energy generation, it is necessary that the capture and use of the energy also does not produce greenhouse gases or pollutants. The world consumes around 380 exajoules (1 EJ = 10^{18} J) a year. This is a staggering amount of energy that needs to be created to meet demands. The Earth's population continues to grow and energy must be available to grow with it. At this time, almost 80%

of the World energy supply is generated from fossil fuels, as seen in Figure 1.[1] Only ~13.5% of this energy is generated by renewable sources. Removing traditional biomass generation, only 3.4% is being utilized to provide the Earth's energy. The European Union has even predicted by the year 2030 that renewable energy sources will not keep pace with demands, and even less energy will be generated by these methods. It is obvious that these energy-critical renewable sources must be improved to allow for growth and economically feasibility to fulfill the Earth's energy demands.

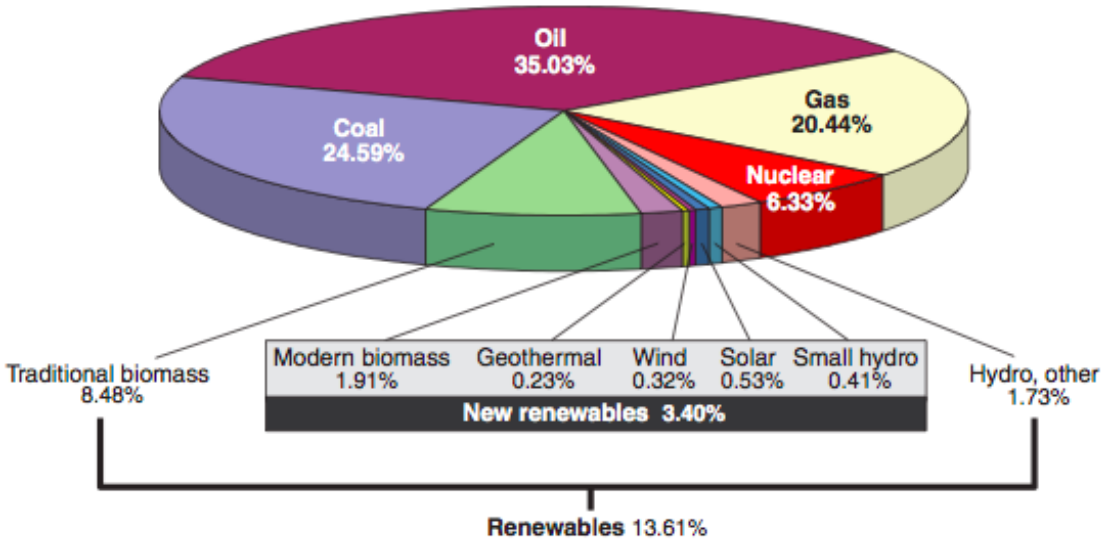

Figure 1. Pie chart of the sources of the Earth's energy generation. Reprinted with permission from [1].

1.2.1 Solar Cell Energy Generation

Solar cells, or photovoltaic devices, provide a promising source of renewable energy. These devices make use of the photovoltaic effect where the active material absorbs light exciting an electron within the material to an excited state, leaving behind a hole. Both of these charges can then be forced to move throughout the material,

generating electrical current. The material used for solar cells must be a semiconductor with a band gap that matches the solar spectrum. The forerunner and most utilized solar cell semi-conductor material is silicon. Crystalline silicon (C-Si) devices have been comprehensively studied over the previous decades, making up most of the solar cell devices in use today. Even with highly crystalline material, a maximum of ~28% of the sunlight's energy can be transformed to electricity. Commercial cells show even lower efficiencies, ~15-20%.[2] The reduction in efficiency is a result of the lower crystallinity within the commercial cells. High crystallinity Si creation is very energy intensive, making it economically unfeasible to make use of the ~28% cells that can be generated. Moreover, Silicon has a band gap of 1.1 eV, which corresponds to the infrared region of light. Any light over this energy can still be absorbed, but the excess energy of the photon is converted to heat instead of current. To compound these issues, C-Si is a very poor light absorber, requiring a thick active layer, increasing the total cost. These problems have kept solar energy more expensive than conventional methods. Recently, perovskite solar cells have seen tremendous gains in efficiencies, from 3.8% in 2009 to 20.1% in 2014.[3] However, work is still required to commercialize these devices and many of the perovskites contain lead, leading to worries about leeching. Many other semiconducting materials have been proposed and examined for replacing C-Si including CdS, CdSe, CdTe and $CuInSe_2$.[4] These semiconductors possess higher absorption coefficients and reasonable band gaps, but have not been mass-produced. This is due the toxic elements associated with these materials, which makes them impractical to use on a large scale. Thus, it will be extremely beneficial to develop a green semi-conductor material with a

high absorption coefficient that is cheaply obtained, non-toxic, and can be easily scaled up for production.

1.2.2 Wind Energy Generation

About 2% of the Sun's energy imparted onto the Earth is converted to wind energy. This equates to about 300 EJ yearly, however only 0.05% of this energy is being captured.[2] Windmills make use of turbines converting the kinetic energy of the wind into electricity by rotation of magnets around a metal coil. However, the blades of the windmill spin at 10-20 rotations per minute (RPMs) at peak times. Such low RPMs cannot be used in the standard induction generators, as they require ~1000 RPMS to operate. Therefore, a gearbox is required behind the slow moving turbine to yield the proper RPMS. Not only is energy lost by this conversion process, these gearboxes are the main source of failure within the systems.[5] Removing these gearboxes would increase the lifetime and reduce the loss of energy of the wind turbine. Recently, companies such as General Motors have been moving toward direct drive permanent magnet turbines, which make use of larger magnets to eliminate the need for the gearboxes. To increase the amount of current generated in these turbines there are two methods. First is to increase the speed of the magnet's rotation around the coil. Second is to increase the magnetic flux. To increase the rotation speed, the radius of rotation can be increased. However, there is a practical limitation to the size of the radius used in the turbine. To increase the magnetic flux, strong magnets must be used. However, there are many different magnetic materials out there and the proper magnets must be chosen.

To determine the type of magnets to be used, one must know the properties of a magnetic system. The most standard way to examine a material's magnetic property is by

measuring a magnetic hysteresis loop (M-H), as shown in Figure 2. These measurements are done on a Vibrating Sample Magnetometer (VSM) where a magnetic sample is placed into a uniform magnetic field and then vibrated, generating a voltage within nearby pickup coils. This induced voltage is directly related to the sample's magnetic moment, which can be determined by calibration to a known magnetic sample. Sweeping the magnetic field applied (usually done by large electromagnets) with a constant vibration, a hysteresis loop can be generated. On the Y-axis of the measurement is magnetization, M, (units of emu or emu/g) of the sample material at variable applied field strength, H (x-axis, units of Oe). Within the hysteresis loop, different material characteristics can be determined at specific points. A typical measurement is performed beginning with a demagnetized sample with no field. A field is then applied and ramped until the sample reaches its magnetic saturation (M_s), where all the domains are aligned within the material. Then the field is swept backwards until saturation is reached in the negative applied field, where the domains are aligned in the opposite direction. The point where the line crosses the Y-axis is called the remanence. Where the loop crosses the X-axis is called the coercivity (H_c) of the material, which is how much applied magnetic field is required to completely demagnetize the sample. The M-H loop provides large amounts of valuable information about magnetism of materials and is a standard in the magnetic materials field.

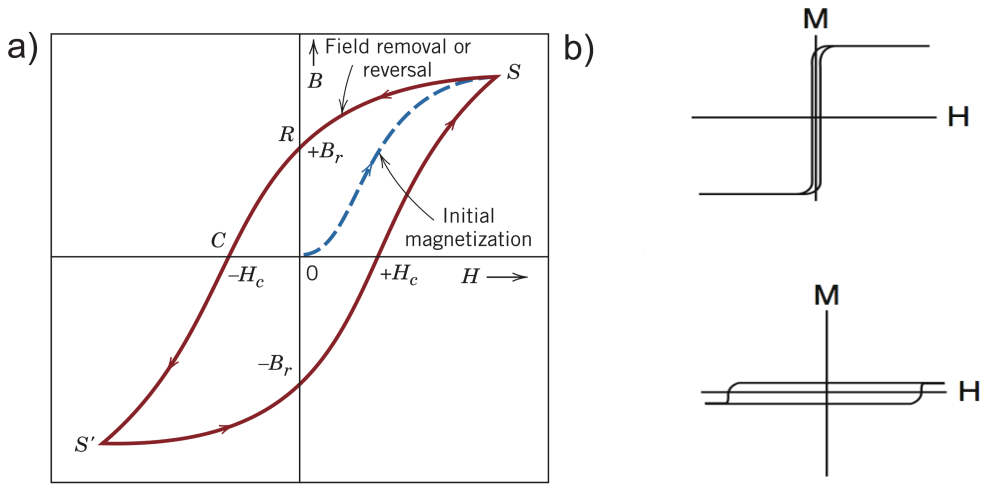

Figure 2. a) Example hysteresis curve with components labeled. B and H are magnetization and applied magnetic field. Points S, R, C are the Magnetic Saturation, Magnetic Remanence and Coercivity of the magnetic samples respectively. b) Comparative hysteresis loops between soft (top) and hard (bottom) magnets. Figure adapted with permission of [6, 7].

There are two subtypes of magnet classification, one termed soft, and the other hard. Soft magnets have low H_c, meaning they are simple to demagnetize, and high M_s. These types of magnets are utilized in applications where switching of magnetic fields is rapid, and energy loss is small. An example of such an application is the magnetic cores in transformers. Examples of soft magnetic materials include pure metals (Co^0, Ni^0, Fe^0), bimetallic alloys (FeNi, FeCo) and many different cubic ferrites (FeO, Fe_2O_3). On the other side of the spectrum are hard magnetic materials. These materials have high H_c, making them difficult to demagnetize. Material that exhibit high magnetocrystalline anisotropy constants (K_u, J/m^3) make up hard magnetic materials. Some standard hard metal systems include $BaO\text{-}6Fe_2O_3$, MnBi, $L1_0$-FePt, $L1_0$-FePd. These have high H_c but

exhibit much smaller M_s than their soft magnet counterparts. To compare different hard magnetic materials, an energy product is defined ($(BH)_{max}$) as the area of the largest rectangle that can be constructed in the second quadrant of the M-H loop. This $(BH)_{max}$ is usually quoted in units of Mega-Gauss*Oersted (MGOe), but can be converted to SI units by the relationship of 1 MGOe = 7.96 kJ/m^3. For high energy permanent magnets, both high M_s and high H_c are desired, as it will increase the $(BH)_{max}$. Magnets having a $(BH)_{max}$ over 10 MGOe are classified as high-energy magnetic systems. These systems include the magnetic alloys $SmCo_5$, and $Nd_2Fe_{14}B$. The turbines mentioned above make use of the rare earth (RE) based neodymium iron boron ($Nd_2Fe_{14}B$) permanent magnets. Around ~2,000 kg of $Nd_2Fe_{14}B$ are needed in these new direct drive generators, thus requiring high amounts of RE these generators. Development of useful applications that these required RE elements becomes an issue due to the United States having very low production of them and must import most of the raw material. RE elements, unlike their name suggests, are not that rare within the Earth's crust.

Figure 3 presents a list of many of the RE elements and their crustal abundance in parts per million (ppm). For reference, Neodymium (Nd) has a crustal abundance of 41.5 ppm, which is much higher than gold (0.004 ppm), silver (0.075 ppm) and even lead (14 ppm).[8] Although the RE's have high abundance within the earth's crust, there are no concentrated sources to mine effectively. This makes mining and purification of RE elements too costly to be economically feasible in most areas. In fact, only one mine in the United States is actively producing the raw material for RE element purifications. Due to this, the United States imports almost all of its RE supplies, and 93% is exported

from China. In fact, 95% of the RE global market comes from China. Recently China has slowed the export of RE to the rest of the world due to new taxes and limits instated.[9]

Element	Symbol	Atomic number	Crustal abundance
Light REEs			
Lanthanum	La	57	39
Cerium	Ce	58	66.5
Praseodymium	Pr	59	9.2
Neodymium	Nd	60	41.5
Samarium	Sm	62	7.05
Europium	Eu	63	2.0
Gadolinium	Gd	64	6.2
Heavy REEs			
Terbium	Tb	65	1.2
Dysprosium	Dy	66	5.2
Holmium	Ho	67	1.3
Erbium	Er	68	3.5
Thulium	Tm	69	0.52
Ytterbium	Yb	70	3.2
Lutetium	Lu	71	0.8
Yttrium	Y	39	33

Figure 3. List of RE elements crustal abundance in parts per million. Reproduced with permission of [9]

To reduce the dependence on foreign countries, research and development of strong magnets has seen a paradigm shift, moving to magnetic systems that employ materials other than RE elements. The ultimate goal becomes to create magnets that are both powerful and inexpensive with abundant and non-toxic elements.

1.2.3 The Promise of Nanoparticles

Within recent years, an explosion of research on nanoparticles has been observed. Interest in nanoparticles has spilled into many scientific disciplines due to unique properties of materials seen at the nanometer scale. But how can nanoparticles be used in helping improve green energy generation? In the case of solar cells, there are many

benefits to nanoparticles. First and foremost, the ability to tune the band gap of semi-conducting nanoparticles is easily the most promising aspect.[10] Being able to tune the band gap of a single material allows for precise control of light absorbed, unlike in bulk where only one band gap is achievable. However, band gap tuning is not the only benefit of semi-conducting nanoparticles. Synthesis of nanoparticles is almost exclusively achieved by solution processing. Solution processing allows for cheaper creation than more energy intensive thin film creations such as high vacuum deposition systems.[11] Solution processing affords the ability to create thin films through spin coating, dip coating, and inkjet printing reducing overall costs of film creations. These methods can also be easily transferable to flexible substrates, allowing for more mobile devices. Nanoparticles have found use in sensitizers in hybrid polymer solar cells to extend the wavelengths the devices function at.[12-14] Pure inorganic solar cells have been created utilizing single-phase Schottky devices, as well donor-acceptor material pairs.[15-18] Nanoparticles have even replaced the dye of dye-sensitized solar cells.[19-21] However, with such promise of nanoparticles, there are drawbacks. Almost all of the extensively studied nanoparticles are made with toxic elements, including Cd, Pb, As. Subjecting these toxic elements to extreme conditions, as in solar cells, leads to worries of leaching. It would, therefore, be immensely valuable to find an inexpensive green semiconductor that can selectively highlight the positive aspects provided by standard nanoparticle processing, without the drawbacks of including a toxic element.

Solar cells are not the only application to benefit from the unique nanosized properties nanoparticles provide. Nanoscale magnetic materials are featured in many applications such as high-density data storage, spintronics, and biomedical imaging.[22-24]

However, more importantly for green energy applications is the possibility of manipulation of the material's magnetic properties on the nanoscale. The size of a magnetic particle is seen to affect the strength of magnetic properties. With the potential to alter the size, the quality of permanent magnets can be improved when compared to their bulk counterparts.[25] Furthermore, increases in magnetic attributes can be created by well controlled two-phase magnetic nanocomposites.[26] Nanocomposites can yield increases up to 40% in magnetic properties, when compared to the single phased analogue and without the use of RE elements.[27] Not only do the magnetic properties increase, these nanoparticles also gain the benefit of solution processing like their semi-conducting counterparts. Control of self-assembly of particles and phase deposition through simple dip coating or drop casting can prove an easier method than energy intensive layer by layer thin film deposition methods. Indeed, the field of magnetism has seen benefits to its timely merge with nanosynthesis. With this coupling of promising traits, it could be possible to generate new permanent magnets that can help lessen the need for RE based magnets.

In the following section, the growth and control of nanoparticles will be explored, followed by sections dedicated to semi-conductor nanoparticles and their synthesis. Metal nanoparticle synthesis will receive its own discussion subsequently.

1.3 Colloidal Nucleation and Growth: Basics of Nanoparticle Synthesis

Before the two main focuses of the goals are tackled, introduction into how nanoparticles are formed and controlled must be examined. Generation of nanoparticles may seem very complex with the many different methodologies that have arisen from the explosion of nanosynthesis, but in reality all nanoparticle generation can be ultimately

related back to basic colloidal generation. LaMer and Dinegar are routinely cited as the first to explore generation of colloids, where they developed a theory that is ultimately still used today.[28] It was found that to form colloids, a nucleation event must occur. Studying sulfur colloids in a super saturated condition; it was found that once a certain supersaturation level was reached, a nucleation event occurred producing initial nuclei relieving the supersaturation. Growth phase follows with monomer addition from solution onto these starting "seeds". Figure 4a displays a graphical representation of LaMer theory of colloidal growth. In the case of semiconductor and metal nanoparticles a nucleation event is usually generated with what is termed a hot-injection to instantaneously reach the supersaturation concentration. In this procedure, one or both precursors are rapidly injected into a heated solution of coordinating ligands, causing rapid super-saturation while simultaneously cooling the reaction, initiating a nucleation event. The coordinating ligands are used to stabilize the seeds by coordinating to the surface, helping control the crystal growth and allow the particles to stay solvated. Such a hot-injection apparatus is shown in Figure 4b. The seed particles size is ultimately affected by the time spent within the initial nucleation window, above the nucleation threshold. Short bursts create tight nucleation curves and therefore monodisperse seeds, whereas longer nucleation windows allow for nucleation events to occur at different

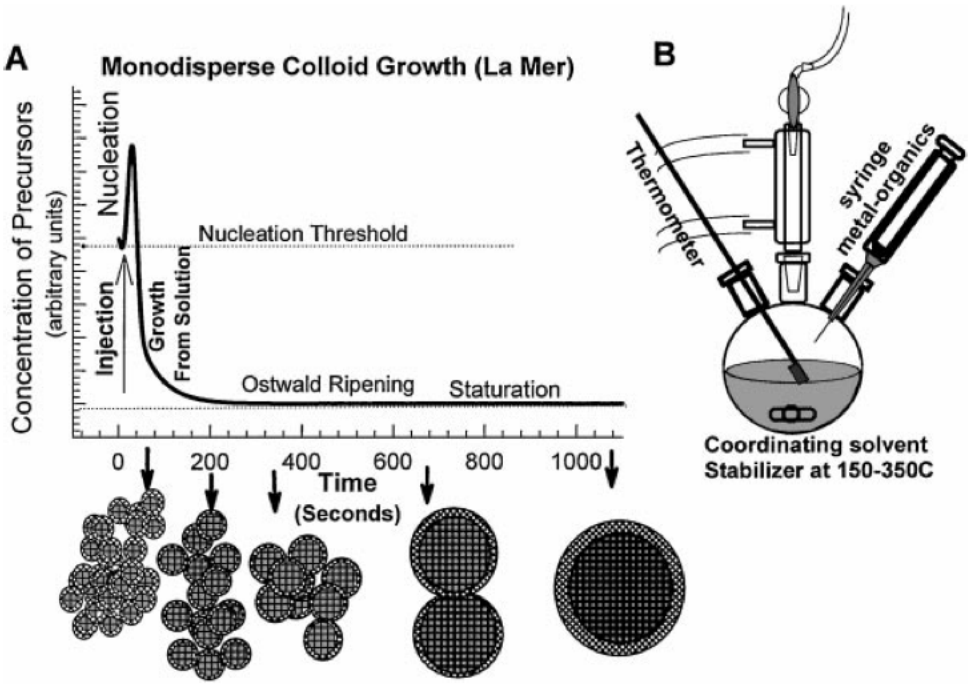

Figure 4. a) Classical LaMer theory of colloidal growth. b) Standard reaction apparatus for hot-injection nanoparticle synthesis. Reprinted with permission from [29]

times, decreasing monodispersity. Coordinating ligand concentrations and coordinating affinity also dramatically affect the kinetics of the nucleation. Once below the nucleation threshold concentration, growth from monomers in solution occurs, growing particles until all monomer molecules are depleted. At this point, depending on the material system, growth of the nanoparticles can differ. Many systems enter what is termed Ostwald Ripening stage, where smaller particles with higher surface energy slowly dissociate. Their monomers add onto the larger particles, increasing the overall final size. Other systems, such as pure metal particles are not observed to enter the Ostwald Ripening stage due to flocculation and halting growth. However, Ostwald Ripening is not an exclusive growth mechanism. Recently, a unique growth mechanism has been discovered called Orientated Attachment where high energy surfaces of the starting seeds

combine to reduce overall energy of the particles.[30-33] This growth mechanism will be discussed later. As mentioned above, the coordinating ligands used dramatically effect both the nucleation and growth of final particles. These coordinating ligands are mostly long chained organic surfactant molecules with differing functional head groups. Examples are molecules like oleic acid, trioctylphosphine, trioctylphosphine oxide, dodecanethiol, and oleylamine. These basic principles have guided many different variations of nanoparticle synthesis, each with different methods, coordinating ligands and solvents, but all must start with a nucleation to create initial seeds.

1.4 Synthesis of Semiconductor and Metal Nanoparticles

1.4.1 Synthesis of Semiconductor Nanoparticles and Quantum Dots

Synthesis of quantum dots (semi-conductor nanoparticles within quantum confined region in size) demand attention, as they were the starting point for many different semiconductor nanoparticle syntheses. One of the first reports of monodisperse semiconductor "Quantum Dots" (QD) was by Bawendi et al.[34] Here, the authors were the first to utilize the hot-injection method above to create monodisperse CdS, CdSe, and CdTe by decomposition of dimethylcadmium (Me_2Cd) with an appropriate chalcogenide precursor and trioctylphosphine and trioctylphosphine oxide. It was observed that reaction mixture's absorbance peaks red shifted as CdSe QD's grew to larger size through Ostwald Ripening, shown in Figure 5. This red shift is related to quantum confinement of the electrons in the nanocrystal. The trapping of the electron gives rise to discrete electron hole states. The energy between these discrete states can be tuned by size of the QD.[10] Many different absorption spectra could be achievable by the QDs with this simple size tuning. Since this original report many vast improvements on this

synthesis, such as Peng and Peng's switch to CdO as cadmium precursor (as Me_2Cd is highly toxic and flammable) have been published.[35-37] These initial reports started a revolution in the nanoparticle field, triggering an explosion of synthetic methods to create many different semiconducting systems such as PdS, PbSe, ZnS, ZnTe, ZnSe, InP, and FeS_2. Many excellent reviews of these syntheses and their practical uses can be found in the literature.[11, 29, 38] Many of these techniques developed by these first reports are still used today, and have even motivated many novel syntheses of metal and bimetallic nanoparticles.

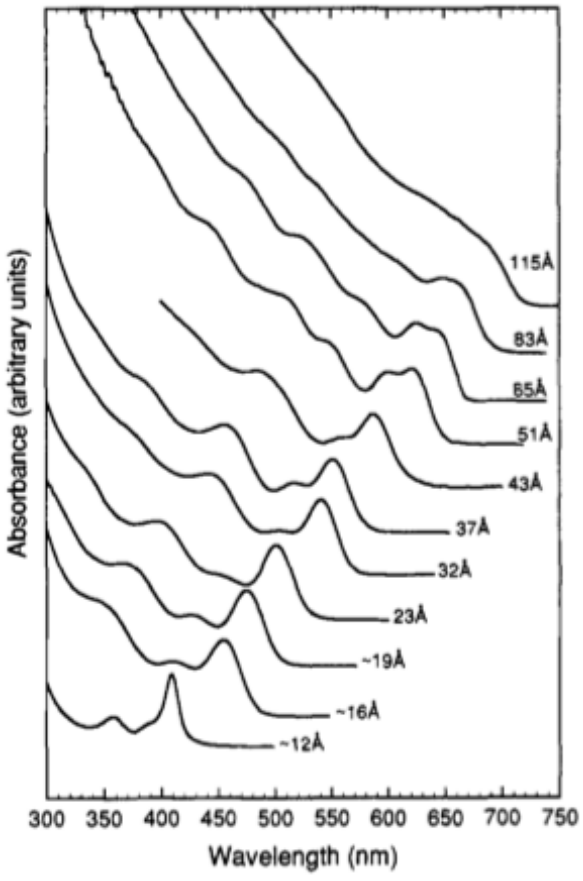

Figure 5. Absorption Spectrum of CdSe QDs dependent on diameter. Reprinted with permission from [34]. Copyright 2015 American Chemical Society.

1.4.2 Metal Nanoparticle Synthesis

Compared to semiconductor nanoparticle synthesis, metal nanoparticle creation requires many of the same components as semiconductor synthesis. This includes coordinating ligands, solvents and the necessity to create a nucleation window. However, a main difference is metal nanoparticle methods have to make use of a reducing agent to provide electrons to convert initial metal salt precursors back to zero-valent metal atoms. Many starting metal nanoparticles syntheses were done within aqueous solutions, due to the ease of dissolving of the metal salts used. For example, Au and Ag nanoparticles are widely explored due to their ease of solvation and reduction with simple citrate anions.[39] These have seen vast uses due to their aqueous setup and their unique plasmonic resonance, which has many promising uses in sensing, imaging, and medical applications.[40-42] For transition metals (Fe, Co, Ni), which are harder to reduce and form at low temperature, high boiling point non-coordinating organic solvent (i.e. diphenyl ether, 1-octadecene, or other long chained organic molecule without coordinating head groups) methods are employed. High temperature is necessary to both completely dissolve the metal salts (metal halides, acetylacetonate (acac), acetates) and the reducing agent used. Many different examples of reducing agents have been utilized over the years, such as sodium borohydride, hydrazine, and sodium naphthalide. The metal salts are dissolved in the high boiling point solvent at varying temperatures (~200-300 °C) in an inert atmosphere along with stabilizing ligands with coordinating head groups, such as long chained phosphides and oleic acid. The reducing agent is then injected to initiate the nucleation event. Once the entirety of the metal reagent is consumed, the reaction is complete, as particles precipitate out of solution halting further growth. However, the size

of metal nanoparticles can be manipulated by amount of coordinating ligands used, providing much needed control.[43] The ability to tune the H_c of magnetic nanoparticles was an interesting phenomenom observed resulting from this size control. Figure 6b diplays the effects on H_c of different size of Co nanoparticles. Figure 6a summarizes that at small sizes, the particles are superparamagnetic. Upon increasing the diameter, the particles enter a single domain phase, where there is H_c increased. Once the particles size large enough, it enters a multi-domian structure, where the Hc quickly decreases to bulk properties. This size dependent H_c is one of the motivations to create nanoscale nanoparticles as it can be utilized to create stronger magnets, as long as the size can be controlled.

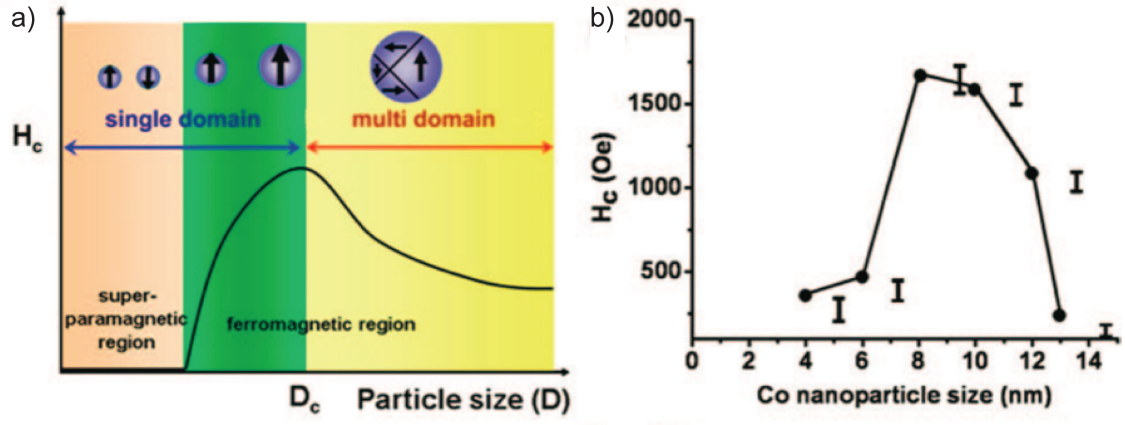

Figure 6. a) Diagram of the effects on Hc dependent on particle size. b) H_c of Co nanoparticles versus size. Reproduced with permission from [25]

Figure 7 displays many different metal nanoparticles examples, including mono and bimetallic systems. It should also be noted that not all metal precursors are required to be metal salts. Many zero-valent metal molecules that can release already reduced metal atoms upon decomposition can be used, removing the need for a reducing agent.

Examples of these are molecules like metal carbonyls ($Fe(CO)_5$, $Co_2(CO)_8$, $Mn_2(CO)_{10}$) and coordinated cyclooctadienes (ex. $Ni(COD)_2$). However, there are only a limited number of these precursors, which do not cover all of the interesting metal systems available. Furthermore, these precursors replace the harsh reducing agents used, but are highly toxic and must be handled carefully.

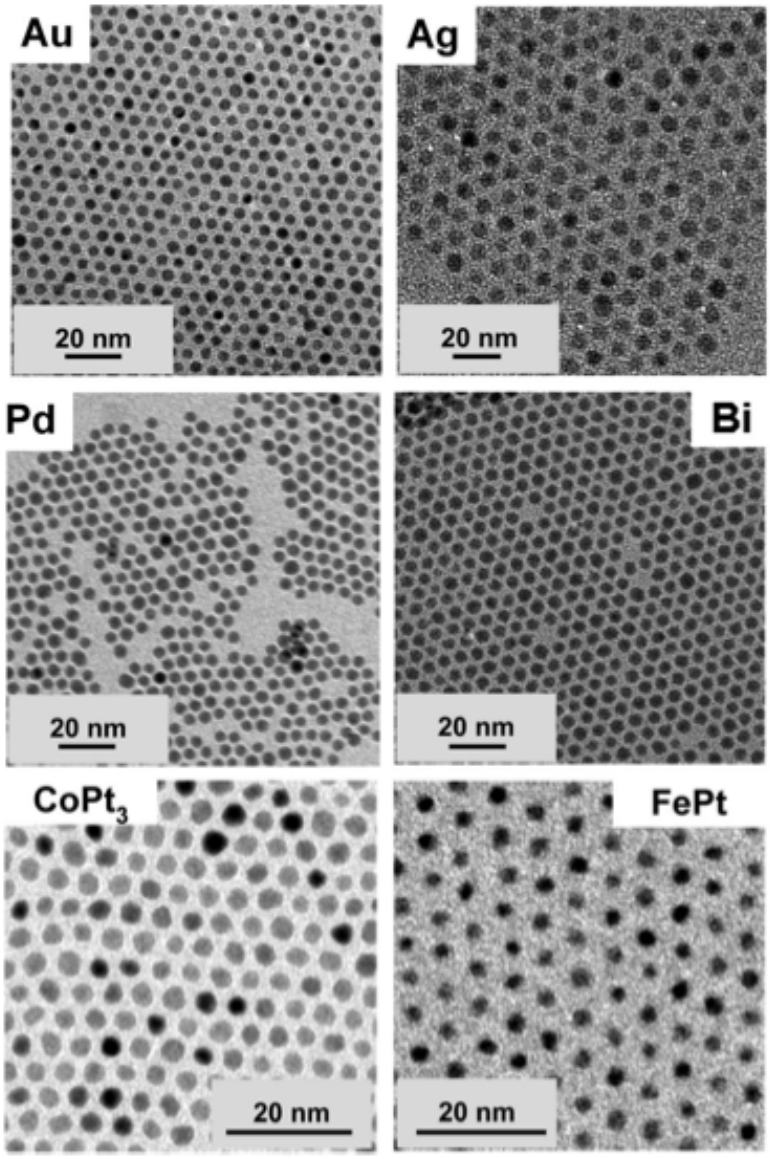

Figure 7. Examples of various types of metal nanoparticles. Used with permission from [11].

With the general methodology of nanoparticle synthesis introduced, next I will discuss basic magnetism to facilitate understanding of following chapters. This includes discussion on the types of magnetism, measurement of basic magnetic properties, and the different types of magnetic materials.

In the following chapters, I attempt to further the knowledge of different iron containing material systems that show promise for green energy applications. In Chapter 2, discussion of the earth-abundant nontoxic semi-conductor Iron Pyrite nanosynthesis is undertaken. Shape control and growth mechanisms of Iron Pyrite nanoparticles are explored and elucidated, providing knowledge for future applications in photocatalysts and optoelectronic devices such as solar cells and photodetectors. In the following chapters, focus is shifted on creating novel $FePd/Fe_2O_3$ core-shell particles, which is shown to be a valid foundation for generation of a magnetic nanocomposite. Finally, in Chapter 3, a new nanosynthetic strategy for creation of magnetic metal alloys is presented, eliminating issues that plague standard nanoparticle synthesis techniques. This novel strategy is shown to be versatile and easily adapted to many different metal alloy systems, and can even find uses in catalytic conversions proving its robustness.

2 Synthesis of Iron Pyrite Nanoparticles

2.1 Introduction

2.1.1 Motivation

Iron pyrite shows immense promise in use as a semi-conductor in many different applications such as photovoltaics, photoelectrochemical cells and photodetectors. Pyrite exhibits a band gap of 0.95 eV and an extraordinarily high absorption coefficient ($>10^5$ cm^{-1}), which is two orders of magnitude greater than silicon, which is the standard semiconductor material.[6, 7] Due to such a high absorption coefficient, substantially less material is necessary to absorb most of the light impinged upon the photodevice. Another benefit of FeS_2 is the cost of the material. Iron is the fourth most abundant element in the earth's crust, trailing silicon, which comes in second.[44] However, the cost of extraction of silicon is ~$1.70/kg, whereas the extraction of iron comes in at $0.03/kg.[4] Thermodynamics dictate this immense difference in cost. The cost of purifying silicon from its material source of silica (SiO_2) costs 24 kWh/kg. Generating iron from hematite (Fe_2O_3) only requires 2 kWh/Kg, making it cheaper to generate raw iron than raw silicon.[45] Figure 8 displays a graph of calculated yearly electricity production from annual and known economic reserves of many different semi-conductor materials. It can be seen that FeS_2 is one of the most promising materials to supplement the necessary power needs of the world. Furthermore, as FeS_2 exhibits such a high absorbance coefficient, it is predicted only 100 nm is needed to absorb 90% of incoming light.[46] Nanotechnology has allowed for the creation particles matching well with this size, with simplicity of handling and deposition.

Finally, current mentality of creating the highest efficiency photovoltaic must be challenged. Having a C-Si solar cell with 20% power conversion efficiency (PCE) will still not satisfy annual energy consumption itself. A pure FeS_2 photovoltaic device with 4% PCE will produce the same amount of output utilizing three times less material and lower cost.[4] Given the gains in cost and material consumption, low efficiency cells should be considered for the market. It follows then that thin film production of pyrite nanoparticles show promise as a viable photovoltaic semiconductor, as well as an active layer in other photodevices. However, the synthesis of the material needs to be controlled.

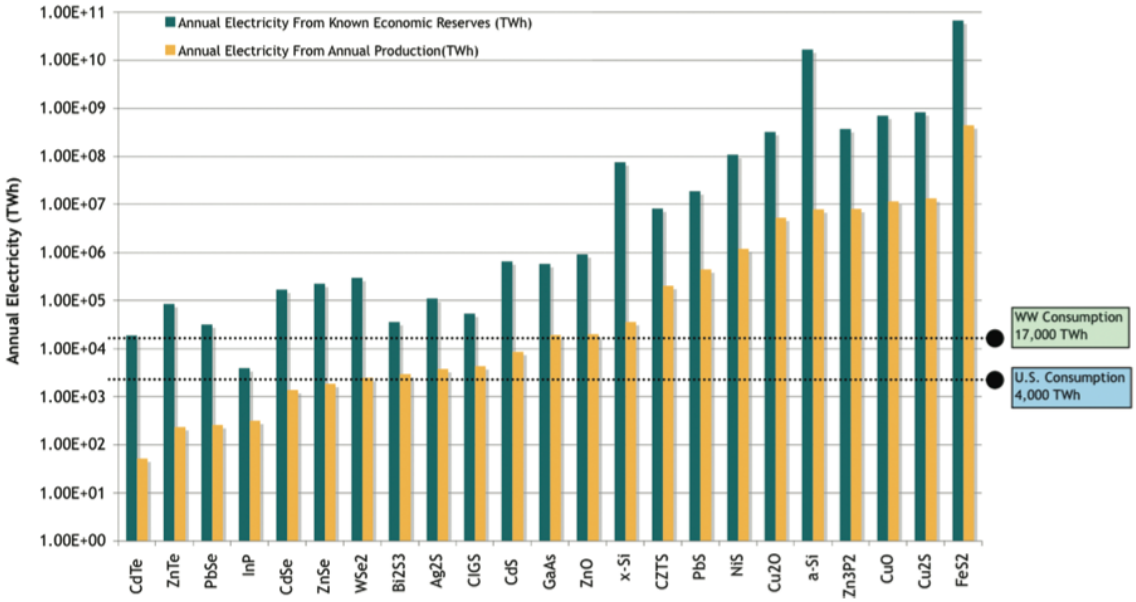

Figure 8. Annual electricity production of different types of photovoltaic materials from yearly generation and known reserves. Worldwide and United States energy consumption marked with dotted lines. Reprinted with permission from [4]. Copyright 2015 American Chemical Society.

2.1.2 Iron Pyrite Structure and Properties

Pyrite possesses a very basic cubic AB_2 structure. In fact, it was one of the first structures defined by x-ray diffraction studies when the technique was being developed. The structure is shared with an entire family of other important minerals including ones with pnictides (P, As, Sb) and chalcogenides (S, Se, Te). This group of minerals is named the pyrite family, as FeS_2 is the most famous mineral. Its structure can be thought of as NaCl with the irons replacing the sodium atom and the chloride atoms are replaced by a dumbbell S_2 dimer. This structures places iron in an octahedral site surrounded by six sulfurs. The sulfurs sit in a distorted tetrahedral site with one iron and three other sulfurs bonded. Since the dumbbell S_2 distorts the tetrahedral sites, the simple NaCl cubic structure is modified, putting iron pyrite in the Pa3 point group. The lattice constant of FeS_2 is 5.418 Å with a distance of 2.26 Å for the Fe-S bond and the S-S bond distance of 2.14 Å.[47] The pyrite structure for FeS_2 is not the only polymorph it can take. Marcasite also possesses the FeS_2 stoichiometry, but exhibits an orthorhombic structure instead of basic cubic. This change in the structure changes the properties of this crystal phase. It has been suggested that complete removal of marcasite from pyrite is necessary, as it will create gap states in the band gap. However, this is still under debate in the literature, with recent theory challenging this mentality.[48]

Crystal field theory predicts that a transition metal's d orbitals are non-degenerate in an octahedral environment. As iron is in the octahedral spot within the crystal structure, this splits the d orbitals into t_{2g} set made up with d_{xy}, d_{yz}, d_{xz} orbitals and an e_g set with the remaining d_z^2-$_y^2$ and d_z^2 orbitals. Iron is in the oxidation state of +2 in FeS_2, leaving six electrons to completely fill up the t_{2g} orbital set under the low-spin approach. As such,

iron pyrite is a diamagnetic low-spin semi-conducting material with a band gap found to be 0.95 eV between the two orbital sets. While this band gap is generally accepted in literature, all solar cells generated with pyrite have experienced very low open circuit voltage. Many different reasons have been proposed for this low voltage; however, sulfur vacancies within the crystal structure are the most cited for the cause of the low performance. Many different theoretical studies have been conducted recently to determine if FeS_2 is thermodynamically driven to be a pure compound, but the solution to iron pyrite's low open circuit voltage is ambiguous.[48-51]

The crystal faces of iron pyrite are important to discuss, especially when in the nanosized regime and dealing with charge transfer within devices. Initial studies show that nanosized crystals will exhibit either the {100} or {111} crystal surfaces, however other faces can be achieved with careful synthetic control, shown later in this work.[49, 53-54] It is important to note that iron pyrite's {100} surface has lower surface energy than its {111} making it contrast many other crystals with similar structure, which can help explain why both nano and macro-sized crystals of pyrite usually desire to form cubic structures.[52] Figure 9 displays models of the different {100} and {111} surfaces. The {111} (Figure 9c) surface is completely terminated by sulfur and is non-polar. However, the {100} surface can be terminated in variable different ways. These possibilities are [S-Fe-S], [Fe-S-S] and [S-S-Fe]. It can be seen that the latter two of these terminations are polar and can lead to the possibility of iron-terminated surfaces. Having these iron-terminated faces leads to a change in the crystal field splitting of the iron from an octahedral to a trigonal bipyramidal structure (shown in the {100} close-up in Figure 9a). It was first thought that this splitting change could lead to trap states within the band gap

of pure pyrite, which could explain the lower open circuit voltage. However calculations show that this change does not place the states within the band gap.[48] It has also been theorized that changing sulfur concentrations during growth could affect the termination of the surfaces, which could lead to better performance from the material.[53] In any case, the two main surfaces of pyrite are different from one another leading to different chemistry and properties of the surfaces.[53, 57-58]

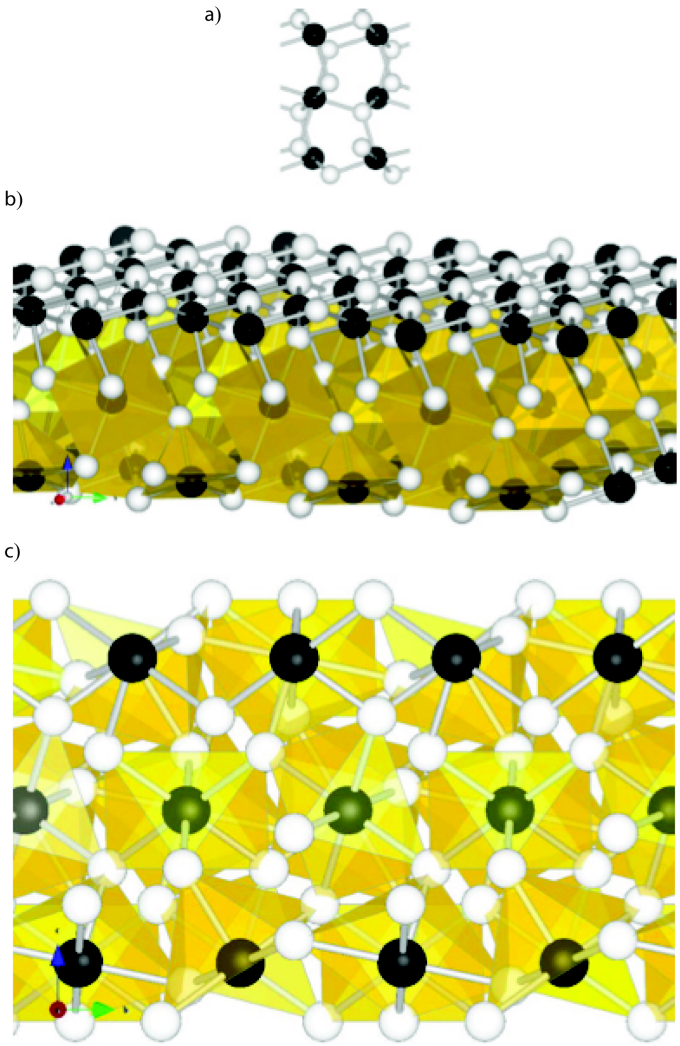

Figure 9. a,b) Model of the {100} surface of iron pyrite with a close-up shown in (a). c) Model of the completely sulfur terminated {111} surface of iron pyrite. Used with permission from [48]

2.2 Synthesis of Iron Pyrite Nanomaterial

There have been many different methodologies to grow pyrite material. Seminal bulk studies by Tributsch and his group used chemical vapor deposition (CVD) and metal organic chemical vapor deposition (MOCVD), which is often cited as the starting point of

interest in iron pyrite as a photovoltaic semi-conductor.[54-57] Following these studies, more focus on nanoparticle generation occurred starting first with hydrothermal methodologies, followed by standard high temperature organic solvent methods.[58-60] Of the latter, both one-pot precipitation and two-pot hot-injection methods were developed.[61-63] In this section, our two-pot hot-injection method will be the focus, which allows control of the iron pyrite particles and their properties.

2.2.1 Thermodynamic and Precursor control of Iron Pyrite Nanoparticles

Motivation for the first synthesis of iron pyrite nanoparticles in our group started with the Law et al. report on generation of spherical FeS_2 particles.[64] Using this standard synthesis, I set out to systematically control shape, size, and properties of pyrite nanoparticles to help lay the foundation for iron pyrite nanoparticle synthesis. An iron precursor and octadecylamine (ODA), which was used for both ligand and high boiling point solvent were loaded into a flask and heated to 120 °C. In another flask, diphenyl ether and colloidal sulfur powder were heated to 70 °C. The sulfur solution was then injected into the iron flask at varying temperatures to initiate the reaction. The solution was then brought to a final temperature of 220 °C for 90 min. Full materials and methods can be found at the end of this chapter. It was found that varying both injection temperatures and iron precursors had a pronounced effect on the final particles shape. In the case of using $FeCl_2$ as the iron precursor, changing the injection temperature radically change the shape from ~80 nm cubic structures (120 °C injection temperature) to smaller, ~30 nm diameter spherical like structures (220 °C) as seen in the transmission electron microscope (TEM) images in Figure 10a-c. At an intermediate injection temperature of 170 °C large “popcorn-like” structures that are around ~220 nm in size are produced.

When changing the precursors to $Fe(acac)_2$ and $Fe(CO)_5$, thin sheets (Figure 10d) and thick sheets with defined edges (Figure 10e) were produced respectively at an injection temperature of 220 °C.

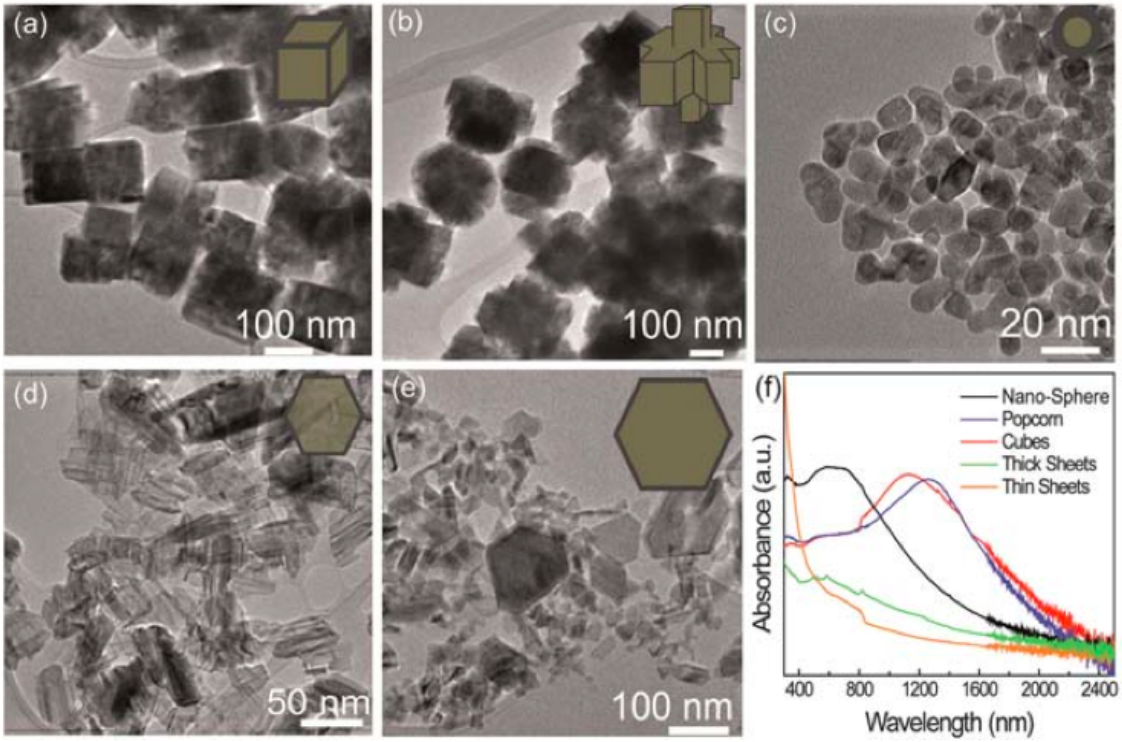

Figure 10. Iron Pyrite nanoparticle shape dependence on injection temperatures and Iron precursor. a-c) Nanoparticles produced using $FeCl_2$ and an injection temperature of a) 120 °C, b) 170 °C, c) 220 °C. d,e) Iron pyrite nanoparticles produced using 220 °C injection temperature with d) $Fe(acac)_2$ and e) $Fe(CO)_5$. f) Uv-Vis absorption spectra of the different particles produced. [65] – Reproduced by permission of The Royal Society of Chemistry.

Uv-Vis absorption spectra of each structure are also shown to be vastly different. Figure 10f displays the different spectra depending on size and shape. Absorbance spectrum of the nanospheres matches well with other reports with the maximum peak

seen around 600 nm.[64] When the structures are cubic, the absorbance peak shifts into the near infrared region (NIR) of the spectrum with a peak centered around 1100 nm. Other cubic iron pyrite nanomaterial also show this characteristic NIR absorption peak.[59] The popcorn particles show a more intense shift into the NIR with a peak centered at 1300 nm, most likely caused by the aggregation effect of the cubic structures coming together to form the final popcorn shape. Both sheet structures showed mostly broadband absorption with very little definitive peaks between them. The spherical FeS_2 particles show promise for use in photovoltaic devices due to its absorbance matching the solar spectrum. However, the cubic FeS_2 particles exhibit unique NIR absorbance, which can find better use in NIR photodetectors.

Characterization of these particles is needed to determine phase purity of FeS_2 that was generated. Figure 11a display XRD patterns for each of the different FeS_2 particles formed. From these patterns, it is observed that all of the particles created with the $FeCl_2$ and $Fe(CO)_5$ precursors generate pure phase iron pyrite diffraction with no other common contaminates (i.e. marcasite or greigite). When $Fe(acac)_2$ is used as an iron source, pyrite diffraction is seen, but a large amount of greigite contamination is observed. When others have utilized $Fe(acac)_2$ as a source, they found that only greigite material was formed, indicating a difference in formation when using this precursor.[66] A reason for this different phase formation with different precursors will be discussed later. Figure 11b-c displays High Resolution TEM (HRTEM) images of spheres, cubes and thick sheets. All of the samples show high crystallinity throughout the particle, indicated by the lattice structure observed. In the nanosphere sample, the lattice shows a {111} growth direction that is confirmed by the fast Fourier transform (FFT) of the lattice, which

produces a hexagonal pattern in the inset of Figure 11b. When examining the FFT of the cube sample, a square pattern is shown, indicating a {100} lattice. The same FFT patterns are seen for the thick sheet sample, although there are some smaller satellite spots, indicating a possibility of other domains present within them.

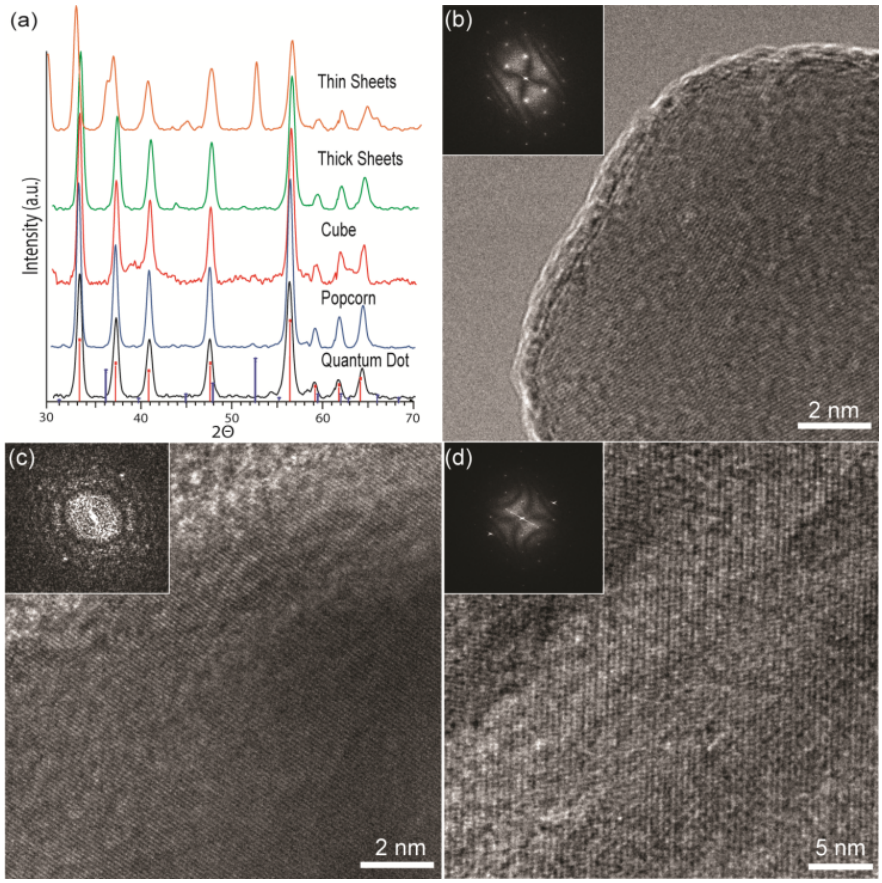

Figure 11. a) X-Ray Diffraction Patterns of the different iron pyrite nanoparticles. Red line represents iron pyrite (JCPDS 1-079-0617) and blue represents greigite (Fe_3S_4, JCPDS 1-089-1999) diffraction. b-d) HRTEM images of b) nanospheres, c) cubes, d) thick sheets. Insets are fast Fourier transforms of images. [65] – Reproduced by permission of The Royal Society of Chemistry.

To better understand the shape control produced by the different injection temperatures of the $FeCl_2$ precursor sample, a simple thermodynamic model is proposed

in Figure 8. After creating monomers of the precursors by decomposition, the shape of the particles can be controlled by Gibbs free energy (G = H- TS). Knowing that the enthalpy (H) will stay the same (same amount and type of starting material), only the temperature (T) and entropy (S) can play a role in controlling final shape. Temperature is easily controllable in the synthesis. Entropy must also be considered due to having a higher amount of available decomposed monomers at higher temperatures. If injection occurs at a higher temperature (T), more monomer (higher S) both contribute energy to allow for higher energy {111} growth to be possible, shown by the left path in Figure 12. At lower temperatures, not enough energy is available from both temperature and entropic contributions, so the {100} growth direction is preferred, producing final cubic structures (right path, Figure 12). With an intermediate temperature of 170 °C, both growth directions are likely seen, but upon aging the higher energy {111} surface merge with other {111} faces, leaving only the more energetically favorable {100} surface exposed.

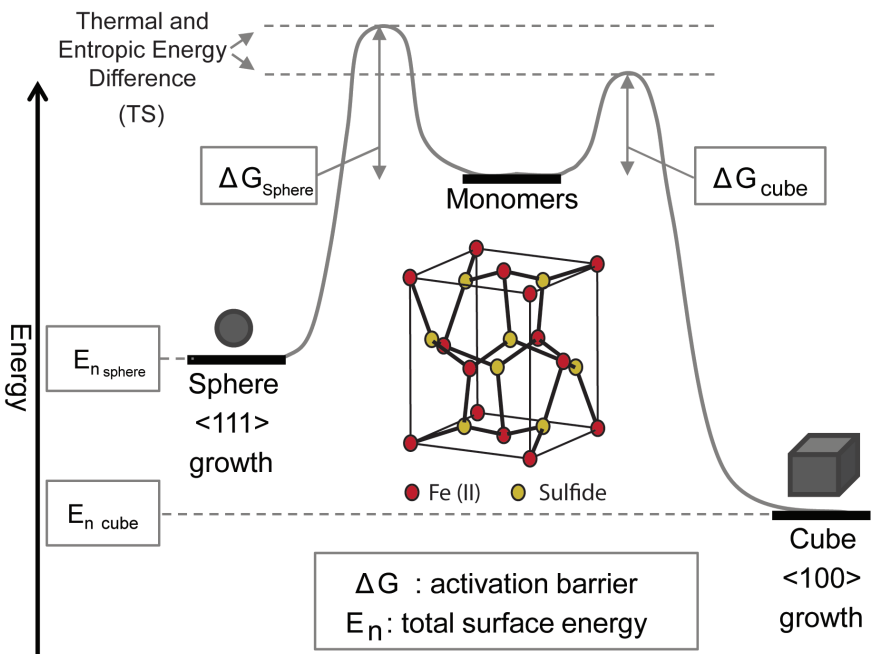

Figure 12. Proposed energy diagram for the formation of different shape iron pyrite nanoparticles from the $FeCl_2$ precursor. [65] – Reproduced by permission of The Royal Society of Chemistry.

While this simple model works for the iron pyrite nanoparticles produced when utilizing $FeCl_2$ as a precursor, explanation for the shape changes observed when utilizing both $Fe(CO)_5$ and $Fe(acac)_2$ is still required. Since the temperature of injection is the same, only the rate at which the monomers are created by decomposition of the precursor will change. For this, we can use simple hard/soft acid-base (HSAB) concepts, which states that like components bind stronger and unlike have weaker binding. Weaker binding precursors should release iron quicker than more strongly bound precursors, allowing for different growth mechanisms. Looking at $Fe(acac)_2$, the acac ligand is a very hard base and the Fe^{2+} ion is an average acid.[67] Direct comparison to $FeCl_2$ can be made, where Cl^- is also a hard base, but not at the same magnitude as the acac ligand, indicating

that $Fe(acac)_2$ should have weaker binding. When considering $Fe(CO)_5$, it is known that Fe^0 is a soft acid and the CO ligand is a soft base, meaning these should bond somewhat stronger to each of the other precursors. Knowing the rough binding tendencies using the HSAB, trends can be related back to shape of particles of the iron pyrite produced. First, $Fe(acac)_2$ decomposes the quickest, releasing very high amounts of iron monomer which corresponds to the iron rich greigite (Fe_3S_4) phase that appears in the XRD spectra above. According to HSAB, when using the slightly more stable $FeCl_2$ as a precursor, smaller nanospheres of pure pyrite are achieved indicating an optimal release rate of iron monomers. Finally, $Fe(CO)_5$ releases iron monomers the slowest, and on top of that, a oxidation of the Fe^0 to Fe^{2+} must occur, meaning smaller amount of seeds will form. More monomer will then add onto the initial plates formed, growing them larger and thicker. Utilizing both the temperature model and HSAB concepts, different iron precursor effects on particle shape and purity can be explained.

2.2.2 Growth of Iron Pyrite Plates

As seen in Figure 10e, iron pyrite plates were grown utilizing $Fe(CO)_5$ as the iron precursor and ODA as the coordinating ligand. Formation of these plates was interesting to us, as they did not take the shape of cubes or spheres, which are the preferred growth directions. Furthermore, 2D nanomaterials exhibit horizontal confinement of electrons and high surface area, which could lead to improvements in photocatalysts and photovoltaic or photodetector devices. Due to this, more extensive studies of the FeS_2 plates were conducted.

Temperature dependent growth was first studied to examine the effects on the pyrite plates produced. With a lower injection/reaction temperature of 120 °C only an

amorphous precursor state was formed as seen in the scanning electron microscope (SEM) and TEM images in Figure 13a,d respectively. The lower temperature of this reaction did not provide enough thermal energy to completely decompose the starting precursor, which in turn did not allow for crystallization of the particles within the 180 minutes of reaction time. Upon increasing the reaction temperature to 180 °C, smaller plates with define edges are observed, with a diameter of ~150 nm in size (Figure 13b,e). Finally, when reaction temperature is raised to a temperature 240 °C, the thick hexagonal plates are observed, shown in Figure 13c,f. It is apparent that the lower temperatures produce thinner plates from $Fe(CO)_5$ and that temperature plays and important role in the formation of the 2D iron pyrite plates.

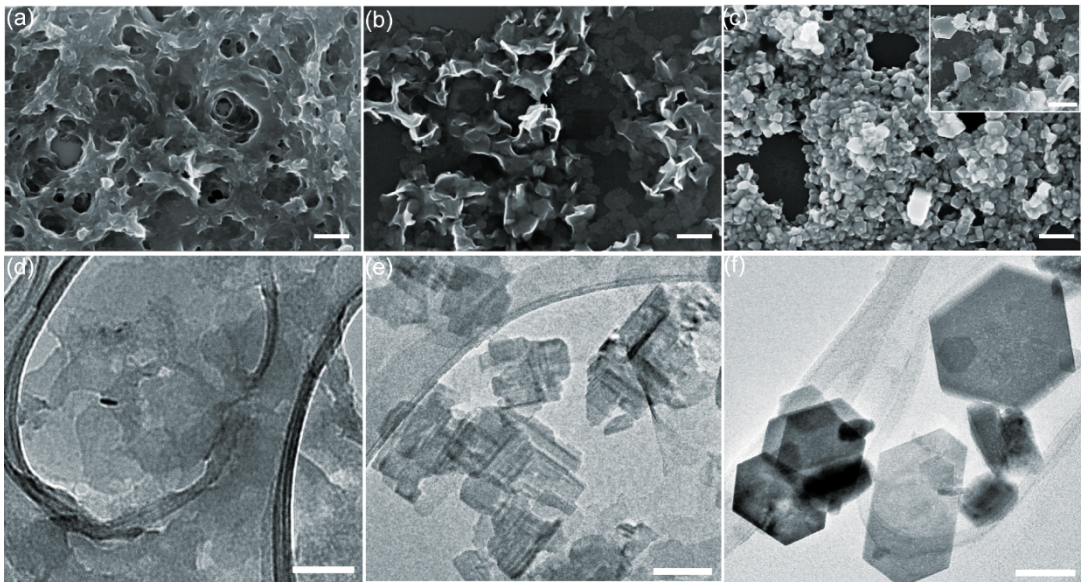

Figure 13. SEM and TEM images of iron pyrite nanoparticles with a reaction temperature of (a,d) 120 °C, (b,e) 180 °C, and (c,f) 240 °C. Scale bars are 200 nm. Reprinted with permission from [68]. Copyright 2015 American Chemical Society.

Investigation into how these plates are formed is important as it could provide clues to control shape of other FeS_2 nanoparticles. To achieve this, aliquots were taken at 3 min, 180 min, and 540 min during the 180 °C reaction. TEM images of the nanoparticles at each of these growth times are displayed in Figure 14. At 3 min into the reaction small plates are starting to form. Aging longer (180 min, Figure 14b) plates have grown to a larger size, and start layering on top of one another. Finally, at 540 min, much larger and thicker plates are generated shown in Figure 14d. Lattice are observed in the HRTEM image in Figure 14d, confirming these are indeed crystalline and not amorphous particles. These final plates exhibit a hexagonal shape, much like the plates generated at 240 °C, but on the micron scale. It is highly doubtful that Ostwald ripening is the cause of such large plates, suggesting that another growth mechanism is occurring. Stacking of the smaller plates onto one larger plate likely causes this. In any case, simply changing temperature and reaction time can generate vastly different 2D nanoplate structures of FeS_2.

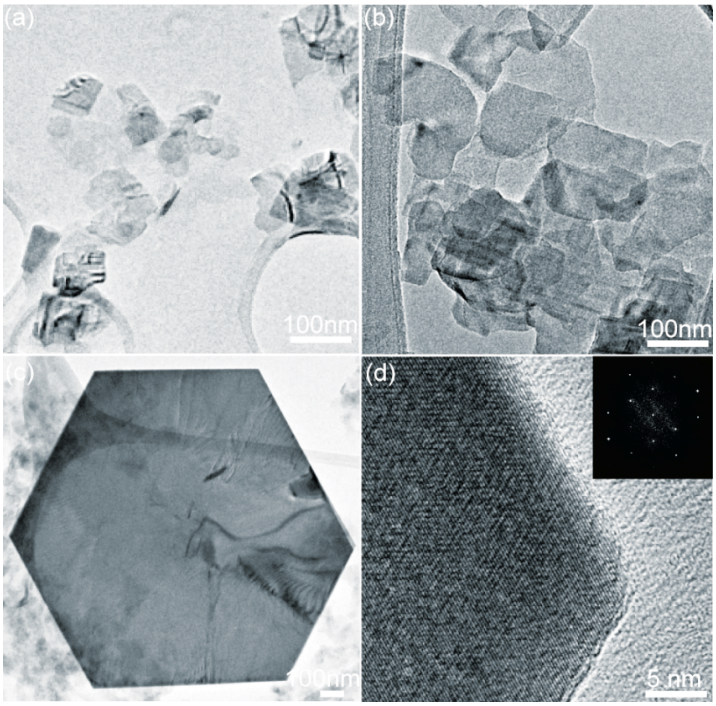

Figure 14. TEM images of iron pyrite nanoparticles at 180 °C reaction temperature at a) 3min, b) 180 min, and c) 540 min. d) HRTEM image of plate edge shown in (c). Inset is FFT of lattice. Reprinted with permission from [68]. Copyright 2015 American Chemical Society.

2.2.3 Surface Face Dependent Photocatalytic Activity and Stability.

The possibility of controlling the exposed surface faces of the pyrite nanoparticles provides the opportunity to study the differences of photocatalytic performance and stability between them. To achieve this, a standard photodegradation of methyl orange in water was utilized to examine the photocatalytic activity and degradation of the different shaped particles. Comparison of the different FeS_2 nanoparticles generated from the $FeCl_2$ precursors will be examined first.

Figure 15a-c displays the UV-Vis spectra series for the three different shapes of nanocubes (Figure 10a), popcorn (Figure 10b) and nanospheres (Figure 10c). The

nanocube structure has modest degradation of the methyl orange absorbance peak at 450 nm after 80 min of reaction time. Popcorn has even less activity than the nanocubes with minimal loss methyl orange absorption. Finally, the nanospheres show the least amount of dye degradation of the three shapes. The activity of the photodegradation can be related back to the different exposed surfaces of the particles. The nanocube FeS_2 particles surface is dominated by the {100} surface, which shows the highest activity. The nanosphere particles with mostly {111} surface show the least activity while the popcorn show moderate degradation most likely due to a less surface area due to their larger size. As mentioned above, the {100} surface is iron terminated while the {111} face is completely sulfur terminated. This could indicate the photodegradation could be dependent on having iron sites on the surface

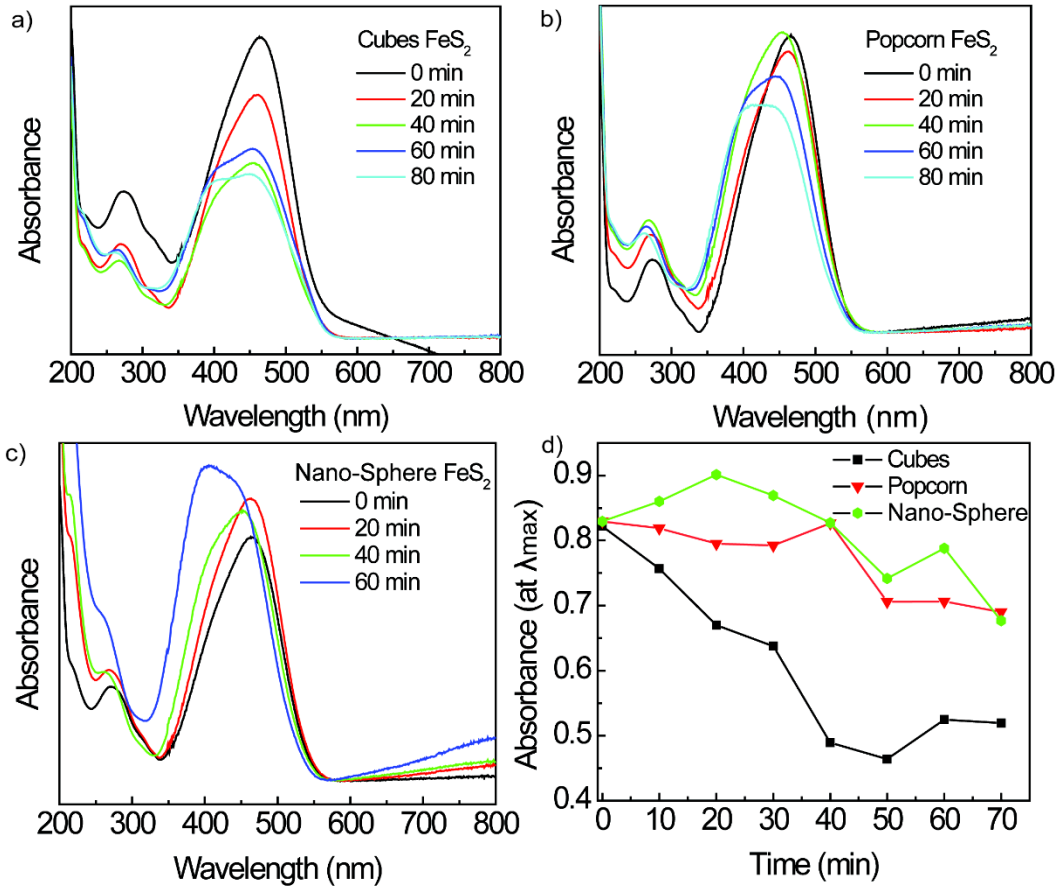

Figure 15. Uv-Vis spectra of photodegradation of methyl orange by a) Cubic FeS_2, b) Popcorn FeS_2 and c) Nanosphere FeS_2. d) Summary of absorbance at λ_{max} versus time of the different shaped FeS_2 nanoparticles. [65] – Reproduced by permission of The Royal Society of Chemistry.

From spectra presented in Figure 15, another peak can be seen to be growing in around 400 nm. This other peak indicates another species within the solution that is forming during the photodegradation experiment. Upon further investigation, it was found that pyrite degrades and then oxidizes in aqueous solutions, which in fact is the main cause of acid mine drainage. Acid mine drainage is when bodies of water around

mines become acidified by the breakdown of iron pyrite in water to produce sulfuric acid. It follows the following reactions:[69]

$FeS_2(s) + 3.5O_2(g) + H_20(l) \rightarrow Fe^{2+}(aq) + 2SO_4^{2-}(aq)\ 2H^+(aq)$ (Eq. 1)

From here, it can be seen that sulfuric acid is produced upon the degradation of pyrite. Upon measuring the pH of the solution after the reaction is complete and comparing it to before a drop to 2.9 from 4.2 is observed indicating acidification during the reaction, consistent with the above equation. The Fe^{2+} ion can then be oxidized to Fe^{3+} by the following equation:[69]

$4Fe^{2+}(aq) + O_2(g) + 4H^+ \rightarrow 4Fe^{3+}(aq) + 2H_2O(l)$ (Eq. 2)

This oxidation can be confirmed with addition of NaOH to the solution, where an insoluble brown $Fe(OH)_3$ forms. Moreover, the new peak within the absorption spectra can be attributed to this Fe^{3+} ion in solution by matching $FeCl_3$ absorbance spectra, which has a main absorbance peak at 400 nm. Also, the nanospheres after the photocatalytic reaction are degraded as shown in the TEM image in Figure 16. This confirms that these particles are not completely stable in an aqueous solution.

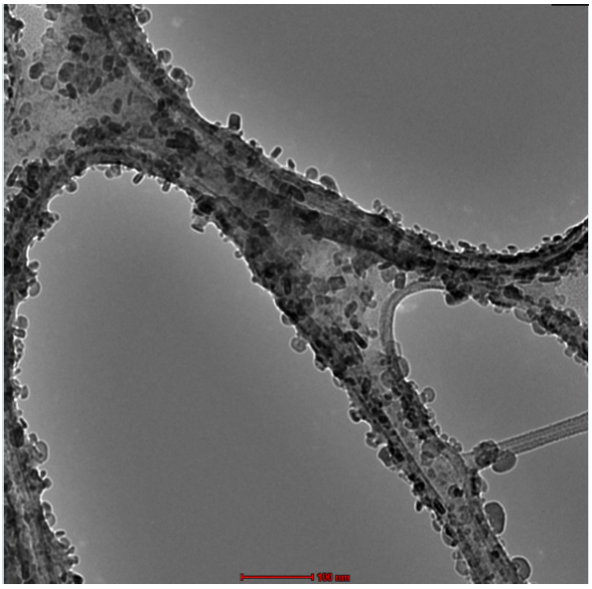

Figure 16. FeS_2 nanosphere sample after methyl orange photodegradation experiment. [65] – Reproduced by permission of The Royal Society of Chemistry.

As noted above, the appearance of the new peak at 400 nm within the spectra can be attributed to the degradation of the FeS_2 nanoparticles. This gives the opportunity to discuss the photostability of different surface faces of iron pyrite in water. From the spectra in Figure 15, it is observed the nanosphere sample experiences the most extreme degradation, with the absorption peak shifting to 400 nm within 60 min. Cubic pyrite nanoparticles also experience degradation, but not to the same magnitude as the nanospheres. The popcorn particles' (Figure 10b) degradation intensity falls in between the two other samples. Previously it has been found that H_2O absorbs onto sulfur defect sites, where it can then undergo the above mentioned chemistry.[70] As the {111} surface is sulfur terminated, it will possess the most sulfur defects, degrading quicker than the other {100} faces. These experimental results indicate that the {111} surface is less stable than the {100} surface to photooxidation in water.

Photocatalytic activity and stability of the iron pyrite particles produced by different iron precursors, such as the thin and thick plates, can also be examined using this simple method. Figure 17a-c display the Uv-Vis spectra of photodegradation of methyl orange using the thin plates (Figure 10d), thick plates (Figure 10e), and nanospheres (Figure 10c), respectively. Very different activity is observed for the plates when compared to the other structures. Both the thin plates and thick plates rapidly degrade the methyl orange, as indicated by the decrease in absorbance at 450 nm thereby further confirming that the {100} face is more photoactive towards methyl orange. Furthermore, there is no secondary peak that is seen to grow in, indicating that the plates are more stable to oxidation than the other structures. This could be attributed to both the high amount of stable {100} surfaces and high crystallinity. Due to this stability and activity, FeS_2 plate structures show promise as photocatalyst due to their high surface area and stability in water.

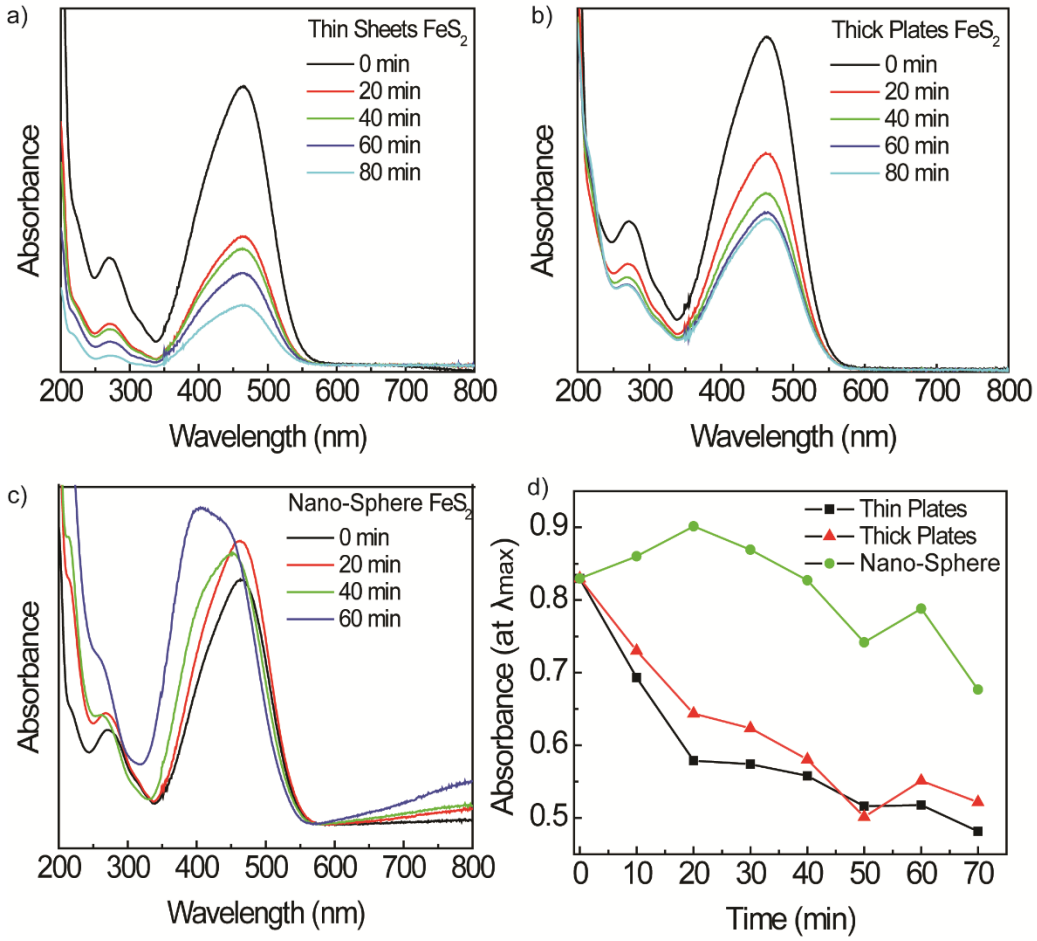

Figure 17. Uv-Vis spectra of the photodegradation of methyl orange with a) thin plates ($Fe(acac)_2$), b) thick plates ($Fe(CO)_5$), c) nanospheres. d) Summary of absorbance at λ_{max} versus time of the FeS_2 nanoparticles produced from different precursors. [65] – Reproduced by permission of The Royal Society of Chemistry.

2.3 An Improved Growth Mechanism - Oriented Attachment

2.3.1 Oriented Attachment Growth

In 1998, Penn and Banfield published work that shook up the standard idea of nanosynthesis growth mechanisms.[30] They suggested that instead of Ostwald Ripening

that controlled final size of nanoparticles, a completely different pathway could be responsible. They deemed this mechanism Oriented Attachment (OA), and used TiO_2 nanocrystals to support their mechanism. The mechanism stated that instead of the dissolution the higher-energy surfaces on small particles as suggested by Ostwald Ripening, the high-energy surfaces could merge together, reducing the overall surface energy. Merging of particles is then the how the particles grow, instead of the classical monomer additions. Figure 18 displays a cartoon depiction of the differences between the classical Ostwald Ripening mechanism and the OA mechanism. The basics of OA growth follow these steps: 1) seed particles start to aggregate with each other followed by 2) rotation of the seed particles to achieve matching of the higher surface area then 3) removal of any absorbents, such as ligands, and finally 4) coherence between the two faces to eliminate the high energy surfaces. Since the proposal of this mechanism, many systems including oxides (i.e. CeO_2, Fe_2O_3, ZnO), sulfides and other chalcogenides

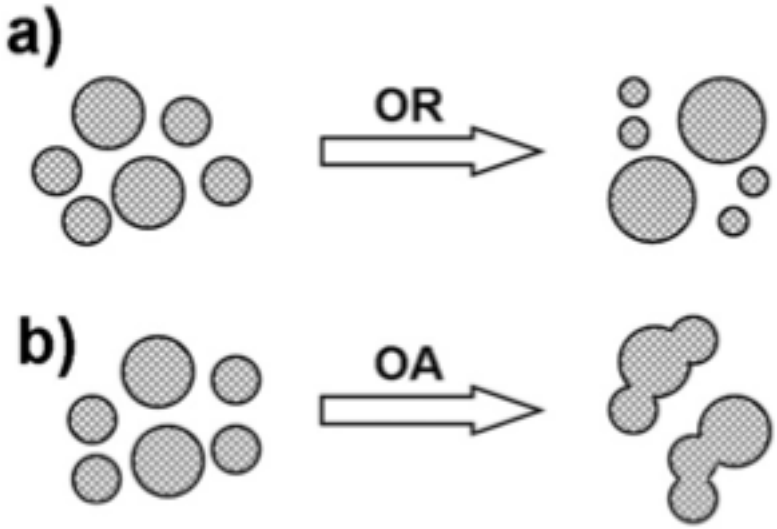

Figure 18. Comparison between Ostwald Ripening and Oriented Attachment (OA). [71] – Reproduced by permission of The Royal Society of Chemistry.

(i.e. ZnS, CdS, PbSe, CdSe) and even pure metals (i.e. Ag, Au).[72-78] This oriented attachment growth mechanism and how it relates to the FeS_2 system will be discussed in the following section.

2.3.2 Oriented Attachment Growth of Pyrite Nanoparticles

Upon seeing that large (~ 1 μm) FeS_2 hexagonal plates form in Figure 14 after long reaction times, we were not convinced that Ostwald ripening was the main factor behind such extreme growth. This spurred us to examine the growth processes for the FeS_2 structures obtained by taking aliquots throughout the reactions. Upon initial hot-injection it was found that FeS_2 quantum dot seeds were created through standard LaMer theory. TEM images and the absorption spectrum of these particles are presented in Figure 19. It can be seen that this particles have a tight distribution around 2 nm and show excitonic peaks matching those that have been reported previously.[79]

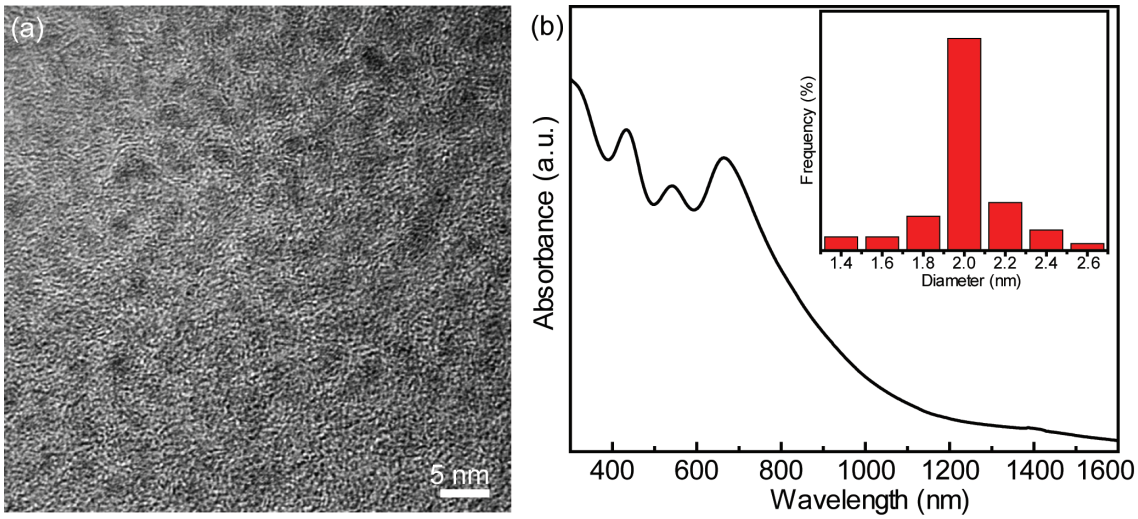

Figure 19. a) TEM image of the FeS_2 seeds. b) Absorption spectrum of the FeS_2 seeds. Reproduced with permissions from [80].

At different injection temperatures, different size seeds were generated that could undergo multiple paths of OA (Figure 20a,e). From here, these seeds enter the OA growth process generating the final structures. Figure 20 displays the full OA process for both cubic FeS_2 (top) and FeS_2 nanosheets (bottom). Starting with the cubic structure, Figure 20a shows larger seeds that were created at lower injection temperatures of

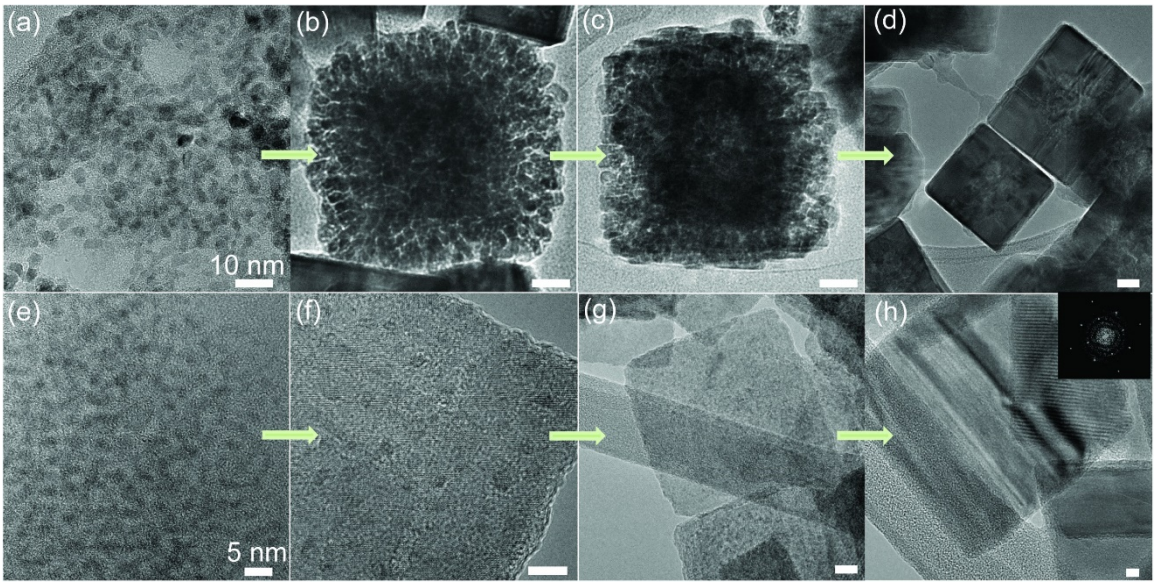

Figure 20. TEM images of OA process for formation of (a-d) Cubic FeS_2 (scale bars 10 nm) and (e-h) Cubic FeS_2 nanosheets (scale bars 5 nm). Reproduced with permissions from [80].

120 °C. These seeds then enter the collision phase, where they start to merge together (Figure 20b). Even at this state the final cubic structure outline is observed To confirm the OA process, HRTEM images were taken during the collision and coalescence of the FeS_2 nanocubes. Figure 17a shows a typical image of the collision stage in FeS_2 cube formation. Upon further magnification, collision points can be seen in Figure 21b,c, where defects within the crystal lattice are observed indicative of the OA growth

mechanism to start forming. The seeds then start to coalesce (Figure 20c), merging high-energy surfaces (i.e. the {111} surfaces) leaving only the low energy {100} surface

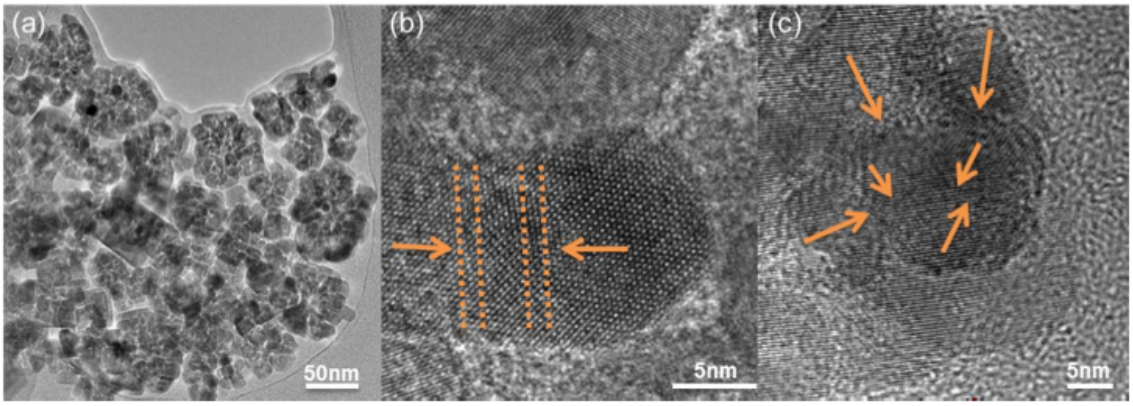

Figure 21. TEM and HRTEM of the (a) collision and (b,c) coalescence of FeS_2 seeds. Orange arrows indicate defects within the lattice, a sign of the OA process. Reproduced with permissions from [80].

exposed. Finally, the particles are allowed to age in the recrystallization phase to reduce defects from all of the coalescence, producing well defined cubic nanostructures (Figure 20d). Upon increasing the injection temperature to 145 °C, smaller initial seeds are generated (Figure 20e). These generated seeds then go through a similar process of OA growth, producing thin {100} FeS_2 nanosheets (Figure 20h, inset is FFT) for the first time. Within the nanosheets at earlier aging time (Figure 20f), the initial seeds can be seen, which then recrystallize to fully crystalline structures by the end of the reaction (Figure 20h), which is similar to the formation of PbS nanosheets by the OA mechanism.[81] These images confirm that the initial seeds do in-fact merge together and do not grow by the classical Ostwald ripening mechanism.

The reaction can also be monitored by Uv-Vis absorbance as shown in Figure 22. By 30 min, the seed particles are all consumed by collision and the spectra slowly shift to the IR as the cubic structures are formed. By 90 min when the cubes are formed, only the cubic absorption at 950 nm is seen.

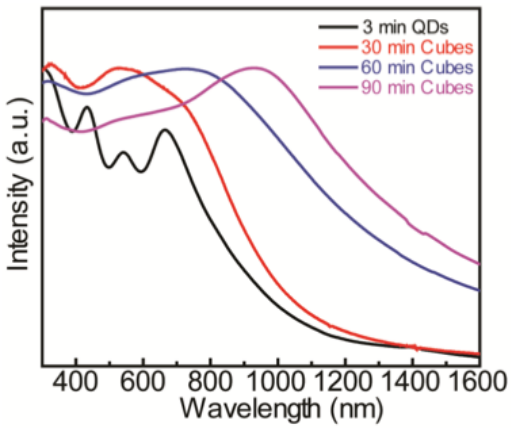

Figure 22. Uv-Vis spectrum for FeS_2 cube formation at different reaction times. Reproduced with permissions from [80].

To explain the differences in formation between the cubes and the nanosheets, the produced seeds must be examined as their surface faces are what control the collision and coalescence. To do this, we utilize Barnard and Russo's theoretical predictions on the different surfaces of pyrite nanoclusters based on size.[52] Within their work they show that

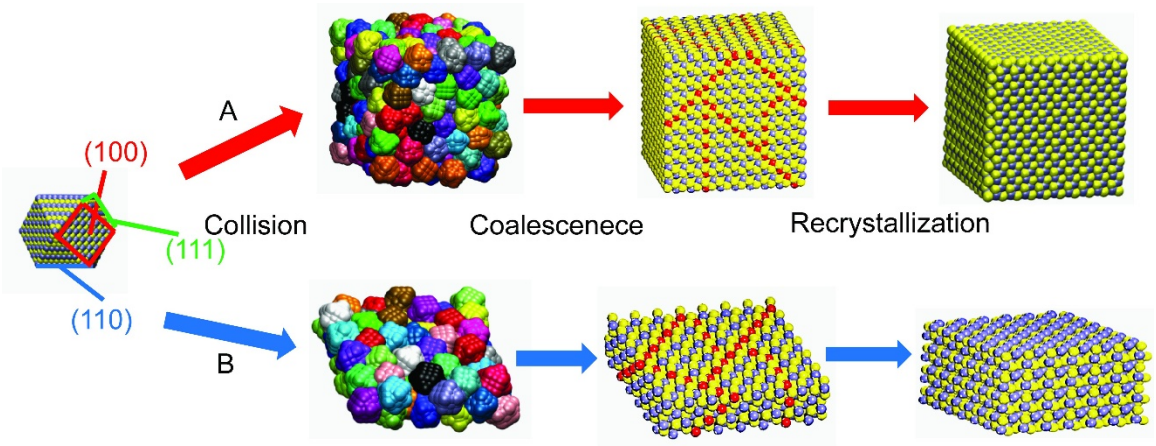

Figure 23. Schematic of the pathways to form (a) Cubic FeS_2 and (b) Nanosheet FeS_2. Reproduced with permissions from [80].

truncated FeS_2 nanoclusters are made up with 6 {100} surfaces, 8 {111} surfaces and 12 {110} surfaces. Up until now the {110} surface was not considered due to this surface is not observed in larger pyrite crystals. Only upon size reduction to nanoclusters, the {110} surface is generated. However the {110} surface plan has the highest surface energy between the other standard pyrite surfaces. Figure 23 shows a schematic of the formation of the two different FeS_2 structures. When considering the cubic formation at lower injection temperatures, the larger seeds are made up with higher {100} surface areas, and when these seeds collide, these surfaces are left exposed due to their lower surface energy (path A, Figure 23). When injection temperature is higher, smaller seeds are formed which exhibit higher {110} surface area. Since the {110} surface of pyrite is energetically unfavorable compared to the other surfaces, these are the faces that combine with each other to reduce the overall energy. This type of coalescence causes the 2D of the nanoplate structures. Interestingly enough, if the nanosheets are allowed more

reaction time, they will slowly grow into cubes. Figure 24 displays TEM images of FeS_2 nanosheets at different reactions times. At 10 min, the standard thin sheets are observed (Figure 24a) and some can be found standing on their side (Figure 24b), highlighting their thin dimension. Upon further reaction time (240 min), the plates are seen to be thicker by darker opacity in the TEM images (Figure 24c). Side view of the particles also confirms growth in the z-direction (Figure 24d). Finally, by the 360 min reaction time, large cubes are observed (Figure 24e,f). This type of growth can be explained by OA growth of the plates on the top {100} surfaces, in order to reduce the surface energy of the particles even further. Control of the initial seeds sizes by the injection temperature is a simple method to control the subsequent OA growth phase. This growth phase then controls which FeS_2 nanoparticle shape that is produced, making it a facile method to control FeS_2 formation.

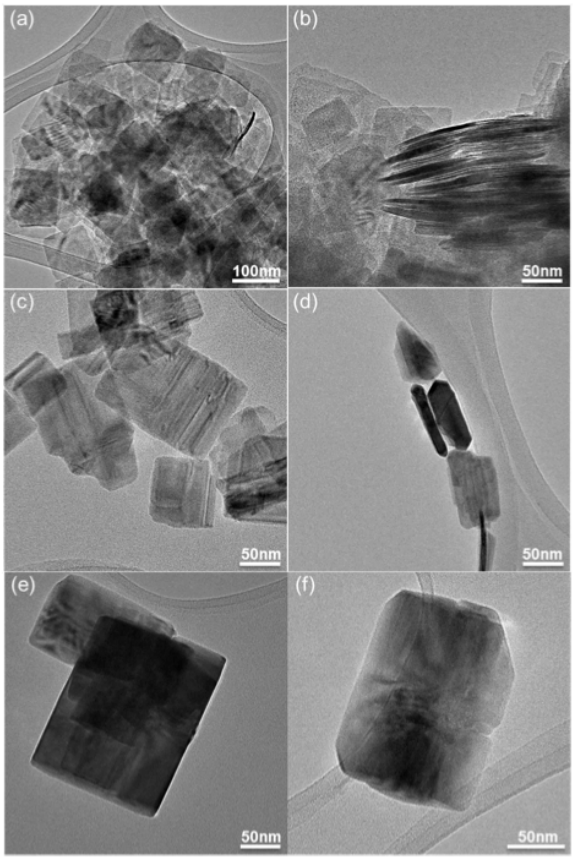

Figure 24. TEM images of FeS_2 nanosheet growth at (a,b) 10 min, (c,d) 240 min, and (e,f) 360 min. Images on right display cross-sectional views of the particles. Reproduced with permissions from [80].

Temperature plays an important role in the kinetics within the OA mechanism of growth. It is suggested that dipole-dipole interactions are responsible for the first collision step of the mechanism.[31] Overcoming this attractive energy will cause the initial seeds to de-adsorb from each other, lowering the amount of coalescing events, resulting in smaller particles. In OA kinetics it has been shown that temperature can provide this extra energy. This effect can be observed in our system by simply increasing the reaction temperature of the FeS_2 nanocube synthesis. Figure 25a-c displays the nanocubes formed

at reaction temperature of 220 °C, 250 °C and 270 °C, respectively. As observed by the size distribution histograms in the insets of each image, a shrinking of the particle sized is observed, confirming a thermal effect on the final size of the particles. Size control will prove useful in fabrication of photovoltaic devices as mentioned before, only ~100 nm of pyrite is required to absorb 90% of light.

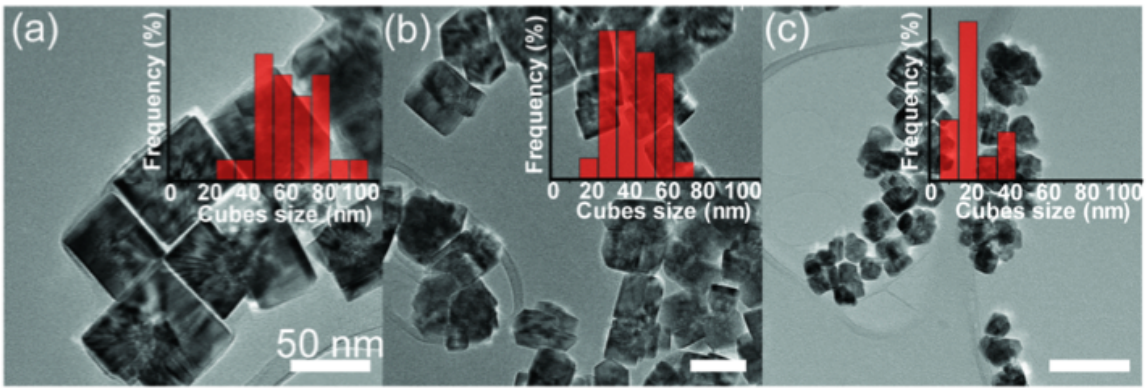

Figure 25. Cubic FeS2 nanoparticles at reaction temperature of (a) 220 °C, (b) 250 °C, (c) 270 °C. Inset is histogram of size dispersion of the nanoparticles. Reproduced with permissions from [80].

Since the OA mechanism can be controlled through injection and reaction temperatures, the reaction time must now be considered. Coalescence between surface faces usually creates defects in the crystal lattice, which are detrimental to charge transport. It will be key to eliminate as many defects as possible within the produced crystals so that the material will be optimal for its uses in photoactive devices. Since defect sites are high energy, it is thermodynamically desired to eliminate them by recrystallization. Recrystallization is achieved by providing the reaction enough energy and time. Simply increasing the final annealing time allows for more recrystallization after coalescence. Figure 26a presents an HRTEM image of FeS_2 cubes at 40 min of

reaction time. Outlined in white are different crystalline domains within one single particle resulting from the OA growth mechanism. Stacking faults are also observed, pointed out by the orange arrows. Upon increasing reaction time to 120 min these defects are minimized, as seen by Figure 26b. The HRTEM image shows a particle with one single crystalline domain, with the FFT showing long range ordering and the very prominent {100} pattern. From this it can be concluded that while collision and coalescence are completely by 40 min, longer reaction times are highly desirable to allow for the elimination of as many defects as possible, producing optimal FeS_2 material.

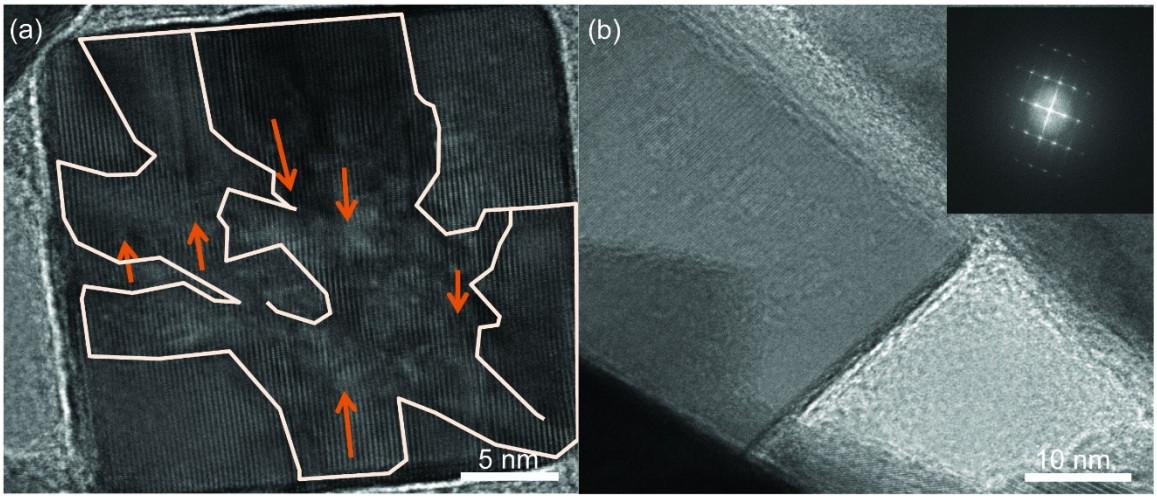

Figure 26. a) HRTEM image of FeS_2 cube with 40 min reaction time. Crystalline domains outlined by white line and orange arrows indicate stacking faults. b) HRTEM of FeS_2 cubes after 120 min of reaction with inset FFT showing long-ranged crystallinity. Reproduced with permissions from [80].

Finally, it was observed that the OA mechanism was not just responsible for the cubic and nanosheet formation, but for all the formations of FeS_2 that we have observed in our studies. Figure 27a-d displays the growth formation of the thick nanoplates created

using $Fe(CO)_5$ as the iron precursor as discussed in section 2.2.2. However, imaging closer to the edge it is apparent that this is only the collision phase (step 2 in Figure 19), as they have not merged yet. Upon further reaction time the large plates coalesce and recrystallize to form the final micron sized plates. FeS_2 nanospheres are also produced the OA mechanism. Figure 27e shows the nanosphere seed particles enter the collision phase and form smaller bunches (Figure 27f,g). These then coalesce and recrystallize producing final nanosphere morphology seen in Figure 27h. Observations of the OA mechanism for all of these nanoparticle shapes indicate that OA is the dominant mechanism responsible for the creation of FeS_2 nanoparticles.

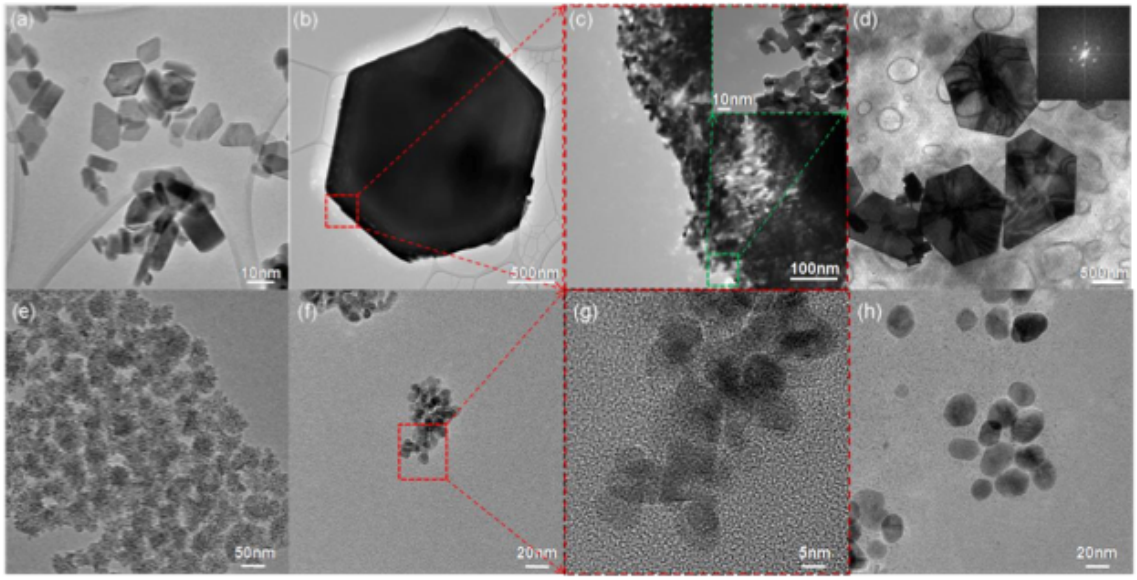

Figure 27. a-d) OA process involving hexagonal plates formed with $Fe(CO)_5$. e-h) FeS_2 nanospheres formation through OA. Reproduced with permissions from [80].

In conclusion, it was found that the OA growth mechanism is responsible for the growth of the FeS_2 nanoparticles. The injection temperature easily controls the shape of nanoparticles, due to the different types of FeS_2 seed particles generated. Size is also

tuned by changing the reaction temperature. Finally, crystallinity can be improved by allowing longer reaction times to allow for recrystallization to eliminate many of the stacking faults and defects. However, due to the OA mechanism there will always be defects and grain boundaries within final pyrite nanoparticles. This discovery has significant impact on utilizing FeS_2 nanoparticles in green photodevices as these defects are death centers for exitons and must be minimized.

2.4 Iron Sulfide Ink for Micron Sized Crystals

The discovery of the OA mechanism for FeS_2 produced questions on the quality of crystallinity of the final nanoparticles due to the defect states that are intrinsically involved because of it. Many other groups became focused on the question if it these defects were the cause of FeS_2 poor performance in photovoltaic devices.[82-84] A new goal was formed for the generation of high quality large crystals for intensive studies. To this end, the challenge to create larger, high-quality FeS_2 crystals was the next synthetic task.

To achieve this goal, new methods have to be developed to create such large crystals, while maintaining ease of scalability. Formation of large pyrite crystals in solution processing methods is difficult. Figure 25 shows that the largest crystals that can be generated are ~80 nm. To create the desired size, a new methodology would have to be used. It is known that pyrite forms through a FeS state.[85] Furthermore, large pyrite crystals have been created previously by vapor growth methods mentioned in section 2.2. Knowing this, development of an iron sulfide (FeS) precursor through solution processing followed by sulfurization to grow large crystals was desirable. To create the intermediate FeS nanowires, a low temperature reaction was used (120 °C, instead of the standard 220 °C). The material generated from this reaction was a dark, viscous material

that was reminiscent of ink when dissolved into chloroform. Figure 28a displays TEM image of the material created, showing dark wires within a matrix, which were deemed FeS nanowires. The inset of the image is SEM image, showing the matrix material is plate like. HRTEM of the wire structures shows very uniform structure and a spacing of 2.7 nm between the wires, shown in Figure 28b. The 2.7 nm spacing corresponds to the length of the ligand ODA that is used as a capping ligand, explaining why the wires form uniformly.[86] The ligand is then what makes up the plate like matrix seen in the SEM. Within the Scanning Transmission Electron Microscope (STEM) image in Figure 28c, the wires are visible within the matrix, indicating they are iron rich, as higher atomic number elements exhibit higher contrast in STEM. The Energy Dispersive Spectroscopy (EDS) spectrum of the wires indicates that the stoichiometry is 1:1 Fe:S and XRD shows no diffraction, indicating an amorphous material (Figure 28d). This FeS ink therefor makes a plausible precursor to generate large FeS_2 crystals.

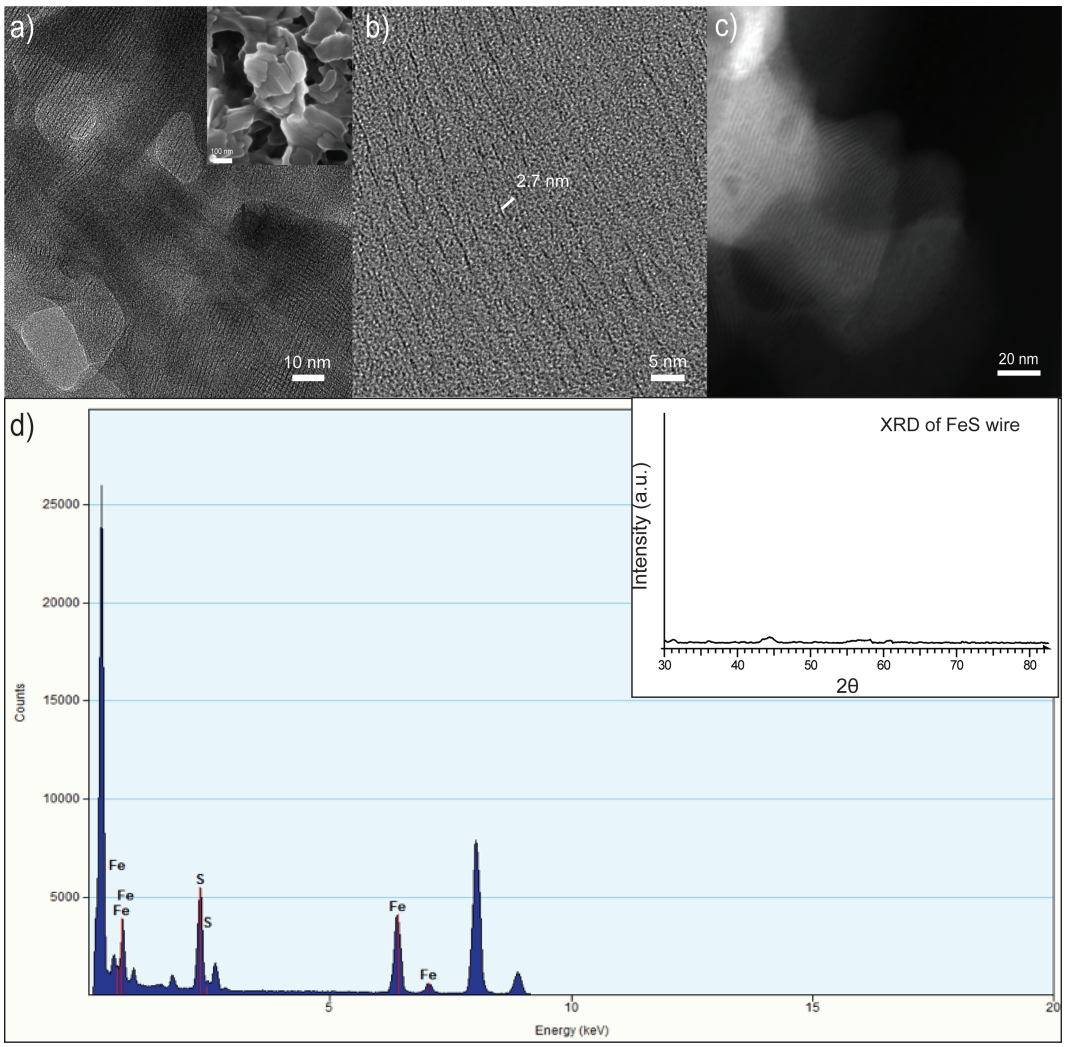

Figure 28. a) TEM of FeS wire structures. Inset is SEM image of wires. b) HRTEM image of wire structures. c) STEM image of wires. d) EDS spectrum of FeS wires. Inset XRD of wires.

To achieve iron pyrite growth, the FeS nanowire ink must be sulfurized to complete the transformation to FeS_2. This is achieved by placing the nanowire material into an ampule with sulfur powder and high temperature annealing. Figure 29a shows a SEM cross-section of the sulfurized nanowire films where large FeS_2 crystals can be seen within and protruding out of the film. A TEM image of an isolated crystal is displayed in

Figure 29b, showing well-defined shape and edges. HRTEM of the FeS_2 shown in Figure 29c shows these FeS_2 are highly crystalline with no stacking faults or defects in the lattice. Distance between lattices measures 5.43 Å, matching well to the lattice constant of FeS_2. The {100} pattern displayed in the FFT in the inset confirms the high crystallinity and explains the final cubic structure obtained. These highly crystalline micron-sized FeS_2 particles show promise to be used in more in-depth studies such as hall measurements and performance as a photovoltaic.

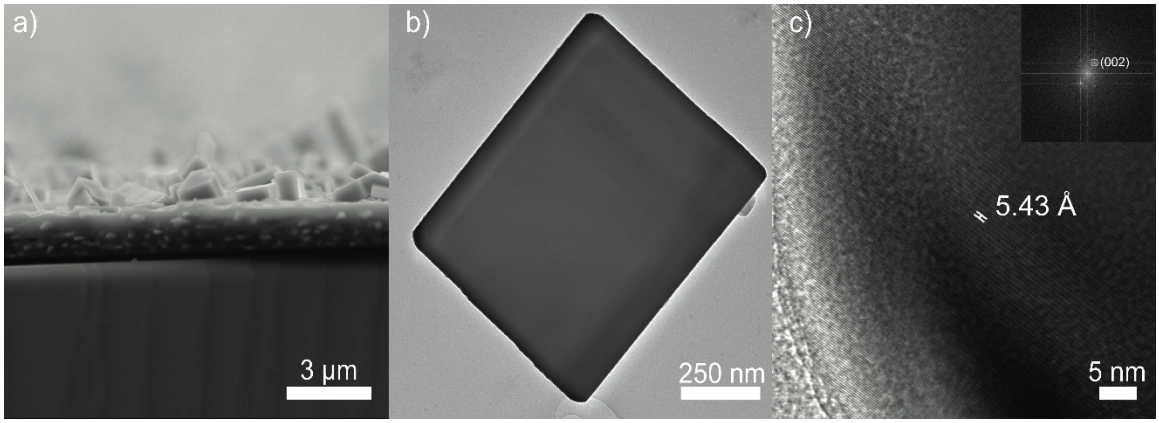

Figure 29. a) Cross section SEM of post sulfurization of FeS films showing micron sized FeS_2 crystals. b) TEM image of a single FeS_2 crystal. c) HRTEM image of FeS_2 crystal produced.

As seen above, the shape and face of FeS_2 have different chemical activities and stabilities. Therefore, controlling the exposed surface and size of the FeS_2 crystals is desirable. It was found that the crystals produced were dependent on temperature of sulfurization with a set growth time of 4 hours. Top-down SEM images of the sulfurized films at variable temperatures are shown in Figure 30a-f, exhibiting different crystal sizes and shapes. At temperatures above 550 °C, the large pyrite crystals appear. At lower

temperatures, only small multi-phased crystallites are formed within the matrix material. XRD confirms only pyrite peaks are exhibited above this critical temperature. Lower temperatures produce multi-phase iron sulfides including marcasite. It is important to note that at 550 °C, almost all of the crystals formed have very defined cubic/rectangle shapes, indicating {100} plane growth. As the sulfurization temperature is raised over 550 °C, the final crystals start exhibiting rounded edges and granular formation. This granular formation is indicative of {111} growth. At 650 °C the matrix material is completely converted to smaller grained crystals. By 700 °C, very large spherical crystals are the only material produced.

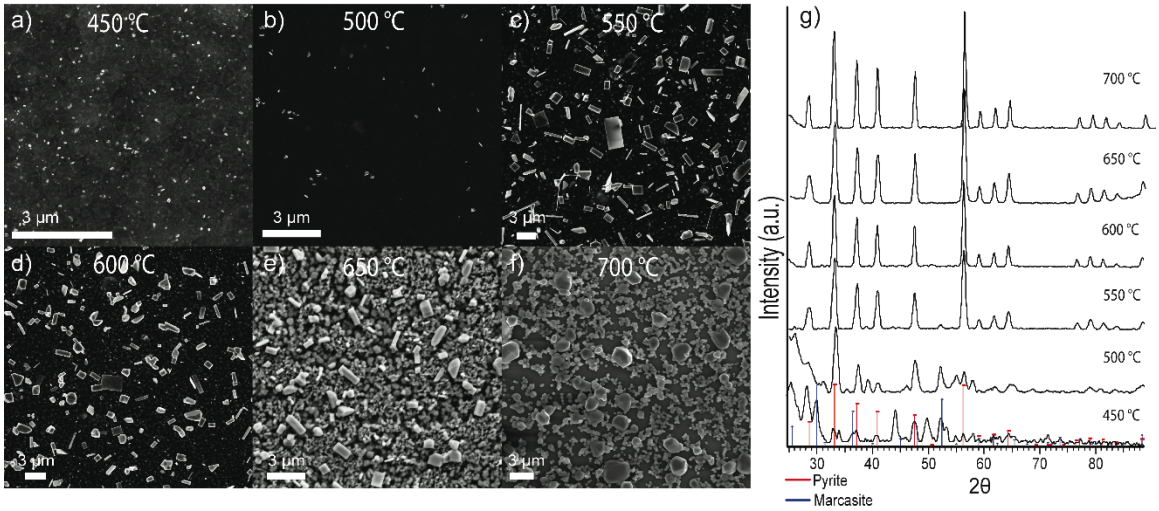

Figure 30. a-f) SEM images FeS_2 crystals at different sulfurization temperatures for 4 hours. g) Corresponding XRD of the FeS_2 crystals.

Sulfurization time was also studied to examine growth kinetics. 500 °C was chosen as the temperature to examine if {100} growth preferred longer reaction times. Figure 31 displays the time dependent FeS_2 crystal growth from the sulfurization of the FeS wire precursor. At early times (4 hours) only very small crystallites form. Longer

sulfurization times yield larger crystals, but they lack a well-defined shape. At 8 hours, the final micron cubic/rectangle FeS_2 crystals appear. This indicates that it is possible to achieve the desired {100} surface dominated pyrite crystals with lower temperatures, although a sulfurization time of at least 8 hours is required.

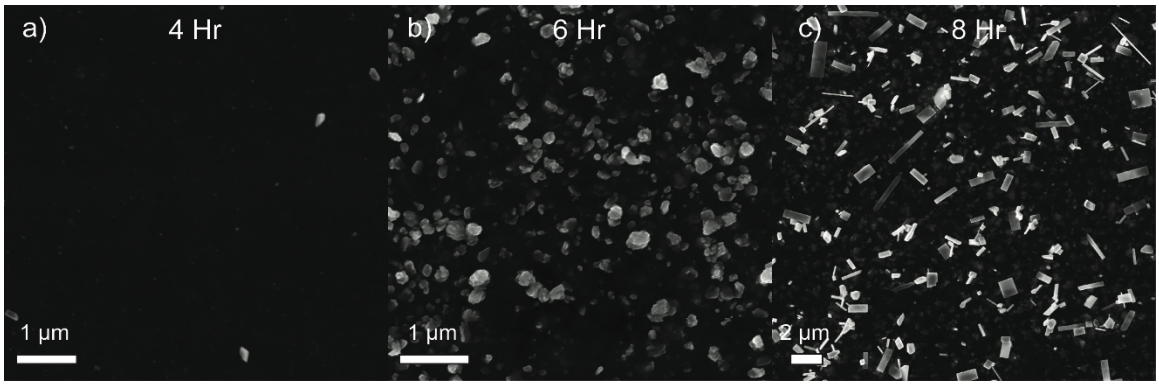

Figure 31. SEM images of sulfurization of FeS wires at 500 °C at a) 4 hours, b) 6 hours and c) 8 hours.

Since the time and temperature growth requirements are understood, a grain growth equation can be used to determine the activation energy of {100} pyrite grain growth, which will be valuable to control other pyrite crystal growth methods. As noted above, the temperature points above 600 °C are left out, due to the {111} becoming the dominate growth direction. Grain sizes were determined by measuring all visible grain edges in the SEM images and then averaged to avoid overestimation of grain growth. Grain sizes versus temperature and time plots are presented in Figure 32a,c, respectively. Note the temperature units are in kelvin for easier usage in the grain growth equations.

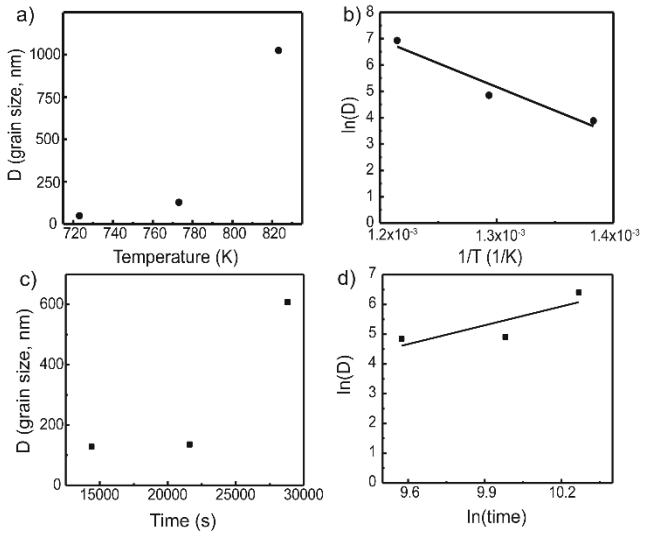

Figure 32. a) Grain size (D) of FeS_2 crystals vs. sulfurization temperature b) Plot of Ln(D) vs. 1/T, c) Grain size of FeS_2 vs. time, d) Plot of Ln(D) vs. Ln(time).

The grain growth empirical equation can be used to explain the growth characteristics under heat treatment can be described as:

$$D^m = Kt \quad \text{(Eq. 3)}$$

where D is average grain size, m is grain growth exponent, K is temperature dependent parameter and t is the annealing time.[87] The grain growth exponent is dependent on the material system and needs to be solved for. The temperature dependent parameter K and temperature (in Kelvin) can be related back to the Arrhenius formula:

$$K = Ae^{(-\frac{Ea}{RT})} \quad \text{(Eq. 4)}$$

where E_a is the activation energy, A is the pre-exponential term, R is the gas constant and T is temperature. Combining the above equations generate:

$$D^m = tAe^{(-\frac{Ea}{RT})} \quad \text{(Eq. 5)}$$

It is obvious by this equation that grain growth can be affected by both time and temperature. Taking the logarithm of this new equation generates:

$$\ln D = (-E_a/mR)(1/T) + (1/m)\ln t + (1/m)\ln A \quad \text{(Eq. 6)}$$

Plotting Ln(D) versus 1/T and fitting to a straight line (Figure 32b) generates the equation: y=-17997x + 28.564, which is the temperature dependent growth equation. Here, the slope equals -17997 = ($-E_a$/mR)

Considering the time dependent growth where temperature is now constant, it is possible to plot Ln(D) versus Ln(t) (Figure 32d). Fitting to a straight line generates the equation: y=2.1109x-15.595 where the slope equals (1/m) = 2.1109 or m = 0.4737. With both m and ($-E_a$/mR) known, E_a can be determined to be 7088 J/mol, or ~71 kJ/mol. This value matches nicely (73 kJ/mol) to previously determined {100} growth activation energy using MOCVD methodologies.[88]

In conclusion, a simple FeS nanowire ink precursor has been developed that can be utilized to generate high-quality micron sized iron sulfide crystals. It was found that both temperature and time affected the types of pyrite crystals generated. If {100} surface are desired, a temperature of 550 °C can be used. If {111} dominated surfaces are the goal, higher temperature (700 °C) is needed. Growth activation energy of the {100} surface was also determined to be 71 kJ/mol, matching nicely to other pyrite crystal growth methods.

2.5 Conclusion

Iron pyrite has many different promising attributes to be used in green-energy applications such as a photovoltaic semiconductor, photodetector material, or as an earth abundant photocatalyst. I have presented simple methodologies to control the shape and

size of iron pyrite nanoparticles. It has also been discovered that pyrite does not grow by the classical Ostwald Ripening mechanism, but instead goes through OA to form final nanoparticles. The OA mechanism can then be tuned by injection temperature and reaction temperature to control the shape of the nanoparticles. However, the mechanism by which orientated attachment happens includes intrinsic defects within the crystal lattice such as stacking faults and grain boundaries. Longer reaction temperatures improve the final crystallinity, however surface and internal defects still may be present. To overcome this problem, a FeS nanowire ink was developed to generate high quality micron sized FeS_2 crystals that can be used for more in-depth studies to discover whether pyrite will be able to be utilized as a green material, or will live up to its name of "fool's gold".

2.6 Materials and Methods

Standard synthesis of FeS_2 nanocrystals starts with 0.5 mmol Iron precursor ($FeCl_2$ (99.99%, Sigma), $Fe(acac)_2$ (99.95%, Sigma), $Fe(CO)_5$ (99.99%, Sigma)) and 12 g octadecylamine (ODA, 90% technical grade, Sigma) were loaded into a three-neck flask. The flask is then degassed by pulling vacuum and back purging with argon gas three times. The flask is then heated to 120 °C for one hour to dissolve the precursor and melt the ODA. Another three-neck flask is then loaded with 4 mmol sulfur powder (colloidal, Sigma) and 5 ml diphenyl ether (99%, Sigma) and is degassed by vacuum/argon purge three times and heated to 70 °C to dissolve the sulfur powder. Depending on desired particle shape, the iron precursor flask is then kept at 120 °C (cubes), or raised to 145 °C (nanosheet), 175 °C (popcorn) or 220 °C (nanosphere). Then sulfur solution is rapidly injected into the iron precursor flask. For different precursor shapes, such as thin

nanoplates ($Fe(acac)_2$) and thick nanoplates (($Fe(CO)_5$), an injection temperature of 220 °C was used. The solution was then brought up to 220 °C (or higher to achieve smaller sized cubic structures) and allowed to react for desired amount of time. To generate FeS wires, a 120 °C injection temperature was used and temperature was not allowed to be raised after injection and was only reacted for 10 min. After the allotted time, the reaction vessel was removed from heat and allowed to return to room temperature. 2 mL of methanol (99.8%, Sigma), was injected at around 100 °C to keep the ODA from solidifying. The final solution was transferred to centrifuged tubes and chloroform (99% anhydrous, Sigma) and methanol were added. This solution was then centrifuged for 10 min at 4000 rpm to crash out the FeS_2 particles. The top solution was poured off and this washing with methanol/chloroform was repeated 2 more times to remove any excess ligand. Particles were either stored dry or dissolved in chloroform in the drybox, depending on desired use.

For the photodegradation of methyl orange experiments, 0.09g of nanoparticles were dissolved in 10 mL of a 30 mg/L aqueous solution of methyl orange (ACS reagent 85%). This solution was sonicated for 5 min in the dark and put into a black box with stir plate and xenon light source. The vial was put 7 mm away from the xenon bulb, which power was measured to be 46 mW/cm^2 by a power meter. 200 μL aliquots where taken at 10 min time intervals and then diluted with 400 μL of water and absorbance was taken.

Sulfurization of nanowire ink to achieve micron sized pyrite crystals was achieved by first creating films on simple silicon substrates. 40 μL of a 15 mg/L solution (in chloroform) was drop-casted onto clean silicon substrates and allowed to dry. These substrates where then loaded into a glass ampule with 100 mg of sulfur powder within.

This ampule was then sealed under nitrogen environment with an oxygen/gas torch. The ampule was then loaded into a tube furnace and heated to desired temperature and time.

All Uv-Vis spectra were obtained on a UV-3600 Shimadzu Uv-Vis-NIR spectrophotometer. X-ray powder diffraction was done at room temperature using monochromated Cu-Kα radiation on a Brukerproteum diffraction system equipped with Helios multilayer optics, and APEX II CCD detector and a Bruker MicroStart microfocus rotation anode x-ray source operating at 45 kV and 60 mA. Powders were suspended in Paratone N oil and placed into a nylon loop and mounted on a goniometer head. Transmission electron microscope (TEM) images were obtained using a field emission FEI Tecnai F20 Xt. Scanning electron microscope (SEM) images were obtained using a LEO 1550 field emission SEM.

3 Synthesis of Core/Shell Iron/Iron Palladium Nanoparticles

3.1 Introduction

3.1.1 Motivation

Now that I have presented the work on the various methods of generation of the non-toxic energy-critical semi-conductor Iron Pyrite, I will move onto studies of generation of magnetic nanoparticle systems. As stated in 1.2.2, high-energy magnetic systems are needed for the new magnet turbine systems. However, all known high-energy systems utilize RE elements. Finding a way to generate high-energy magnetic systems without the use of RE elements would hugely impact the economic feasibility of wind energy.

In 1993, Skomski and Coey proposed utilizing two phase nanostructured magnets to further increase the variety of high-energy magnetic systems, and maybe even eliminating the need for RE elements.[89] These became known as exchange-coupling magnetic composites. These exchange-coupled magnets are composed of two phases; first phase being soft magnetic material with high M_s, for example Co, Fe, FeCo. The second phase is composed of a hard magnetic material with high H_c (MnBi, $L1_0$ FePd). If these two phases are brought into close contact (~10-20 nm), the hard magnetic material can "pin" the soft materials spin orientation, which will generate a composite with the high M_s of the soft magnet, and the high H_c of the hard magnet. The key to exchange-coupling is to control the phases in an ordered manner to maximize an optimal distance between the hard and soft magnetic phases. Exchange-coupling composites therefore can expand the diversity of high-energy magnets and may even eliminate the need for RE

elements. Within Skomski and Coey's first theoretical report, they suggested a possible optimized structure of a nanocomposite composed of two different magnetic materials to create optimal interaction between the phases.[89] Figure 33 displays their proposed structure. However, they suggested that a lamellar structure of the two phases would be more easily obtainable with the technology at the time, such as the many vapor deposition or sputtering techniques. With emerging nanotechnology, this structure could be more easily obtainable due to precise control of core/shell structures and self-assembly processes.[90-94] One can imagine creating a magnetically hard spherical core structure, followed with a deposition of a magnet shell with varying thickness could generate such a structure after annealing to merge the particles together.

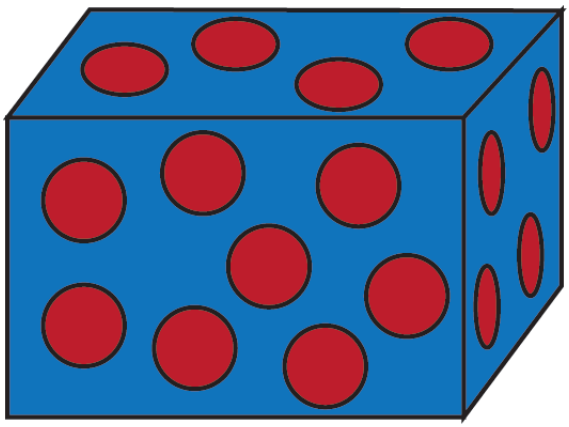

Figure 33. Suggested optimized structure of two-phase magnet for exchange-coupling with red being the hard phase and blue being the soft phase matrix.

The first attempts at utilizing nanoparticles to generate an exchange-coupled nanocomposite was by Zeng et al. in 2002.[27] Zeng and colleagues used FePt and Fe_3O_4 nanoparticles to create self-assembled films by solvent evaporation, followed by

reductive annealing to reduce the iron oxide and convert the FePt to a $L1_0$ structure. $L1_0$ FePt plays the role of the hard magnet phase due to its high K_u constant of $7x10^6$ J/m^3. It was found that after annealing the two phases, interdiffusion of the now zero-valent iron from Fe_3O_4 into the FePt phase created a Fe_3Pt soft phase. Unfortunately, this soft phase exhibits a lower M_s than of a pure α-Fe phase, reducing the overall performance. To overcome this issue, several groups tried replacing $L1_0$-FePt with $L1_0$-FePd structures. There are two benefits to this switch; one is that palladium is a cheaper metal than platinum but still possesses a competitive K_u of $1.x10^6$ J/m^3 as compared to the $7x10^6$ J/m^3 of $L1_0$-FePt. Secondly, there is a thermodynamic stability within the phase diagram that allows for the generation of a solid mixture of both $L1_0$-FePd and α-Fe. Recently Teranishi et al. have shown that it is possible to first create Pd nanoparticles and with a sequential synthesis, anisotropically grow Fe_3O_4 nanoparticles next to them.[91] These composites then can be reductively annealed to induce interdiffusion of the Fe into the Pd and generate the desired $L1_0$-FePd/α-Fe nanocomposites. However, this synthesis is tedious as it requires two different syntheses and lacks precise placement of the two magnetic phases. It would be desirable to develop a one-pot method that generates FePd cores and an iron oxide shell with control of the shell size.

3.2 Interdiffusion Induced Exchange-Coupling of $L1_0$-FePd/ α-Fe Magnetic Nanocomposites

3.2.1 Synthesis of FePd and FePd/Fe_2O_3 Core/Shell Nanoparticles

To meet the challenge of creating a one-pot method to generate a final $L1_0$-FePd/α-Fe nanocomposite, first a method to control the core FePd particles is needed. While there are few FePd nanoparticle synthesis methods in the literature, each exhibits their

own drawbacks. Hou's et al. method suffer from poor size range of the final FePd particle while Kang's et al. method use lithium triethylborohydride, a harsh reducing agent.[95, 96] However, control of pure palladium nanoparticle synthesis is well known, with phosphine head ligands providing excellent control of size and simple reduction by oleylamine.[97] It has also been found that interdiffusion of Fe into cobalt nanoparticles is possible, producing FeCo nanoparticles.[98] Taking into account this knowledge, it is possible that FePd particles could be created via interdiffusion starting with well-controlled Pd cores. First, it is important to show the requirement of a stabilizing ligand in the Pd core synthesis. Figure 34 shows a TEM image of the Pd nanoparticles created with just oleylamine, which displays no control on size or shape, demonstrating that a stabilization ligand is required.

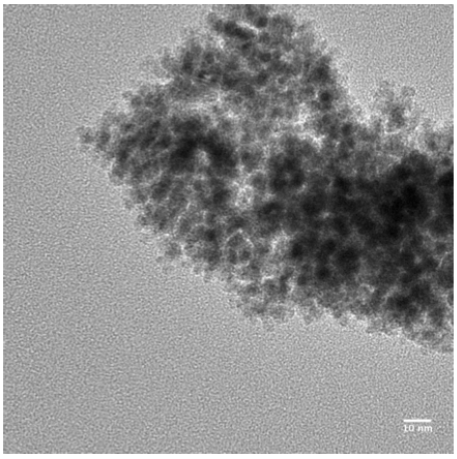

Figure 34. TEM image of Pd nanoparticles synthesized without TBP ligand. Reprinted with permission from [99]. Copyright 2015 American Chemical Society.

With the addition of Tributylphosphine (TBP) as a stabilizing ligand it was found that the particle size could be controlled. Figure 35a-d displays TEM images of the initial Pd cores with different TBP:Pd molar ratios. At 0.5:1 TBP:Pd, the Pd particles produce

aggregated larger particles with a high size distribution, indicating that there is an insufficient amount of stabilization ligand. Upon increase to 1:1, 2:1 and 4:1 TBP:Pd, the Pd cores show a spherical shape and a decrease in size to 6, 4, 2 nm respectively. A decrease in size distribution is also observed. This trend has also been seen with other systems, such as Ni nanoparticles.[82] When one molar equivalent of $Fe(CO)_5$ is decomposed over the initial Pd cores and allowed to anneal in-pot, final FePd particles are seen to grow in size as the Fe is included into the cores while maintaining a small size distribution. Figure 35e shows a graph of both Pd cores and FePd after Fe incorporation

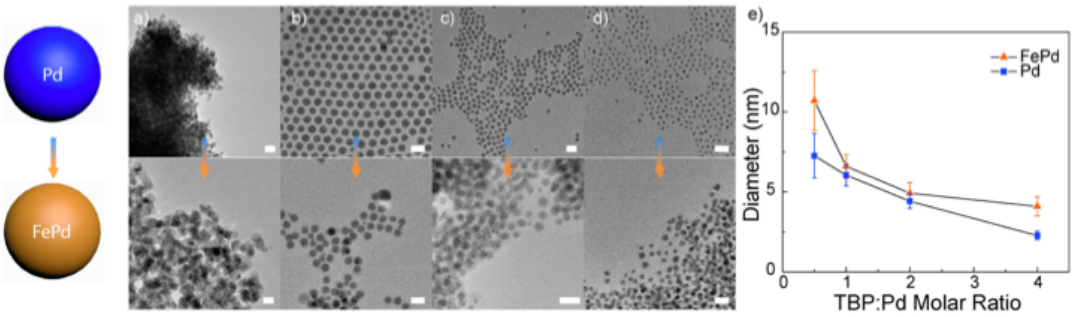

Figure 35. Pd cores with TBP:Pd molar ratios of (a) 0.5:1, (b) 1:1, (c) 2:1, (d) 4:1 and the final FePd particles created after $Fe(CO)_5$ addition. e) Displays a graph of diameter of both Pd cores and FePd particles versus different TBP:Pd molar ratios. Scale bars are 10 nm. Reprinted with permission from [99]. Copyright 2015 American Chemical Society.

dependent on TBP:Pd ratios. It is likely that the size is increased due to Fe diffusion. XRD can be used to help confirm that after Fe addition the Pd cores transform into FePd particles. Figure 36 shows XRD spectra of the Pd cores and the final FePd, matching well to the respective alloy. A thermal diffusion argument can also be used to help boost the

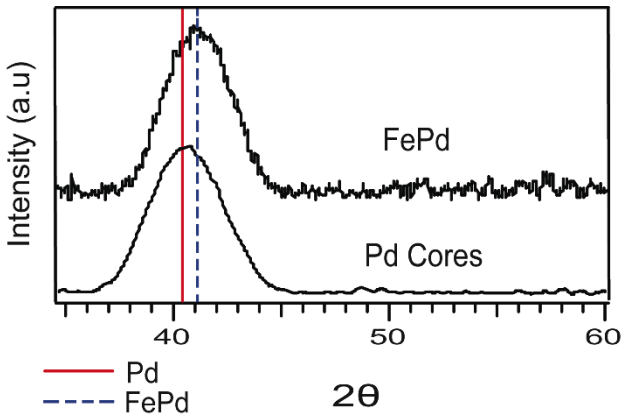

Figure 36. XRD of Pd cores and FePd particles formed after Fe injection. Reprinted with permission from [99]. Copyright 2015 American Chemical Society.

confidence that the Fe is indeed alloying into the Pd cores. Using Fick's first law, the diffusion of metals can be related to an Arrhenius-type equation as such: [100]

$$D = D_0 e^{(-E_a/RT)} \quad \text{(Eq. 8)}$$

where D is the diffusion coefficient at temperature T in kelvin, D_0 is the standard diffusion coefficient for the metal which is reported in cm^2s^{-1}, E_a is the activation energy for diffusion through the desired metal in kJ/mol, and the R is the gas constant. The length covered by diffusion in a given time interval can be calculated using the equation:

$$L = \sqrt{2Dt} \quad \text{(Eq. 9)}$$

where L, D and t are length diffused, diffusion coefficient and time respectively. Combining Eq. 5 and Eq. 6 a new equation is produced:

$$L = \sqrt{2D_0 e^{(-\frac{E_a}{RT})} t} \quad \text{(Eq. 10)}$$

Crystalline Fe diffusion into crystalline Pd has a D_o is 0.95 cm^2s^{-1} and E_a of 262 kJ/mol.[100] Using these numbers, the length of crystalline Fe diffused through crystalline Pd at 1 hour reaction time (the amount of time allowed for Fe annealing) and a

temperature of 493 K (250 °C, reaction temperature used) it is found that a slow diffusion process is seen, only being able to diffuse ~0.00012 nm. This is a basically non-existent diffusion of crystalline Fe into crystalline Pd. Fortunately, the Pd nanocores are polycrystalline, with defects and grain boundaries. It is well known that diffusion of metals occurs much faster at defect and grain boundary sites. Assuming 100% defect sites, the activation energy is only 40 kJ/mol. If we assume that the Pd cores are 100% grain boundaries, the same temperature and reaction time allows Fe to diffuse 6.0×10^6 nm. While both of these cases are obviously extreme exaggerations, it is completely feasible that the Fe can indeed diffuse the 5 nm into a polycrystalline Pd core. Moreover, if we utilize the 5 nm as a diffusion length, it is possible to back calculate a rough E_a of Fe diffusion into these Pd cores, which is found to be 156 kJ/mol. Using this E_a it is possible to calculate the time needed to diffuse into any size of different Pd nanocore.

While this method shows that FePd nanoparticles can be achieved through interdiffusion, the synthesis becomes more interesting with addition of higher amounts of $Fe(CO)_5$. Using Pd cores with a 2:1 TBP:Pd ratio, Figure 37a-d shows that upon further addition of Fe concentration, a Fe_2O_3 (Hematite) shell starts to form over the FePd cores, seen as the lighter phase around the particles. It is thought that once the FePd cores reach a 1:1 stoichiometric ratio, the excess Fe creates this observed shell due to the unique FePd phase diagram.

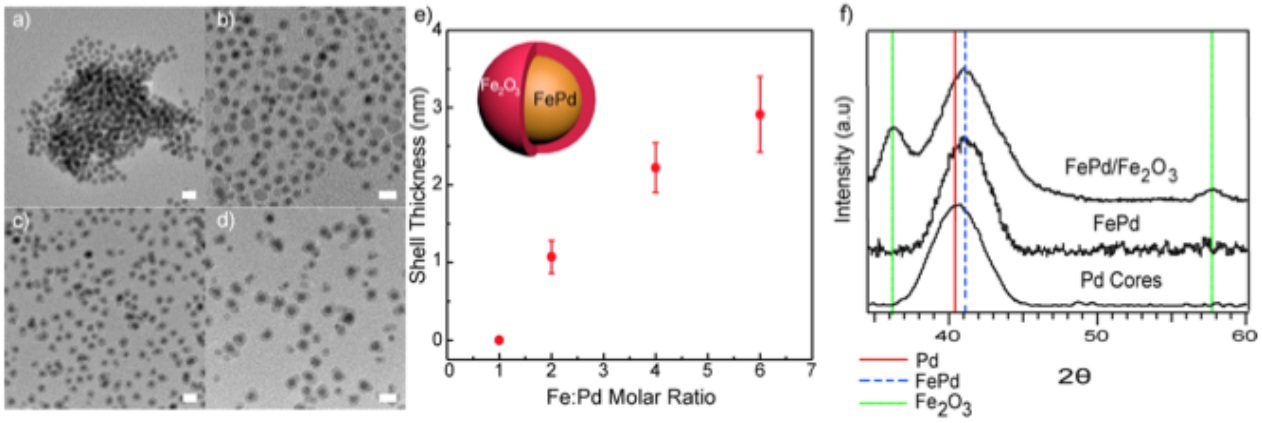

Figure 37. TEM images of particles produced with (a) 1:1 Fe:Pd, (b) 2:1 Fe:Pd, (c) 4:1 Fe:Pd, (d) 6:1 Fe:Pd. e) Graph of Fe_2O_3 shell thickness dependent on Fe:Pd ratio used. f) XRD spectrum with added core/shell FePd/Fe_2O_3 diffraction. Scale Bars are 10 nm. Reprinted with permission from [99]. Copyright 2015 American Chemical Society.

It was observed that the shell thickness could also be controlled with addition of more $Fe(CO)_5$. The graph in Figure 37e shows Fe_2O_3 shell thickness dependent on excess iron added. With a 2:1 ratio, the shell only reaches ~1 nm, while increasing to 4:1 and 6:1, the shell can grow to 2 and 3 nm respectively. When 6:1 is used, other small Fe_2O_3 particles can form, indicating that the max shell thickness obtainable is ~3 nm. This is most likely due to the strain caused between the lattice mismatch of the core and shell material. New peaks arising in XRD confirms Fe_2O_3 shell formation as seen in Figure 37f. HRTEM was also taken for the core/shell particles (Figure 38a) with the shell

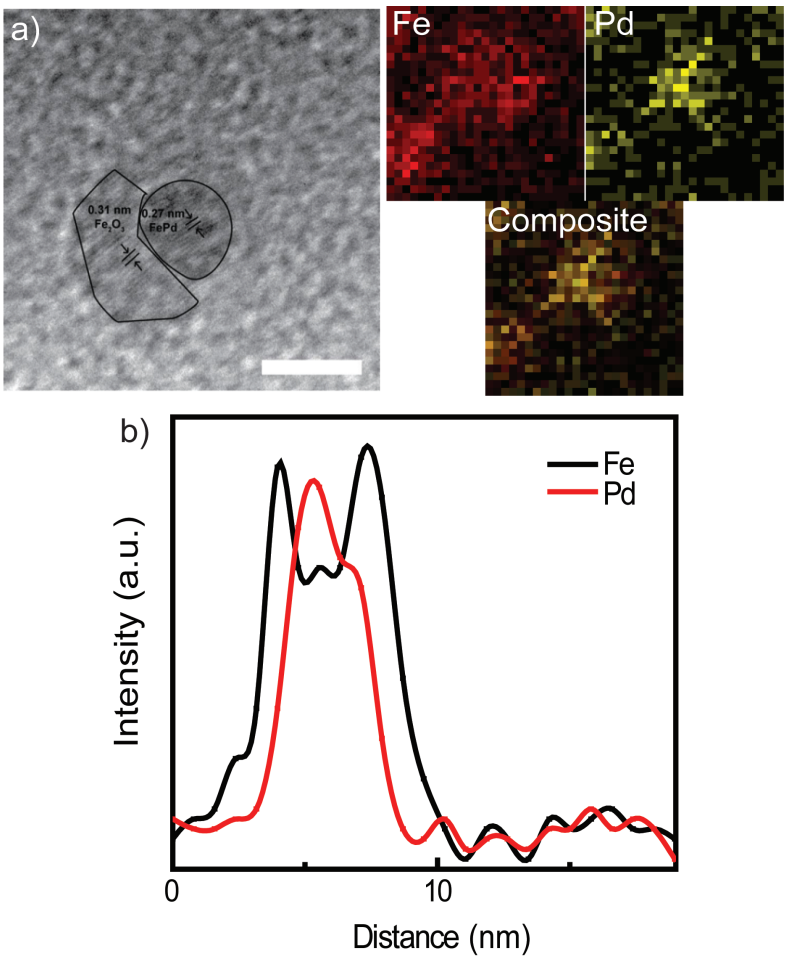

Figure 38. a) HTEM and corresponding elemental mapping of the Core/Shell FePd/Fe_2O_3 nanoparticles. b) Elemental line scans over the Core/Shell particles. Scale bar is 5 nm. Reprinted with permission from [99]. Copyright 2015 American Chemical Society.

lattice measuring 0.31 nm, matching the (220) spacing of Fe_2O_3. Core lattice within the same image measures 0.27 nm, matching the (111) FePd spacing. Elemental mapping and elemental line scans of a single core/shell particle are also shown in Figure 38 displaying high concentrations of Pd within the core and Fe concentration distributed throughout. These measurements support the conclusion that the Core/Shell structures are indeed FePd/Fe_2O_3. EDS was used to study the effects on the relative Fe/Pd ratios of the

core/shell nanoparticles with the addition of more iron precursor. It is observed that with the addition of more $Fe(CO)_5$, the intensity of the iron peak in Figure 39 grows. Stoichiometry of the system was determined by EDS and was found that it produced $Fe_{57}Pd_{42}$, $Fe_{70}Pd_{30}$, $Fe_{76}Pd_{24}$ and $Fe_{82}Pd_{18}$ for 1:1, 2:1, 4:1 and 6:1 Fe:Pd molar ratio synthesis respectively. Stoichiometry will be helpful when analyzing the final

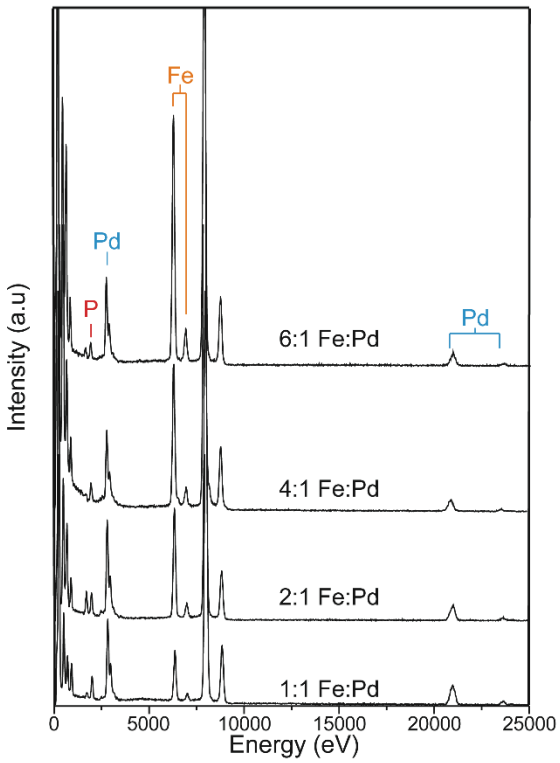

Figure 39. EDS spectra of the different Fe:Pd molar ratio syntheses. Reprinted with permission from [99]. Copyright 2015 American Chemical Society.

magnetic properties of each of these systems. With closer inspection of the EDS spectra in Figure 39, a phosphine peak is observed within all of the systems. This is concerning, as it is known that Fe_2P can be created with phosphine ligand and an iron precursor at elevated temperatures.[101] Therefore, the synthesis must be optimized to reduce the amount of phosphine brought along after synthesis.

As stated above, the TBP ligand is required for shape control of the final $FePd/Fe_2O_3$ core/shell particles. But care must be taken to reduce the amount of phosphine brought into the thermal annealing step as Fe_2P is a nonmagnetic phase and will be detrimental to the final magnetic properties of the nanocomposites. To study the effects of phosphine inclusion, synthesis of the 2:2:1 Fe:TBP:Pd molar ratios with different reaction temperatures was conducted. Reaction temperatures were varied from 190 °C to 290 °C and the particles produced are displayed in Figure 40a-d. Here, all of the particles exhibit core/shell structures, however a trend in phosphine incorporation is observed in the stoichiometry obtained by EDS shown in Figure 40e. As the temperature of the reaction is increased, a higher concentration of phosphine is included in the final stoichiometry. The corresponding M-H loops of these particles after reductive annealing at 500 °C confirm the detrimental effect of the inclusion of phosphine. At the highest concentration of phosphine (290 °C reaction temperature) the M_s of the nanocomposite is almost completely destroyed when compared to the other nanocomposites. Synthesis at 190 °C has the lowest phosphine concentration, but still exhibits a lower M_s than the 220 °C reaction. This is due to incomplete decomposition of the $Fe(CO)_5$ at this temperature, which is observed as a yellow supernatant when cleaning up the particles. Less $Fe(CO)_5$ decomposed lowers the M_s due to less iron included in the final particles. From these experiments it is apparent that the optimal reaction temperature is 220 °C for this reaction and that special care must be taken when considering TBP for a ligand when working with an iron based material system. Now that the reaction temperature is optimized, the effect of Fe:Pd ratios on final nanocomposites magnetic performance must be examined.

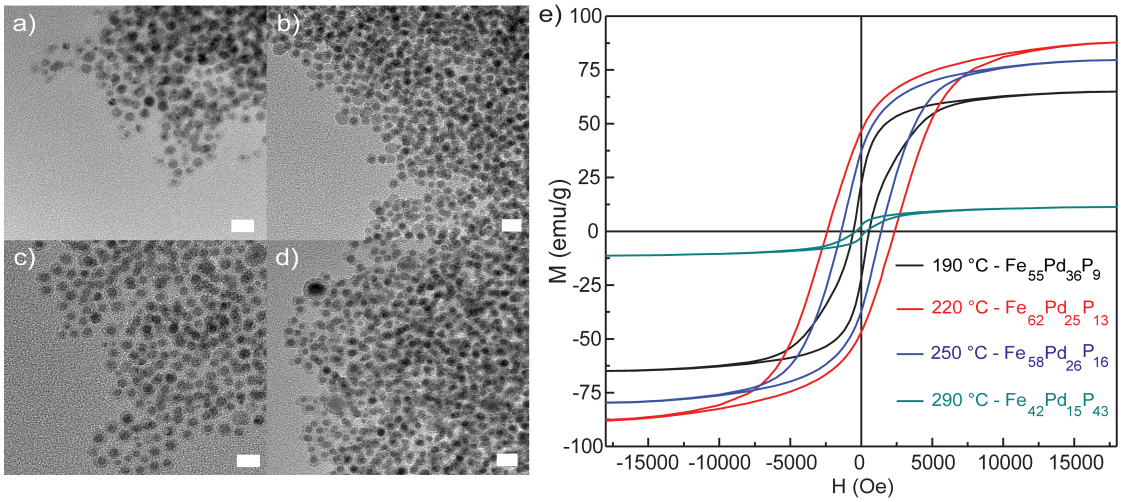

Figure 40. TEM images of $FePd/Fe_2O_3$ core/shell particles with different reaction temperatures of a) 190 °C, b) 220 °C, c) 250 °C, d) 290 °C. e) M-H loop of reductively annealed particles with stoichiometry determined by EDS. Scale bars are 5 nm. Reprinted with permission from [99]. Copyright 2015 American Chemical Society.

3.2.2 Generation of $L1_0$ FePd/α-Fe Nanocomposites Via Reductive Annealing.

The now optimized $FePd/Fe_2O_3$ core/shell nanoparticles are a good foundation to create final FePd/α-Fe nanocomposites through reductive annealing in a 10/90 H_2/N_2 atmosphere at 500 °C. 500 °C was chosen as the annealing temperature, as other studies have shown that 500 °C produced the highest $L1_0$ ordering of FePd and is enough to reduce iron oxide.[93, 97] If a higher temperature is utilized, formation of face-centered cubic FePd becomes a competitive phase, which reduces the coercivity of the overall composite. XRD spectra of the annealed particles are displayed in Figure 41. First there is complete conversion of Fe_2O_3 to the α-Fe phase. Secondly FePd converts to a $L1_0$ structure with the (200) and (002) peak formation after annealing. Finally, as the Fe:Pd

ratio grows, the α-Fe peaks grows, following the trend in the EDS data of more Fe incorporation. Using the well-known Scherrer equation, a rough calculation

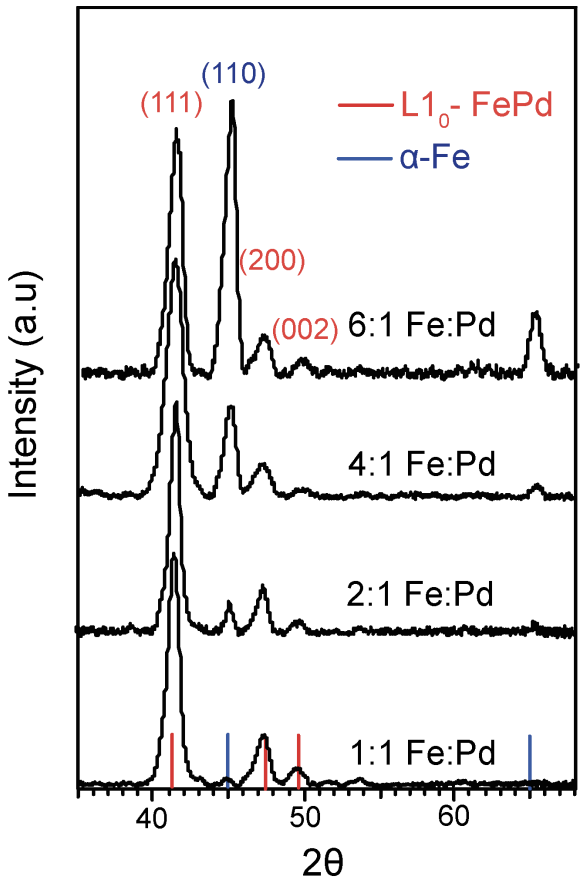

Figure 41. XRD spectra of reductively annealed FePd/Fe_2O_3 core/shell particles with different Fe:Pd molar ratios. Reprinted with permission from [99]. Copyright 2015 American Chemical Society.

of the domain sizes of each phase can be solved for. The Scherrer equation is as follows:

$$\tau = K\lambda/\beta cos\theta \qquad \text{(Eq. 11)}$$

where τ is mean size of the crystalline domains, K is a dimensionless factor (where 0.9 was used as it is the value for spherical-like domains), λ is the wavelength of the x-ray used, β is the full width at half max of the peaks in radians and θ is the Bragg angle.

Solving for the (111) FePd and the (110) α-Fe peak in the 2:1 Fe:Pd sample, rough average domain sizes are seen to be 60 nm and 76 nm respectively. These sizes are much larger than the starting 7 nm particles produced, which warrants investigation of the post-annealed nanocomposites.

Interfacial contact and domain sizes of the post-annealed $L1_0$ FePd/ α-Fe nanocomposites can be accomplished by TEM imaging. Low-resolution TEM images in Figure 42a shows that after reductive annealing the composite displays large domains compared the starting core/shell nanoparticles as seen in Figure 37b. The domains can be roughly identified by the contrast, as the darker domains are most likely the FePd phase as Pd possesses a higher atomic number (Z). Elemental mapping of the black square within the image shows that there are indeed two different phases within the material. Fe signal is seen throughout all of the particles, where the Pd is only in the darker contrast areas, indicating two different phases. The phosphine signal overlaps exclusively on sections where there are no Fe and Pd overlap, further confirming that even with optimization, phosphine will still be included within the final Fe phase. Measuring multiple domain sizes, an average size of 58 and 70 nm for the $L1_0$ FePd and α-Fe is observed, matching well to what was solved for in the Scherrer's equation above. The growth of the domain sizes must occur through coalescence of the different phases during the high temperature annealing. Even so, there is still intimate contact on the nanoscale between the two phases, as seen in the HRTEM image displayed in Figure 42b. Elemental mapping of the section is shown to the right, with the composite of the two metal signals confirming close contact of the separate phases. Lattice spacing in the $L1_0$-FePd phase is 0.38 nm, matching to the {001} lattice and spacing in the α-Fe phase which

measures 0.20 nm, corresponding to the {111} lattice. Now that we have confirmed contact between the phases even with growth of the domain sizes, the magnetic properties of the exchange-coupled nanocomposites need to be examined.

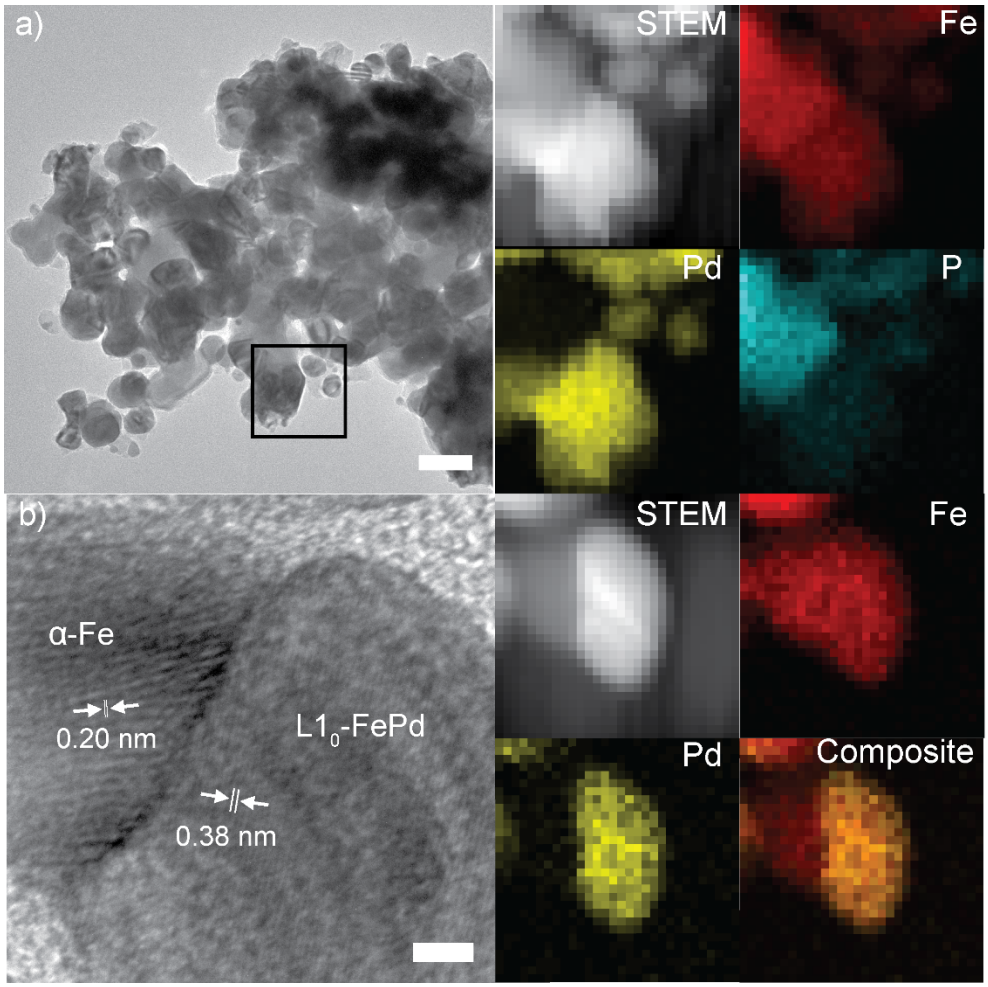

Figure 42. a) Post annealed $L1_0$ FePd/α-Fe nanocomposites (Scale bar is 50 nm). Elemental mapping of the black square is presented next to TEM image. b) HRTEM image of an interface between the $L1_0$ FePd/α-Fe phases with elemental mapping presented to the right. (Scale bar is 5 nm). Reprinted with permission from [99]. Copyright 2015 American Chemical Society.

M-H loops of the annealed exchange-coupled $L1_0$ FePd/α-Fe nanocomposites with different Fe:Pd ratios are shown in Figure 43a. Each hysteresis loop exhibits smooth transformations, with no kinks observed, which demonstrates efficient coupling between the two magnetic phases. The trend in both M_s and H_c is better displayed in the graph of Figure 43b. It is observed that at lower Fe:Pd ratios, H_c is the highest. As more of the soft magnetic α-Fe phase is included, the H_c drops. However, with this drop in H_c, an increase of M_s is seen. The nanocomposite created with a 2:1 Fe:Pd ratio shows the best compromise of magnetic properties, displaying a H_c of 2.2 kOe and a M_s of 91 emu/g. The decrease in H_c seen in higher Fe:Pd ratios is most likely due to excessive Fe doping within the $L1_0$ FePd as seen in other studies.[92] Control of the magnetic properties of these exchanged-coupled nanocomposites is achieved by precursor concentration modifications.

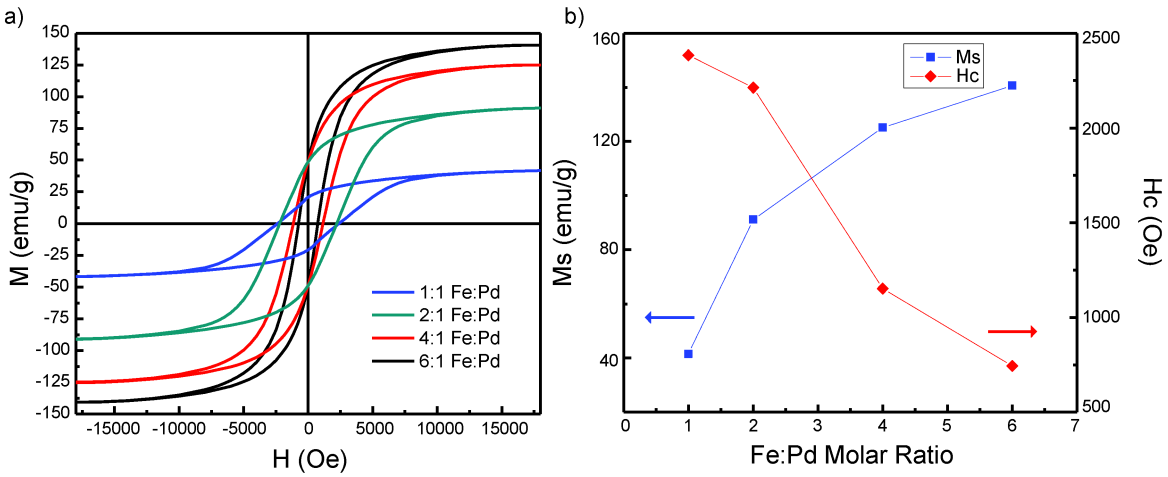

Figure 43. a) M-H loop of the annealed $L1_0$ FePd/ α-Fe nanocomposites with different Fe:Pd molar ratios. b) Graph summarizing both M_s and H_c of nanocomposites with

different Fe:Pd molar ratios. Reprinted with permission from [99]. Copyright 2015 American Chemical Society.

3.3 Conclusions

In conclusion, a new one-pot interdiffusion method for FePd nanoparticles is introduced. It was found that by controlling the stabilization ligand ratios, size of Pd nanoparticle cores can be tuned from 2-7 nm, and with one equivalent Fe addition final FePd nanoparticles can be synthesized with sizes of 4-11 nm. Even more interesting, with the addition of more Fe precursor, a Fe_2O_3 shell with thickness control is seen to form over the starting FePd nanoparticles. An optimized reaction temperature of 220 °C was determined to reduce the amount of phosphine ligand doping into the Fe phase, which reduces the magnetic properties. By changing the Fe:Pd molar ratios during reactions followed by reductive annealing, the magnetic properties of the of exchanged-coupled $L1_0$ FePd/ α-Fe nanocomposite can be tuned. The domains merge together and remain in intimate contact, providing smooth exchanged-coupled M-H loops. An optimized $L1_0$ FePd/ α-Fe nanocomposite with an M_s of 97 emu/g and an H_c of 2.2 kOe is obtained, which shows better performance than just standard $L1_0$ FePd magnetic nanoparticles.

3.4 Materials and Methods

$Pd(acac)_2$ (99%) $Fe(CO)_5$ and Tributylphosphine (97%) were all obtained from Sigma-Aldrich and used as is. Oleylamine (70%) was received from Sigma-Aldrich and 1-Octadecene (90%) was received from Acros and both had argon bubbled through them for 10 min before use.

Synthesis of FePd and FePd/Fe_2O_3 core/shell nanoparticles starts with the palladium core creation. 0.25 mmol of $Pd(acac)_2$ is loaded into a 50 mL three-neck flask

and a vacuum/argon purge is done three times. 5 mL of ODE and 5 mL of oleylamine is added to the flask. The proper molar amount of TBP is added to the flask at this time if necessary. The flask is then heated to 140 °C and allowed to react for 30 min at this temperature. The solution within the flask goes through a yellow to orange color as it is heating, and turns black once the reduction of the palladium occurs. Depending on desired final particles, the proper molar amounts of $Fe(CO)_5$ is then injected (making sure the back vent is open to release CO gas) and then the temperature of the solution is raised to the desired reaction temperature (220 °C for optimized particles) and allowed to react for 1 hour. After this hour, the reaction is cooled by removal of the heating element and allowed to cool to room temperature. The reaction is then cleaned up by centrifugation in a toluene/acetone/methanol rinse three times. The best volumes for this rinse were found to be 10 mL toluene/ 30 mL acetone/ 5 mL methanol. Particles can be left in solid form or re-dispersed in toluene depending on characterization needs.

To reductively anneal the nanocomposites to form the desired $L1_0$ FePd/ α-Fe structures, the particles are crashed out of solution (if in solution) and dried with argon gas. These vials are then put into a tube furnace and put under a 10%/90% H_2/N_2 atmosphere by vacuum and purging three times. The particles then are annealed at 500 °C for 5 hours with a 1-hour ramp time to temperature, while slowly bubbling the H_2/N_2 gas through the tube. Final composites are then cooled to room temperature and rapidly moved to a drybox where they were used for characterization.

Room temperature X-ray powder patterns were obtained using monochromated Cu-Ka radiation (l 1⁄4 1.54178 A) on a Bruker proteum diffraction system equipped with Helios multilayer optics, an APEX II CCD detector and a Bruker MicroStar microfocus

rotating anode X-ray source operating at 45 kV and 60 mA. The powders were mixed with a small amount of Paratone N oil to form a paste that was then placed in a small (<0.5 mm) nylon cryoloop and mounted on a goniometer head. Transmission electron microscope (TEM) images were obtained using a Field emission FEI Tecnai F20 XT. The magnetic hysteresis (M-H) loops were taken on a Microsense EZ7 vibrating sample magnetometer. A MTI GSL-1100X tube furnace was used for reductive sintering.

4 Metal Redox: New Methodology for Nanoalloy Creation

4.1 Introduction

4.1.1 Motivation

Much of the motivation for this work stems directly from Chapter 3, but also addresses other known issues within nanoparticle synthesis literature. As shown above, there is an issue with the phosphine stabilizing ligand doping into the final metal phases. This is detrimental to the final magnetic properties of the nanocomposites. Other researchers have expressed similar problems with different ligands still present on final nanoparticles. In magnetic nanoparticles, in addition to ligand doping problems, any residual ligands included during annealing convert to a carbonaceous matrix, which adds mass to the final composites, lowering the overall performance with this non-magnetic inclusion.[102] These ligand issues are not just limited to magnetic nanoparticles. In nanocatalyst work, these ligands are coordinating to active sites, which reduces the activity as each ligand must come off the surface before the catalyst can work on the substrate. In more extreme cases, it can even shut down the activity completely. Li et al. published work on removing surfactant (oleylamine) from colloidal Pt nanoparticles and its effect on final catalytic performance.[103] They tried various treatments such as acetic acid washing, Uv-ozone treatment, but they found simple heating to 185 °C in air helped catalytic performance the most. While this method works with Pt particles, heat treatment in air is not feasible for easily oxidized metals such as Fe, Co, Ni or Mn or any metallic alloy including these elements. Ligands are not the only problem researchers run into during nanoparticle synthesis and their use in practical applications. While it's been

shown that citrate works well for reduction of easily reduced metals (Au), the harder to reduce metals require harsher reducing agents such as hydrazine, sodium borohydride or lithium borohydride. These chemicals make the synthesis of nanoparticles more complex and potentially dangerous at high temperatures. When considering bimetallic alloy systems, different reduction rates of the two metals causes issues in proper alloying of the systems. It would prove beneficial to develop a versatile solution processing methodology of nanoalloy generation without the use of either ligands or excess reducing agents.

This leaves the question of how to reduce the metal salts that are used for metal precursors in almost all nanoparticle synthesis. For this, motivation was taken from what is deemed the "Transmetalation Process" for creation of core/shell metal nanoparticles. Cheon's group first developed this method in 2001 where they utilized pre-synthesized metal nanoparticles (in this case, Co), and then added platinum hexafluoroacetylacetone ($Pt(hfac)_2$).[104] The zero-valent cobalt nanoparticles exhibit inherent reducing power, which reduces the $Pt(hfac)_2$. This platinum is said to replace the surface of the Co nanoparticles that generates a Co/Pt core/shell final structure.[104] In a subsequent report they show the versatility of this synthetic strategy by creating various core-shell particles such as Co/Au, Co/Pd, Co/Cu.[105] Other groups started showing that this method could be used with other cores besides Co such as Ni and Cu.[106, 107] With the redox chemistry proven to work with already formed particles, can the same redox power be used to create bimetallic nanoalloys from molecular precursors without the addition of either ligands or extra reducing agents?

4.2 Metal Redox for Generation of Nanoalloys.

4.2.1 Metal Redox Synthetic Strategy

As mentioned above, it is desirable to develop a synthetic strategy for nanoalloys, which removes both extra reducing agents and ligands. As known from general chemistry, zero-valent metals have their own inherent reducing ability, but zero-valent metals in molecular states have never been used to create nanoalloys thus far. Utilizing both the hot-injection method and the inherent reducing power of zero-valent molecular precursors, it could be possible to create bimetallic and even trimetallic nanoalloy systems. To test this strategy, only three different reagents are required: a high boiling point solvent, a zero-valent molecular precursor and a metal salt. Examples of zero-valent molecular metal precursors are metal carbonyls and metal cyclooctadienes such as $Fe(CO)_5$, $Co_2(CO)_8$, $Mn_2(CO)_{10}$ and $Ni(cod)_2$. In the case of metal salts, mostly metal acetylacetonates are utilized in this study. Figure 44 displays a general scheme of

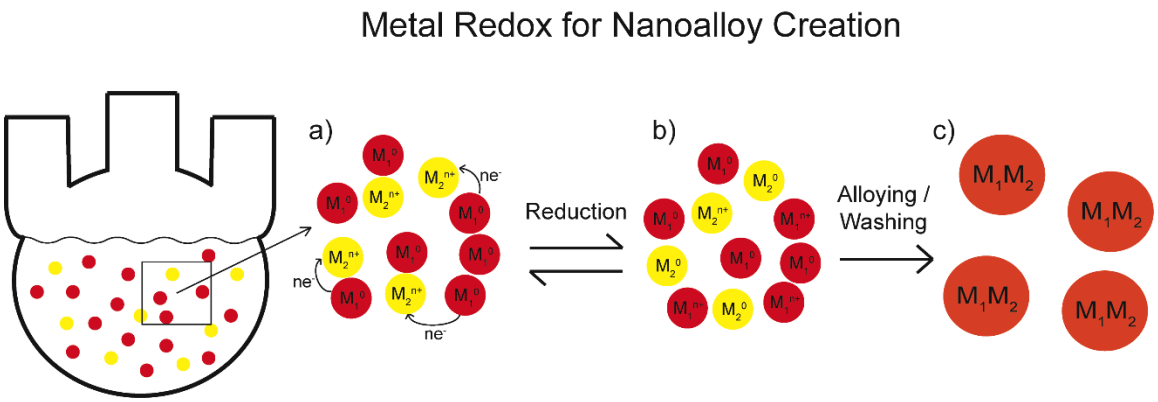

Figure 44. Scheme of the metal redox strategy. Reprinted with permissions from [108].

the metal redox synthesis. Upon injection there are two precursors, one M_1^0 (red spheres) from the decomposition of the zero-valent precursor and a M_2^{n+} (yellow spheres) from the metal salt. Reduction of the metal salt occurs immediately, however it is important to note that this reaction is in equilibrium, which means the entire zero-valent metal

precursor does not get used up in the reduction. This leftover zero-valent precursor and the now reduced metal salt alloy together producing the final bimetallic nanoalloys. However, there are stipulations on the choice of the metal precursors, as the zero-valent metal must have enough reducing power to reduce the metal salt. This can be simply determined by setting up a generic set of half-cell reactions such as:

$2M_1^0 \rightleftharpoons M_1^{n+} + M_1^0 + ne^-$ $E^o = x$ (Eq. 12)

$M_2^{n+} + ne^- \rightleftharpoons M_2^0$ $E^o = y$ (Eq. 13)

$2M_1^0 + M_2^{n+} \rightleftharpoons M_1M_2 + M_1^{n+}$ if $E_{cell} = (x+y) > 0$ reaction will proceed. (Eq. 14)

For example the FeNi system is used. The half-reaction E^o values for Fe^0 and Ni^{2+} are +0.44V and -0.25V, respectively. E_{cell} for this system is then +0.19 V, which is greater than zero meaning this reaction is spontaneous. It is important to note that these values are all at standard conditions, but for every reaction tested if the E_{cell} produced >0 values, the reaction occurred. This allows the half-reaction equations to be a simple guide for the metal redox precursor selections. Fe^0 can thereby be used as a zero-valent precursor to reduce any metal cation with a reduction potential greater than -0.44 V, which means Co^{2+} (E^o = -0.21 V) Pt^{2+} (E^o = 1.188) and Pd^{2+} (E^o = 0.915 V) are all valid choices and will produce its corresponding bimetallic alloy. With these rules to determine if the reaction will be spontaneous, Figure 45 shows TEM images of a vast sampling of the bimetallic alloys achievable by this synthetic strategy with elemental mapping of

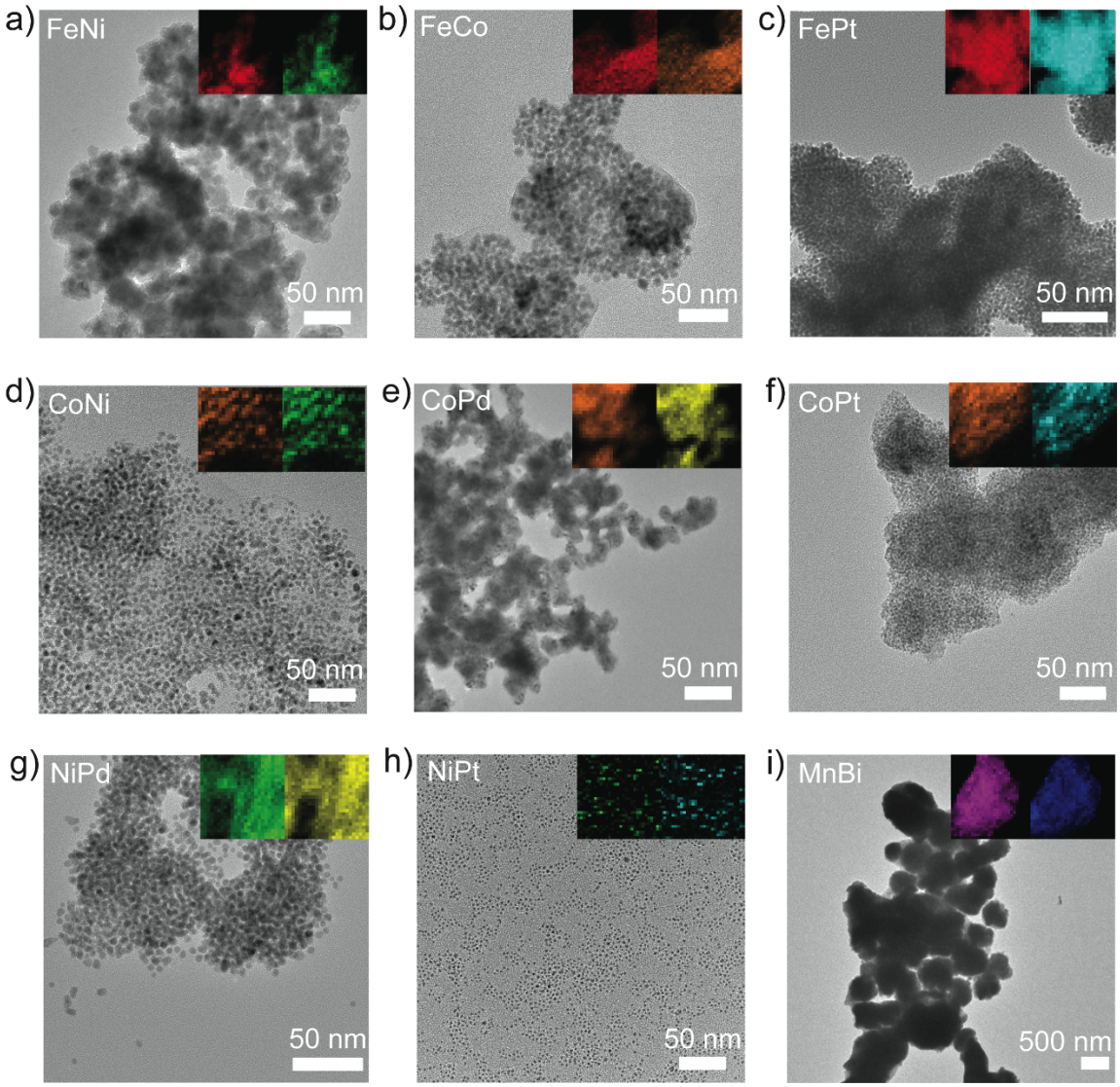

Figure 45. Nanoalloys created by utilizing a-c) $Fe(CO)_5$ as the zero-valent precursor, d-f) $Co_2(CO)_8$ as the zero-valent precursor, g,h) $Ni(cod)_2$ as the zero-valent precursor and i) $Mn_2(CO)_{10}$ as the zero valent precursor. All metal salts were acetylacetonates except the Bi^{3+} where bismuth neodecanoate was used. Reprinted with permissions from [108].

each corresponding element in the inset. To confirm proper alloying XRD of the post-annealed samples are shown in Figure 46. This data shows that the proper phases are generated. Note that an annealing process is required to increase the crystallinity of the

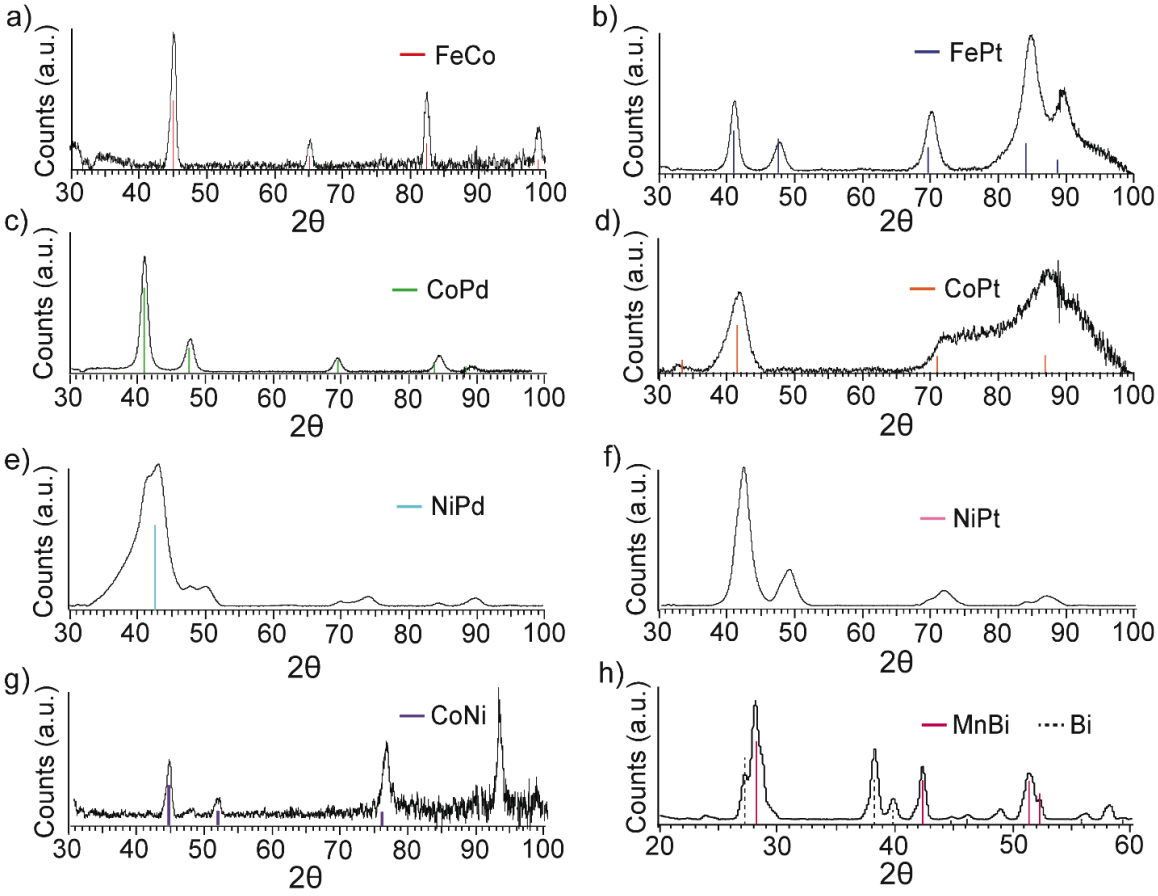

Figure 46. a) Diffraction pattern of FeCo nanoalloy (Red line, FeCo JCPDS# 00-049-1568). b) Diffraction pattern of FePt nanoalloy (Blue line, JCPDS# 00-029-0718). c) Diffraction pattern of CoPd (Green line, JCPDS#00-050-1437). d) Diffraction pattern of CoPt (Orange line, JCPDS#00-043-1358). e) Diffraction pattern of NiPd (No available JCPDS for NiPd, blue line obtained from[109]) f) Diffraction pattern for NiPt (No JCPDS for NiPt). g) Diffraction pattern of CoNi (No JCPDS for CoNi, purple lines obtained from[110]). h) Diffraction pattern of MnBi (Black Dotted lines Bi JCPDS#00-044-1248). Reprinted with permissions from [108].

nanoalloys to get proper diffraction. In the case of the MnBi. This is typical even in bulk synthesis where the MnBi phase must be separated from the Bi phase.[94] M-H loops of the

annealed particle were also obtained to help confirm proper magnetic phase formation and are shown in Figure 47. All of the alloy systems except MnBi are soft magnets.

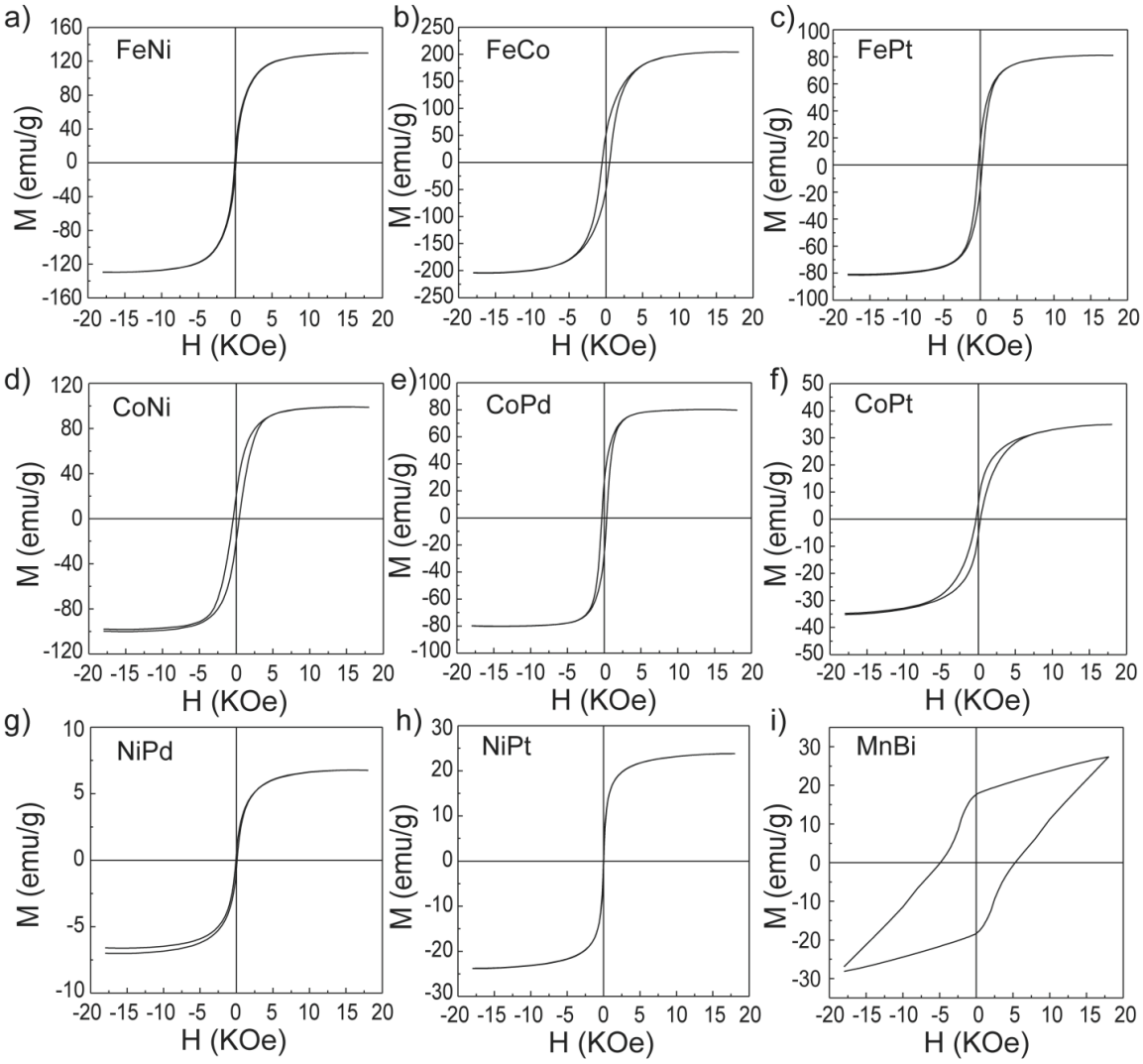

Figure 47. Corresponding M-H loops of the different bi-metallic alloy systems created in Figure 44. Reprinted with permissions from [108].

MnBi shows a kinked M-H loop, indicting decoupling of the magnetic domains. The large amount of nonmagnetic bismuth phase in the alloys is most likely the cause. FePt does have a $L1_0$ phase, which generates coercivity but the generated alloy exhibits s a

$Fe_{69}Pt_{31}$ stoichiometry, making it a soft magnetic phase.[95] All the stoichiometry's of the particles displayed in Figure 45 are listed in Table 1 below. All reactions use a 2:1 zero-valent precursor:metal salt molar ratio with a reaction temperature of 300 °C. It is observed that the stoichiometry of the particles is nearly the same as the loading ratios at this temperature. It would be ideal if further control of the final stoichiometry of the particles could be achieved.

Metal Alloy	Stoichiometry Used	Stoichiometry Measured (EDS)
FeCo	2:1	$Fe_{63}Co_{37}$
FePt	2:1	$Fe_{69}Pt_{31}$
CoNi	2:1	$Co_{66}Ni_{34}$
CoPd	2:1	$Co_{66}Pd_{34}$
CoPt	2:1	$Co_{79}Pt_{21}$
NiPd	2:1	$Ni_{62}Pd_{37}$
NiPt	2:1	$Ni_{84}Pt_{15}$

Table 1. Stoichiometry of final nanoalloys created in Figure 44. Determined by EDS measurements.

4.2.2 Stoichiometry Control of the Metal Redox Method

In order for this methodology to be worthwhile, the final stoichiometry of the nanoalloys must be controllable. To demonstrate control of stoichiometry, the FeNi is chosen as an example system. As stated before, these metal redox reactions are in equilibrium, therefore both loading concentrations and reaction temperatures can be utilized to tune the final stoichiometry of the nanoalloys. To show the effects of both of these variables, reactions with a 1:1 and 1:2 Ni:Fe molar ratios were conducted at

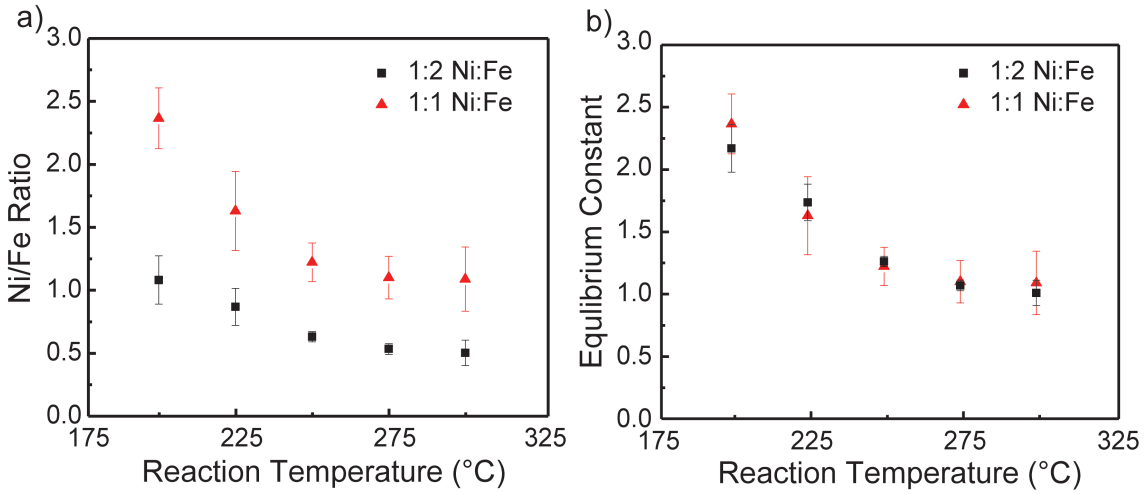

Figure 48. a) Ni/Fe ratios determined by EDS for different temperatures of both 1:2 and 1:1 Ni:Fe reactions. b) Equilibrium constant (K) determined for all of the different reaction temperatures and ratios. Reprinted with permissions from [108].

different temperatures. Figure 48 shows the Ni/Fe ratios of the final particles at different temperatures. All ratios in this figure are generated by simply dividing the Ni atomic amount by the Fe atomic amount that were determined by EDS. All particles generated showed higher nickel content at lower reaction temperatures. This observation can be explained by considering the simplified chemical equilibrium in the system:

$$Fe^0 + Ni(acac)_2 \rightleftharpoons Ni^0 + Fe(acac)_2 \qquad \text{(Eq. 15)}$$

As stated above the E_{cell} of the reaction is positive, meaning it is spontaneous but it is not driven to the product side. At lower temperatures, the spontaneous reaction is favored, but as the thermal energy is increased the equilibrium is pushed backwards as now the non-spontaneous reaction is becoming more favored. Higher Fe^0 concentration in the alloys with higher temperatures is due to this equilibrium tuning. However, it seems that there is a limit to this thermal pushing, as at 275 °C and 300 °C the relationship becomes

non-linear for both loading amounts and stagnates at precursor loading amounts. This is also observed for all the other alloys generated at these temperatures (Table 1). An equilibrium constant for this reaction at different temperatures can easily be determined by $K_{eq}=[Ni^0]/[Fe^0]$ when using the 1:1 Ni:Fe molar ratio synthesis, as it is just the Ni/Fe ratio in the particles. In the case of the 1:2 Ni:Fe reaction, the equation must be modified to account for the extra iron, as any of the unreduced Fe^0 will be included within the final particles. To do this, simply multiply the Ni/Fe ratios by the excess iron used (in this case 2). The determined equilibrium constants (K) for the different temperature reactions are shown in Figure 48b, which match nicely. Chemically, this makes sense as only temperature affects the K_{eq}.

Experiments were also carried out to help confirm the EDS measurements for the 1:2 Ni:Fe synthesis. Both Inductively Coupled Plasma Atomic Emission Spectroscopy (ICP-AES) and absorbance measurements were conducted to verify the EDS measurements, shown in Figure 49. ICP-AES calibration curves and determined Ni/Fe ratios for the 1:2 Ni:Fe synthesis are seen in Figure 49a,b respectively, which match nicely to the EDS determined Ni/Fe ratios. It is also possible to use UV-Vis absorption techniques to determine the stoichiometry of the particles. Since $Fe(acac)_2$ is produced as a byproduct in the synthesis, the concentration of $Fe(acac)_2$ in the supernatant after cleaning of the particles can be determined. This concentration is the amount of Ni that was reduced, assuming that the only thing that Fe^0 reduced was the Ni. Knowing the initial amount of Fe^0 used, the final equilibrium constant for the different reaction temperatures can be calculated. Figure 49c displays the spectra of neat $Fe(acac)_2$ compared to the supernatant of the particles, confirming $Fe(acac)_2$ generation. The inset

is the calibration curve used to determine the $Fe(acac)_2$ concentration in the supernatant. Figure 49d compares the values of the K_{eq} determined by the three methods showing good agreement between EDS and ICP-AES. Absorbance measurements matches well until the 300 °C point, where there could be decomposition of the $Fe(acac)_2$ during the reaction. In any case, these studies confirm that EDS is an acceptable method to determine the stoichiometry for all of the particles.

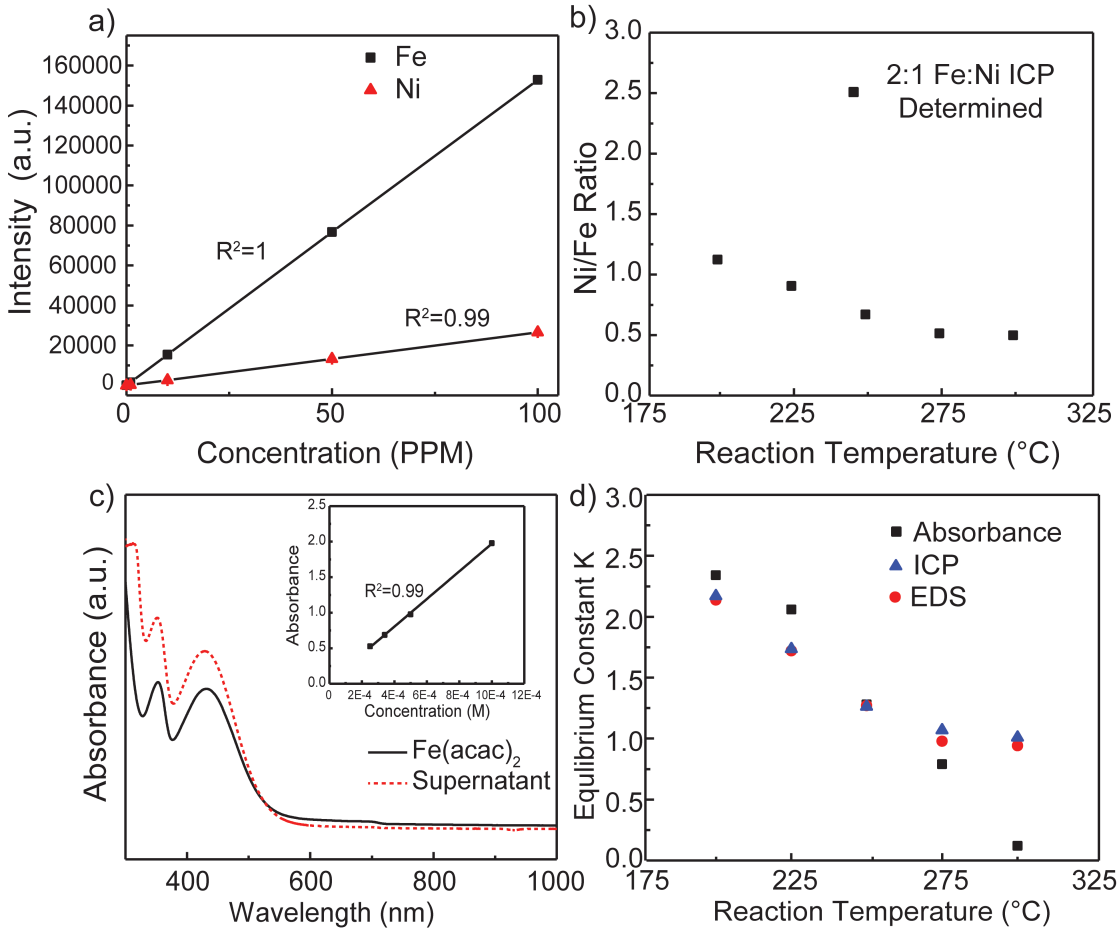

Figure 49. a) ICP-AES calibration curve for the determination of Ni/Fe ratios. b) Ni/Fe ratios determined by ICP-AES. c) Absorbance spectrum of neat $Fe(acac)_2$ compared to the supernatant solution after cleaning of particles. Inset is calibration curve used to

determine $Fe(acac)_2$ concentration in supernatant. d) K_{eq} values determined for all three methods. Reprinted with permissions from [108].

Now that the K_{eq} values of the reactions are known for the different temperatures, a Van't Hoff plot can be made by graphing Ln(K) versus (1/T) and fitting a straight line which relates to the equation:

$$\ln K = -\left(\frac{\Delta H}{R}\right)\left(\frac{1}{T}\right) + \left(\frac{\Delta S}{R}\right) \quad \text{(Eq. 16)}$$

where ΔH and ΔS are the enthalpy and entropy change, R is the gas constant and T is the reaction temperature in K. This plot is shown in Figure 50 with the equation of the fitted straight line displayed. ΔH of the reaction can then be found, which produces a value of -19.9 kJ/mol for the FeNi formation. More importantly, this equation allows for the determination of K_{eq} at any temperature, which is directly related to the stoichiometry of the final particles. This type of study can be easily carried out for the other nanoalloy systems, as they are all controlled by a fundamental equilibrium constant. Using this and precursor loading amounts, the final stoichiometry in the nanoalloys can be controlled using the metal redox method.

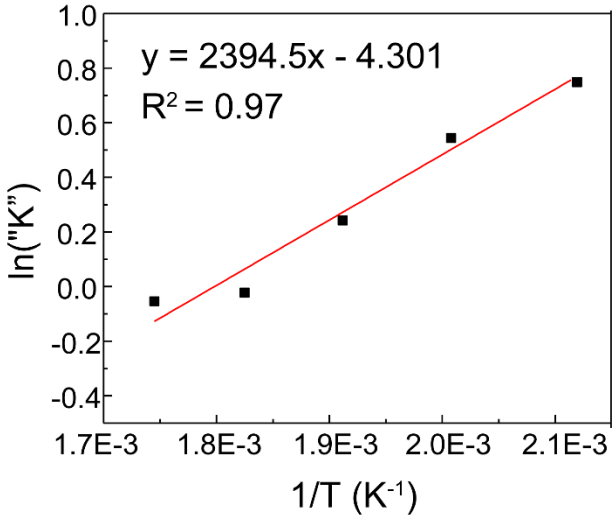

Figure 50. Van't Hoff plot of the FeNi system. Reprinted with permissions from [108].

4.2.3 Trimetallic Nanoalloys Generated by Metal Redox and their Magnetic and Catalytic Properties

The creation of trimetallic alloys is also achieved with the metal redox method, as long as the zero-valent precursor has enough reducing power to reduce both of the other metals. To demonstrate this, a trimetallic alloy of FeNiPd was generated and its properties characterized. FeNiPd was generated at 300 °C to keep the equilibrium constant around ~1 as shown above, meaning stoichiometry of loaded precursor molar ratios are close to that of the final nanoalloyed particles. To study the differences in properties, the molar ratios were changed from pure FePd to FeNi, with the molar ratios being 2:x:y for Fe:Ni:Pd (x+y=1). To show the effects of the different stoichiometry on the phases, XRD was employed, shown in Figure 51a. Starting from pure FePd, the peaks match with FePd diffraction with some α-Fe diffraction visible due to the thermodynamic stability in the phase diagram, mentioned above. As more Ni is incorporated into the synthesis, a visible peak shift from the FePd to the FeNi phase is easily discerned. It is interesting to note that the α-Fe is present in all of the different alloys until pure FeNi,

where the phase diagram does not exhibit the thermodynamic stability for α-Fe formation. Figure 51b displays a typical TEM image of the $Fe_2Pd_{0.5}Ni_{0.5}$ nanoalloy created with elemental mapping of the particles showing all three elements well distributed throughout. The magnetic properties of the different ratio alloys were also examined and the M_s and H_c of each system are displayed in Figure 51c. At pure FePd, H_c is highest due to $L1_0$ FePd formation during annealing. As nickel concentration increased within the particles the Hc rapidly decreases, and stagnates at ~ 0.2 nickel stoichiometry. This drop in H_c is due to the disruption in $L1_0$ formation, where the critical nickel-loading amount matches theoretical calculations of the FePdNi phase diagram.[111] As the nickel loading increases, the M_s also increases, due to FeNi being a soft magnetic phase with higher M_s. This shows that trimetallic alloy systems can be easily achieved with the metal redox method and their magnetic properties can be simply controlled.

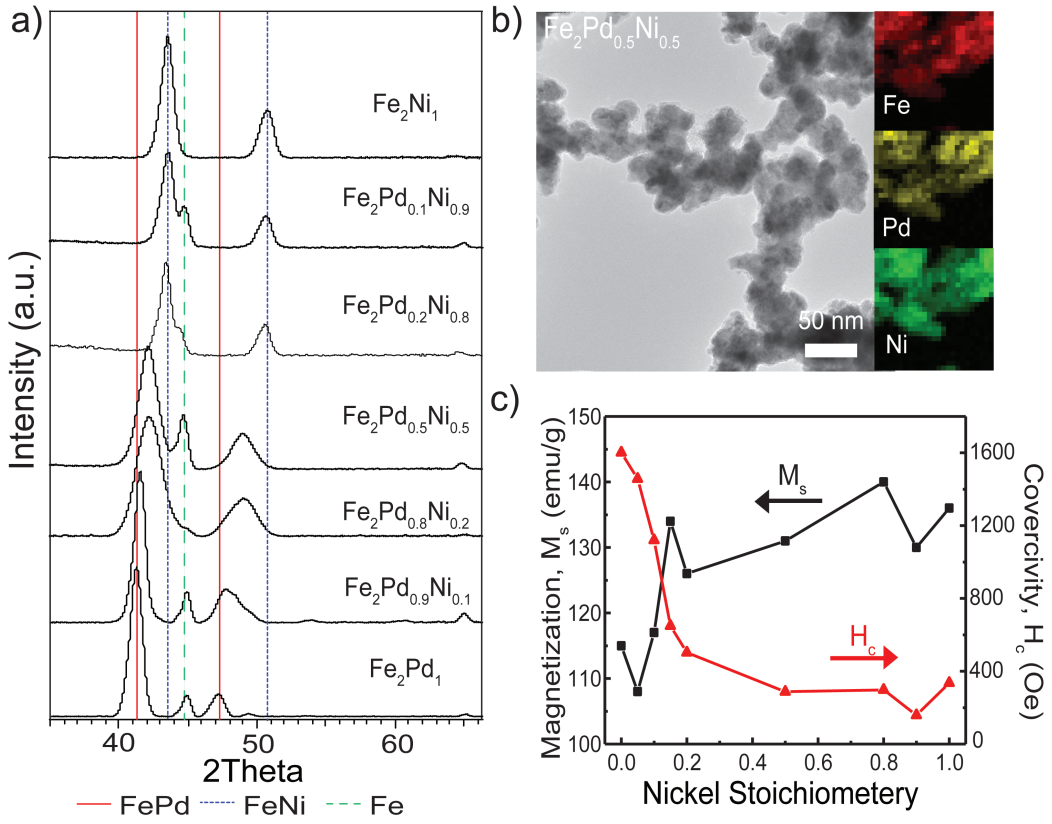

Figure 51. a) XRD spectra with varying FePdNi ratios. b) TEM image of the $Fe_2Pd_{0.5}Ni_{0.5}$ nanoalloys with elemental mapping. c) Graph of M_s and H_c of the FePdNi alloys dependent on nickel stoichiometry. Reprinted with permissions from [108].

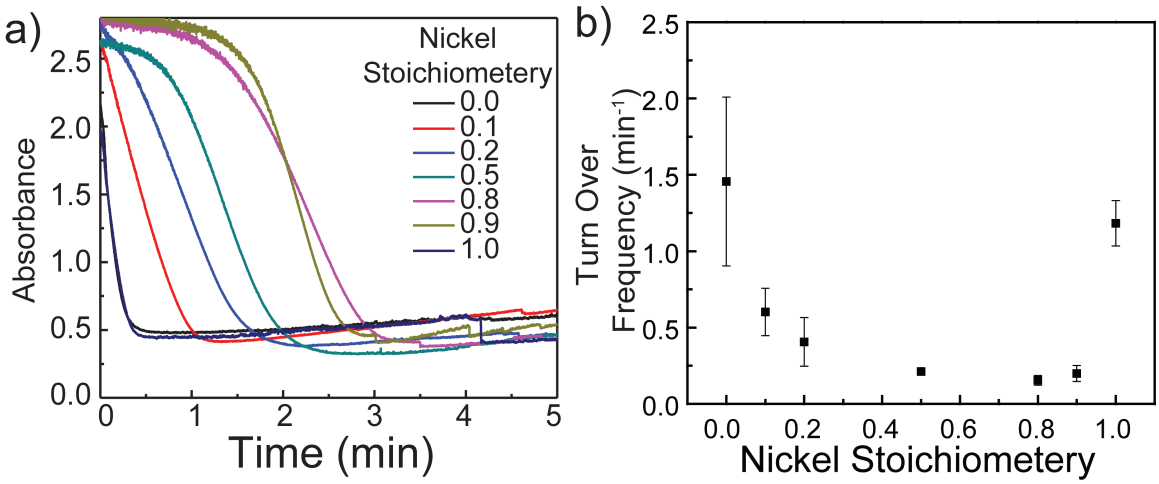

Figure 52. a) UV-Absorbance time dependent measurements of reduction of p-nitrophenol with different FePdNi trimetallic alloys. b) Turn over frequency for each of the different stoichiometric trimetallic FeNiPd. Reprinted with permissions from [108].

These trimetallic alloys also provide an interesting opportunity to study the effects of the varying stoichiometry on the nanoalloy's catalytic activity. As an example, the reduction of p-nitrophenol to p–aminophenol reaction will be examined. This reaction is done in high excess of sodium borohydride, which allows for the assumption that the rate of reaction is independent of the reducing agent concentration. Others have used this reaction as a standard catalytic reaction for many different metal nanoparticles, making it a reasonable starting point for our novel ligandless nanoalloys.[112-114] P-nitrophenol creates a yellow solution when dissolved in water with an absorption max at 400 nm. It then turns colorless as it is converted to p-aminophenol. Figure 52a shows a plot of the absorbance of p-nitrophenol taken at 400 nm to examine the reduction reaction occurring over a five-minute period. The turn over frequency (TOF) can be calculated for these different stoichiometric nanoalloys, which is displayed in Figure 52. TOF is calculated by

taking number of moles of product produced (or number of moles of starting p-nitrophenol and assume complete conversion), and dividing that number by the number of moles of catalyst used. This is then divided by time required to complete the conversion. TOF can then be used to compare the differences between the nanoalloy catalysts' activity. It can be seen that for pure FePd, the TOF is the highest, and rapidly decreases with nickel stoichiometry doping. The TOF stays low until the pure FeNi phase is generated. The low performance of the trimetallic systems can be related to the α-Fe phase that is present in the particles. α-Fe is a relatively inert catalyst for hydrogenation when comparing to other transition metals, lowering the TOF of these alloys. Once the α-Fe phase is no longer present, as in the binary FeNi alloys, the TOF number rises. In the case of the FePd nanoalloys, Pd is a better catalytic material, which gives it the highest TOF, even though there is still α-Fe phase present. Since these particles are magnetic,

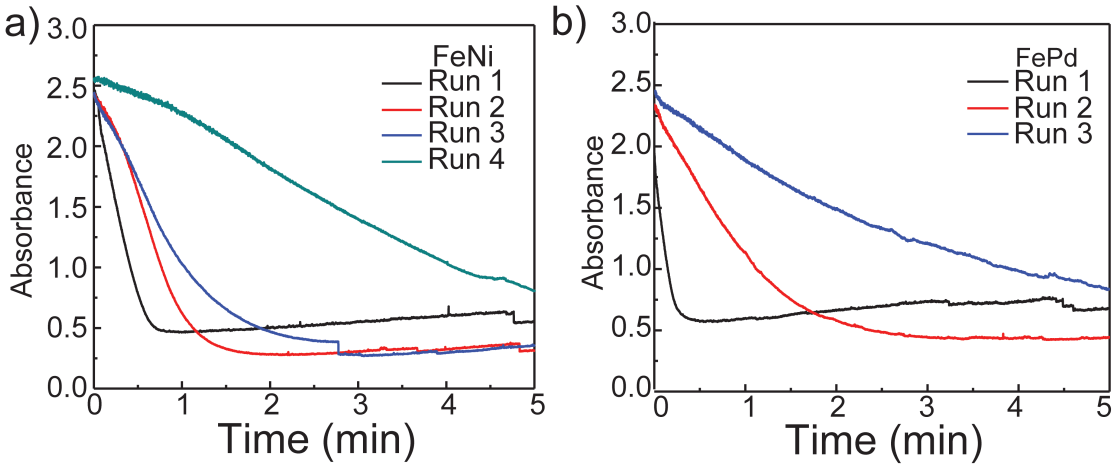

Figure 53. Uv-Vis time dependent measurements demonstrating recyclability of the binary nanoalloys a) FeNi and b) FePd. Reprinted with permissions from [108].

they can be quickly and easily separated by a strong magnet and then reused in the catalytic reaction as shown in Figure 53 with both of the binary nanoalloys. Data

presented here shows initial promise for making use of the metal redox method to produce many different ligandless bi- and tri-metallic alloys for catalytic uses.

4.3 Expansion of the Metal Redox Strategy: The Case of FeGa

4.3.1 Nanoalloy Creation with Similar Redox Potentials

Now that the metal redox method has been shown to be a versatile new strategy of generating ligandless nanoalloys without excess reducing agents, expansion on the obtainable types of alloys is desired. As seen above, thermal energy was utilized to push a spontaneous reaction (E_{cell} is positive) backwards. The next question is if it is possible to use this thermal energy to push a non-spontaneous (where E_{cell} is close to zero or negative) reaction to the products. The alloy system of FeGa is an ideal bimetallic system to test this hypothesis, because the reduction potentials of each of the metals are close to each other (Fe^0 = 0.44 V, Ga^{3+} = -0.53 V). Sample reactions following standard metal redox synthetic procedures and using 2:1 Fe:Ga molar ratios with $Fe(CO)_5$ as the zero-valent precursor and $Ga(acac)_3$ as the metal salt were attempted. Figure 54a-c displays TEM images of the FeGa particles produced at different reaction temperatures with elemental mapping shown on the right. First thing that is apparent is that the reaction does not occur unless a temperature of 275 °C or greater is used. This limits the reactions to a window of 275-320 °C due to the boiling point of the solvent used. In any case, the trend of increasing gallium content with higher reaction temperatures seen in the EDS data with stoichiometry of $Fe_{80}Ga_{20}$, $Fe_{74}Ga_{26}$, and $Fe_{60}Ga_{40}$ with temperatures of 275, 300, and 320 °C respectively. This suggests thermal energy can be used to expand the metal redox method to alloy systems with closer redox potentials. Similar to the FeNi, a

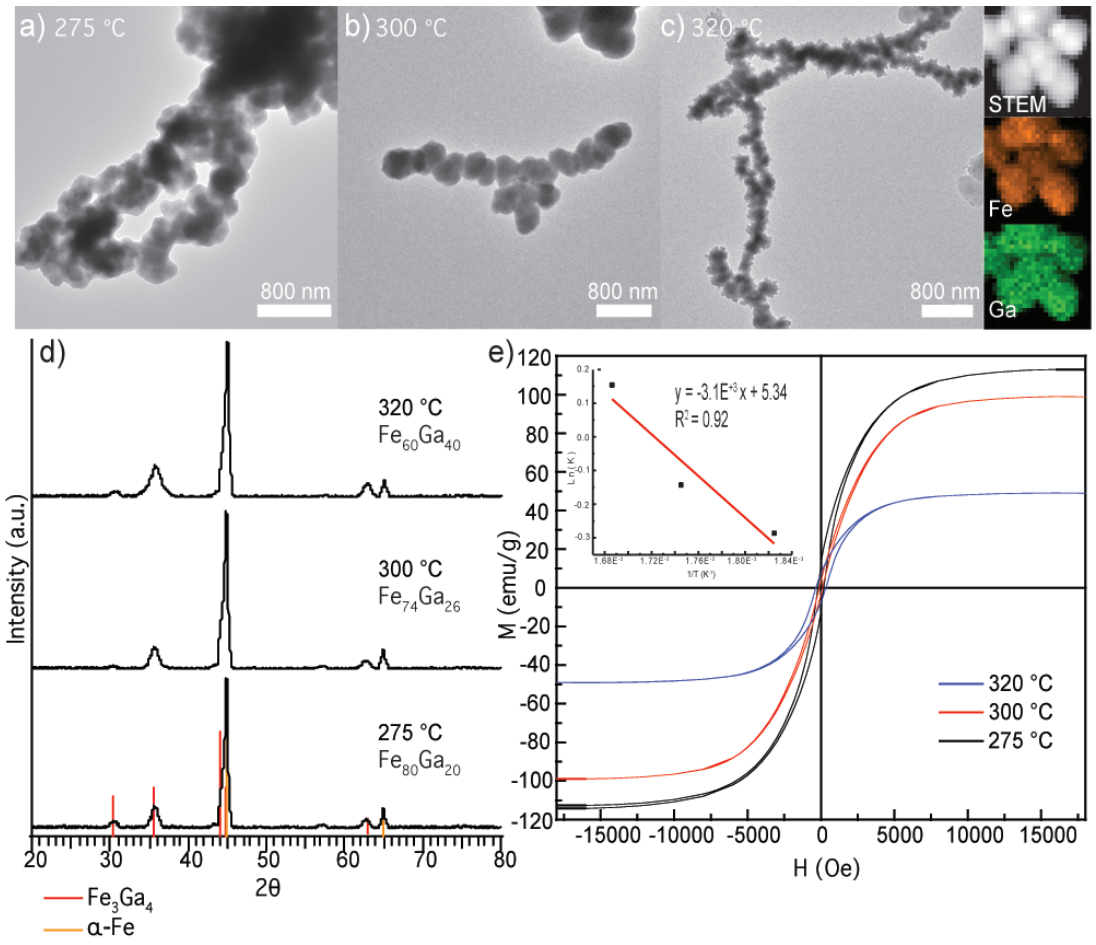

Figure 54. a-c) TEM images of FeGa nanoalloys with different reaction temperatures. d) XRD of annealed FeGa nanoalloys produced with different reaction temperatures. e) M-H loops of annealed FeGa alloys. Inset is Van't Hoff plot for the FeGa reaction.

Van’t Hoff plot can be generated and a straight line can be fit producing the equation y= -3.1x10^{+3}x + 5.3 (inset of Figure 54c). As shown above, this equation can then be used to determine final stoichiometry in the particles within this limited reaction window range. To confirm that increasing amounts of gallium are incorporated into the particles, XRD and M-H loops were acquired of the annealed samples. Annealing was required, as the particles out-of-pot were completely amorphous. Figure 54d displays XRD spectra of the

different FeGa nanoalloys at different reaction temperatures. Two phases are seen to form after annealing, one being a Fe rich α-Fe phase and a Ga rich Fe_3Ga_4 phase. This is not unexpected, as Ga is soluble in α-Fe up to ~25%, which accounts for the large α-Fe

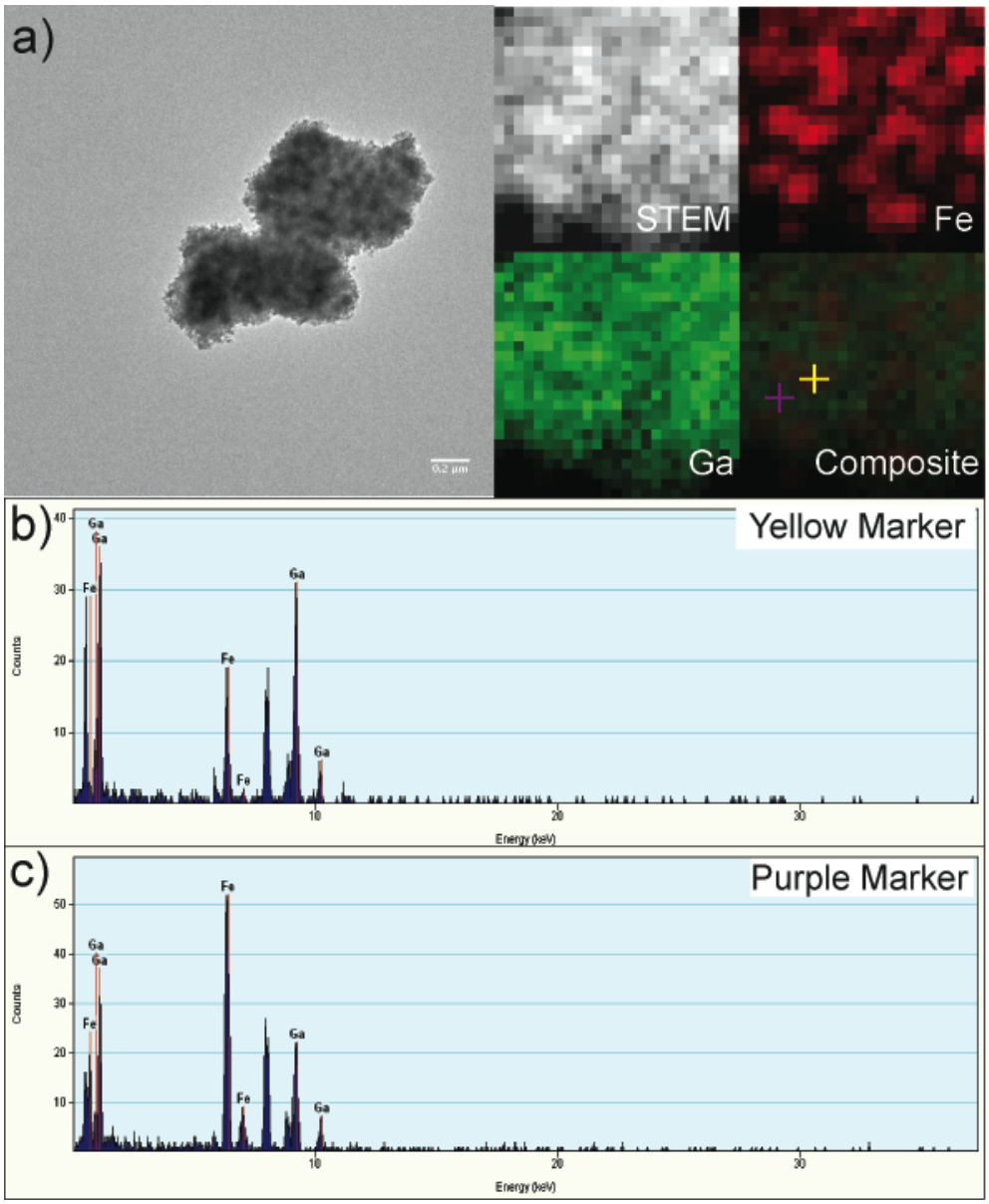

Figure 55. a) Annealed FeGa nanoalloys with elemental mapping displayed on right. b,c) EDS spectra obtained at b) yellow marker and c) purple marker in composite image.

peaks. The rest of the Fe is then incorporated into the other Fe_3Ga_4 phase, which is more intense at higher reaction temperatures. TEM, elemental mapping, and EDS confirm the different phase formations shown in Figure 55. Figure 55a shows TEM image of the annealed FeGa nanoalloys at 550 °C for 12 hours. Elemental mapping shown to the right reveal that there is indeed phase separation after annealing, with spherical Fe rich phases with Ga distributed throughout. Examining the EDS spectrum at a Fe rich point (purple marker) displays high Fe counts, and when examining a point off the Fe rich sections, a Ga rich section is observed in the EDS spectrum (yellow marker). The M-H loops of the annealed particles, presented in Figure 54c, show a correlation between a drop in M_s and a decrease in the α-Fe soft magnetic phase. These experiments confirm that the metal redox can be used to produce nanoalloy with metals that have close redox potentials, and their properties can be easily tuned by temperature.

4.3.2 Effect of Ligand with Reducing Power in FeGa Nanoalloy Creation.

From the above experiments it has been confirmed that FeGa nanoalloy can be generated with the metal redox method. However, there is a limitation in stoichiometry obtainable due to the upper bound of thermal energy. The limit is due to the boiling point of the solvent. To overcome this limitation, a ligand (oleylamine), which exhibits limited reducing power was examined to help push more Ga into the nanoalloys. It is important to note that oleylamine does not possess the reducing power necessary to reduce $Ga(acac)_3$ at 320 °C, confirmed by a control experiment. Therefore, experiments utilizing different oleylamine molar quantities (in comparison to total metal moles in the system) were carried out at a reaction temperature of 300 °C. Figure 56a-c shows typical TEM images of the FeGa nanoalloys with different molar quantities of oleylamine included

with elemental mapping below. At low oleylamine amounts (0.50x) nanoalloys are formed and show even distribution between the elements. There is also an increase of gallium incorporation within the nanoalloys, producing $Fe_{62}Ga_{38}$ stoichiometry, when compared to the $Fe_{74}Ga_{26}$ produced without oleylamine. When more oleylamine is added

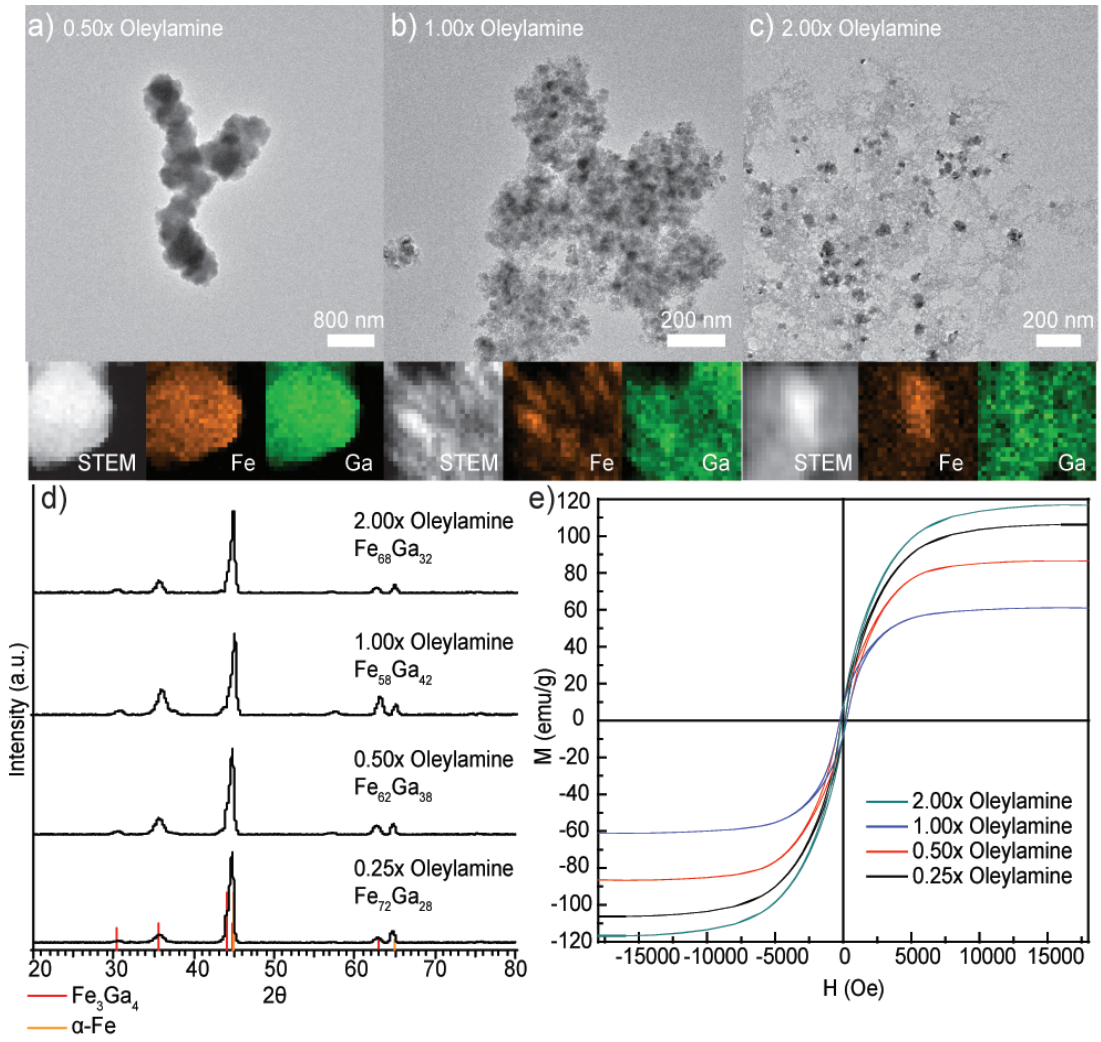

Figure 56. a-c) TEM images of FeGa nanoalloys generated with oleylamine concentrations of a) 0.5x, b) 1.0x and c) 2.0x. d) XRD of annealed FeGa nanoalloys dependent on oleylamine concentration. e) M-H loops of annealed FeGa nanoalloys dependent on oleylamine concentration.

(1.0x) even more gallium is included producing $Fe_{58}Ga_{42}$ nanoalloys. If more reducing ligand is added (2.0x), a deviation in this trend occurs. From the TEM image in Figure 56c it is seen that the nanoalloys have phase segregated, with large dark particles forming. Elemental mapping confirms that these are Fe rich particles. Formation of these particles can be explained, as it is known that oleylamine can reduce $Fe^{2+/3+}$ ions. This indicates that after the Fe^0 reduces the $Ga(acac)_3$ it can then be reduced back to Fe^0 by the oleylamine, forming these large Fe particles. EDS confirms that these nanoalloys are richer in Fe ($Fe_{68}Ga_{32}$), due to this back reduction. XRD of the annealed samples show the same phase separation with α-Fe and Fe_3Ga_4, with intensity peaks of each corresponding to the trend observed in EDS. M-H loops of the annealed FeGa nanoalloys further verify the phase separation and back reduction of Fe, as the M_s drops as more Ga is included in the alloys, then increases when the back reduction of iron occurs. As such, it is seen that oleylamine can be used to help co-reduce Ga, helping control final stoichiometry of the nanoalloys produced. However, if excess oleylamine is used, back reduction of the Fe ions occurs, which must be taken into consideration when utilizing this methodology.

4.3.3 Size Control of FeGa Nanoalloys Utilizing Metal Redox and Stabilizing Ligands.

Finally, it would prove extremely beneficial to achieve size control of the nanoalloys produced by the metal redox methodology for applications where size control is necessary, like self-assembly and other size dependent attributes (plasmons, single domain particles). In this study, Trioctylphosphine oxide (TOPO) is used as a stabilizing ligand to investigate if size control can be achieved. Figure 57a-c presents TEM images

with varying TOPO molar concentration (compared to total metal moles) with the standard 300 °C reaction temperature. At 0.5x TOPO concentrations, large masses are observed, however there are smaller particles starting to form. At 2.0x TOPO concentrations, the FeGa particles shrink to a diameter of 8.9 ± 1.2 nm, however slight

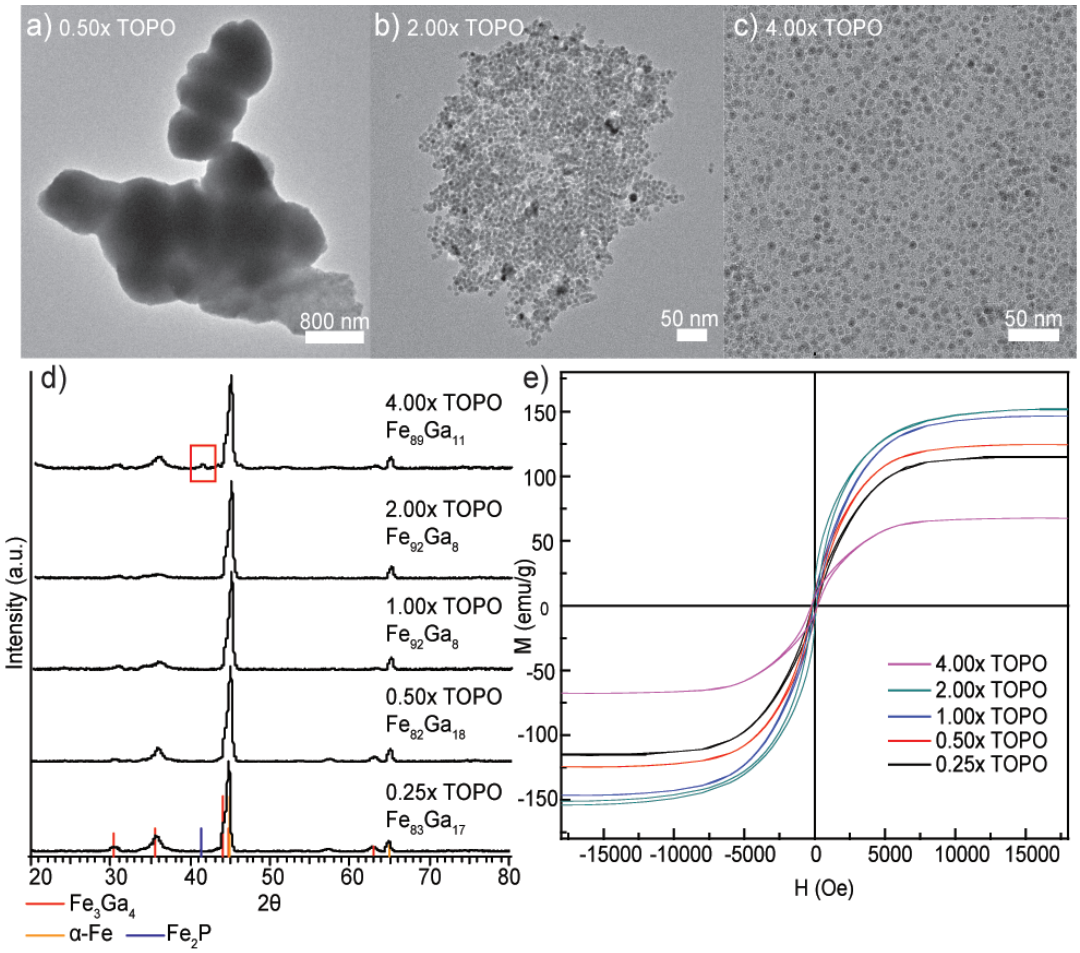

Figure 57. TEM images of FeGa nanoalloys produced with a) 0.50x TOPO, b) 2.00x TOPO, c) 4.00x TOPO. d) XRD of annealed FeGa nanoalloys with different TOPO amounts. e) M-H loops of annealed FeGa nanoalloys with different TOPO amounts.

aggregation is still present. At 4.0x TOPO, particles are completely separated and display a diameter of 6.2 ± 0.91 nm due to increase concentration of stabilizing ligand. However,

with the achievement of size control, the particles lose gallium content. Even at a loading amount of 0.5x TOPO the stoichiometry is $Fe_{82}Ga_{18}$. With the use of 2.0x the stoichiometry is reduced to $Fe_{92}Ga_8$. This decrease is most likely due to the stabilization and passivation of the Fe^0, making it less likely to reduce the $Ga(acac)_3$. XRD confirms the drop in Ga, as the Fe_3Ga_4 phase is almost non-existent and the Ga present is likely dissolved into the α-Fe structure. Once again, the M-H loops follow the trend in increased M_s with the increase of the α-Fe diffraction, except for the final 4.0x TOPO particles. The reason for the decreased M_s is due to Fe_2P formation, which is confirmed by the diffraction peak starting to arise in the XRD. This indicates that even the more stable phosphine ligand TOPO can still dope into the Fe phase. So care must be taken when picking the proper stabilizing ligand. These studies show that size control can be achieved while utilizing the metal redox strategy, albeit a loss of reduction can occur. However, if done with systems with a higher positive E_{cell} value the loss of reduction may not be as bad. Size control makes the metal redox strategy even more robust, providing control for applications that require it.

4.4 Solution Processed MnBi Nanoalloy Generation with the Metal Redox Strategy

As mentioned above in the metal redox section, I have shown it is possible to create MnBi nanoalloys with this synthetic strategy. While MnBi does not include Fe as all other systems in this dissertation, it is worth discussion as this is the first report of high quality MnBi synthesis via a solution processing method. MnBi is a hard magnetic phase that was first created by the navy with high energy melting processes in the 50's.[115, 116] It was found to possess a unique property of increasing H_c upon heating. In most other hard

magnetic materials, the H_c drops as temperature is raised due to the extra energy making it easier to flip the magnetic domains. Therefore, MnBi has been proposed as a magnetic phase that can be used in high temperature applications such as automobiles.[117-121] Generation of MnBi utilizing normal solution processing methods has been a difficult endeavor as controlling both the reduction and alloying is challenging with such different reduction potentials of the two elements (Mn^{2+} = -1.19 V and Bi^{3+} = -0.31 V). The metal redox method eliminates this problem by using Mn^0 as a reducing agent. In this section the champion particles will be presented, followed by synthetic control of this unique synthesis.

4.4.1 Champion MnBi Nanoalloys and Properties

Figure 58a presents a TEM image of a single MnBi nanoalloy particle with elemental mapping to the right. Elemental mapping shows both elements distributed throughout the particle. It should be noted that there is a high concentration of Mn on the surface of the particles, which is a result of how the formation proceeds and will be discussed later. XRD of this nanoalloy is presented in Figure 58b, showing almost complete MnBi diffraction, however there is still a very small amount of Bi phase present. The first two quadrants of an M-H loop of magnetically aligned MnBi are shown in Figure 58c showing an M_s of 49 emu/g and an H_c of 15 kOe. The observed magnetic properties make this the first solution processed MnBi nanoalloy with near bulk properties. Figure 59 shows M-H loops of example particles under different temperatures, which show that these MnBi nanoalloys also exhibit an increase of H_c during temperature

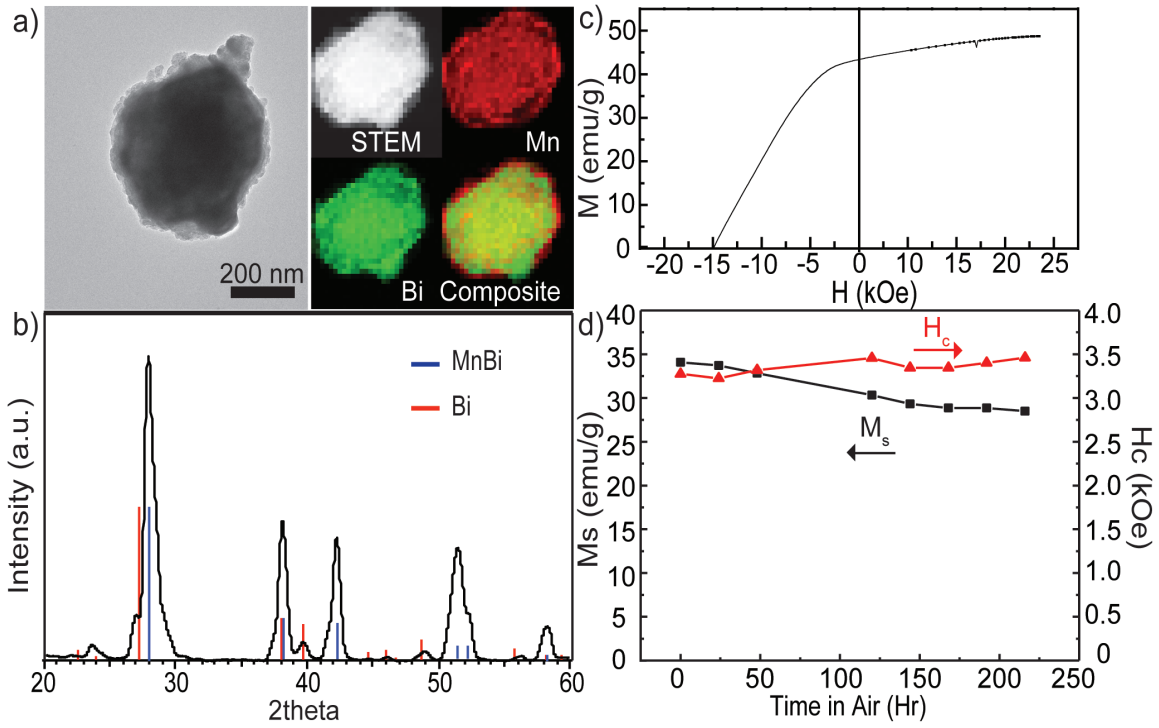

Figure 58. a) TEM images of MnBi nanoalloy. b) XRD spectra of MnBi nanoalloy. c) First two quadrants of M-H loop of aligned MnBi. d) Magnetic stability of MnBi in air.

treatment. All M-H loops from here out will show lower H_c and M_s of particles as we do not possess the means to compact and align the MnBi particles under high magnetic field in-house. Normal bulk MnBi suffers from rapid oxidation, however the MnBi nanoalloys showed high stability in air, as presented in Figure 58d. The M_s of the particles only drops lightly over multiple days, and the H_c are unaffected. This stability is attributed to the aforementioned Mn shell on the surface, protecting the internal MnBi from oxidation. Now that the MnBi champion particles and properties have been discussed, synthetic control of the final magnetic properties will be presented.

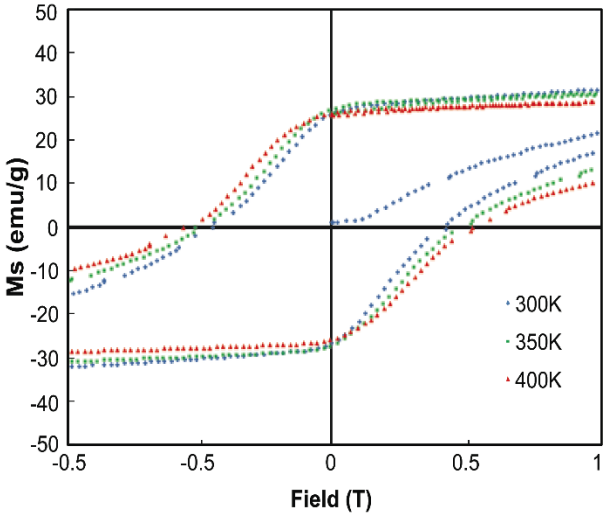

Figure 59. Temperature dependent M-H loops of MnBi.

4.4.2 Formation of MnBi Nanoalloys

Within the metal redox strategy, a zero-valent metal and a metal salt is needed. In this unique synthesis $Mn_2(CO)_{10}$ was chosen as the zero-valent source and Bismuth (III) neodecanoate was used as the metal salt. This synthesis showed the most synthetic control of all of the metal redox synthesis attempted, requiring the most care and optimization. This is due to the vast differences in the reduction potential, the difficulty of the alloying process and the properties of the precursors. To gain a complete understanding of the alloy formation aliquots were taken throughout the reaction to examine growth. A temperature of 240 °C is used for the hot-injection reaction. Upon injection of the $Mn_2(CO)_{10}$ into the Bi precursor, rapid reduction of the Bi is observed, and within 2 minutes into the reaction Bi spheres are seen in Figure 60a. No manganese is present in the particles at this time, as the decomposition temperature of $Mn_2(CO)_{10}$ in ODE is ~220 °C, which can be visualized by release of CO gas from the reaction. Since the temperature of the reaction dropped during the injection, $Mn_2(CO)_{10}$ has not

decomposed yet. Once the temperature has recovered to 240 °C, Mn can be seen to start to penetrate into the Bi spheres at 10 minutes into the reaction (Figure 60b). It is also

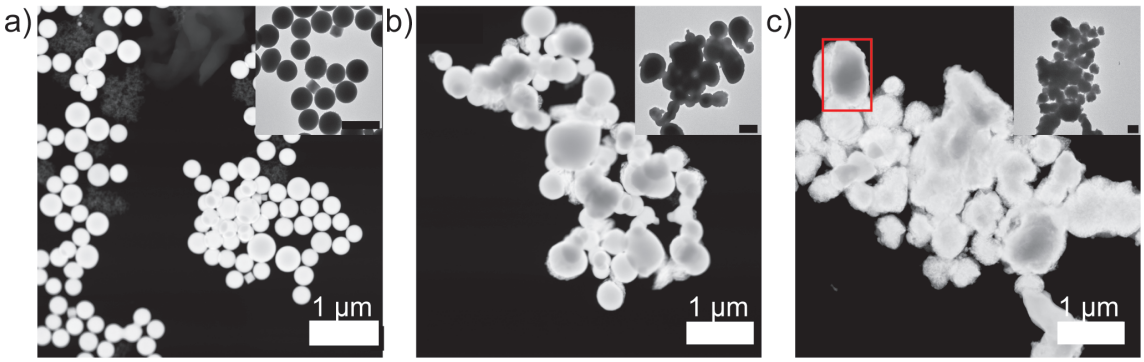

Figure 60. STEM images of a) Starting Bi particles formed after rapid reduction, b) MnBi particles after 10 min into reaction, displaying manganese forming around the Bi, and c) final MnBi particles at 60 min. Red box highlights pure Bi phase in the particles. Inset scale bars of TEM images 1 µm.

important to bring attention to the Bi spheres starting to meld together, likely due to softening of the bismuth as they are near the melting temperature of bismuth (270 °C). Finally, after an hour of reaction time at 240 °C the MnBi nanoalloys are produced, shown in Figure 60c. Pure Bi sections can still be observed (marked with a red square) within the particles, which correspond to the Bi diffraction seen in the XRD.

With this synthesis exhibiting such complexity between the balance of reduction and decomposition of the precursors, the temperature ramp rate heavily effects the final particles shape. Using a fast ramp rate of 13.3 degree/min, millimeter sized spheres with a shiny metallic surface are created, as seen in Figure 61b. Two different reasons rationalize the large solid sphere formation. First, the fast ramp rate reaches the decomposition temperature of $Mn_2(CO)_{10}$ quickly, creating higher concentrations of Mn^0

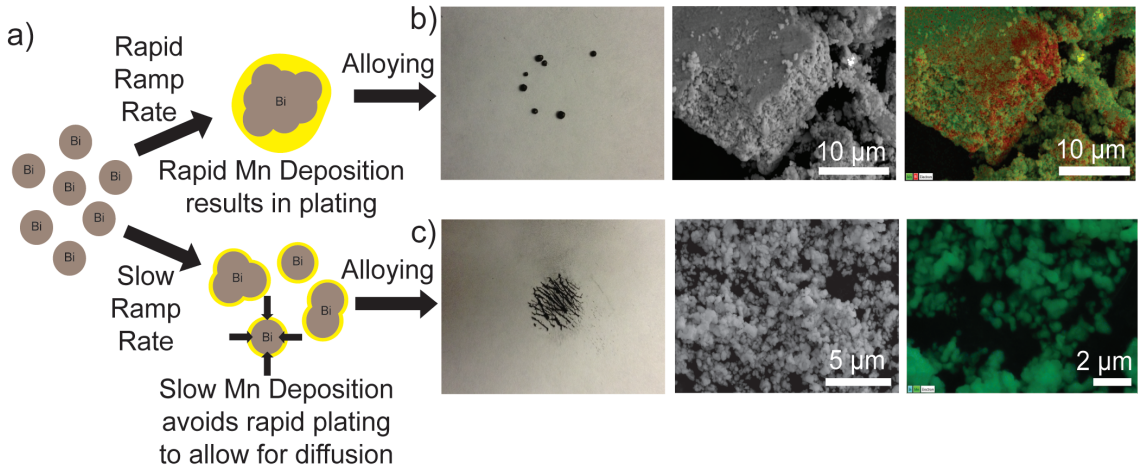

Figure 61. a) Scheme displaying different proposed particle formation pathways. b,c) MnBi particles with accompanying SEM/Elemental mapping created with (b) high ramp rate and (c) slow ramp rate.

monomers. Secondly, the higher ramp rate induces quicker Bi sphere merging. The combination of both of these creates large Bi masses and the high concentration of Mn monomers deposits rapidly onto the surface, blocking diffusion of other Mn. To confirm this formation mechanism, large particles were imaged under SEM shown in Figure 61b. The large particles display a smooth surface, being much different from the small rough particles shown in STEM above. Elemental mapping also shows high Mn concentration on the surface, with a Bi rich core. Finally, XPS of the large spheres show a high manganese counts when compared to Bi, confirming this type of formation (Figure 62). When the ramp rate is reduced to 5.7 degree/min, a black powder composed of well-alloyed nano structures are produced. With the slower ramp rate, there is a compromise between the manganese monomer production and merging of the bismuth nanospheres,

allowing for better alloying of the two metals. To produce the optimal nanoalloys, it was determined that 5.7 degree/min ramp rate was ideal.

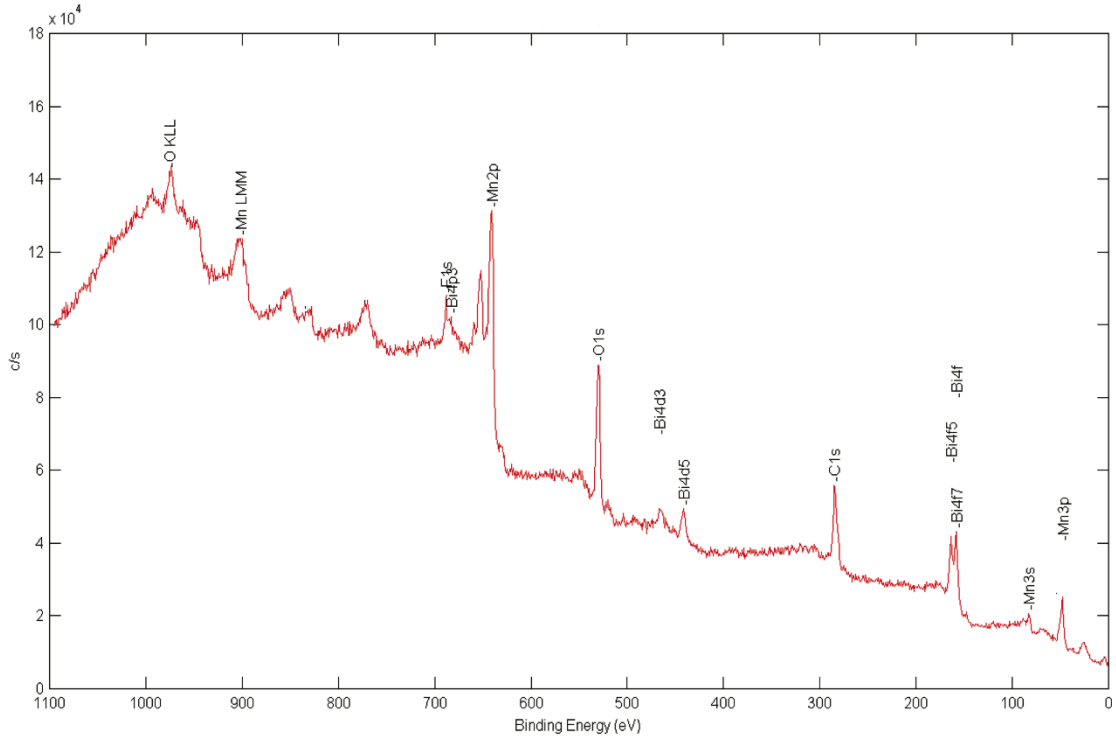

Figure 62. XPS spectrum of large MnBi particles produced with high ramp rate.

4.4.3 Precursor Loading and Reaction Temperature Effects on MnBi Nanoalloy

Stoichiometry of initial precursors, specifically $Mn_2(CO)_{10}$ also plays a vital role in controlling the magnetic performance of the final MnBi nanoalloys. $Mn_2(Co)_{10}$ is used in excess in this synthesis when compared to the other metal redox methods. Larger amounts are required due to $Mn_2(CO)_{10}$ subliming at lower temperature than its decomposition temperature, so some precursor is lost to sublimation on the walls of the reaction vessel. Also not all of the Mn is doped into the initial bismuth spheres, as small particles of manganese particles are seen at the end of the reaction. These excess

manganese particles are removed during the magnetic separation step. To study the effects of this precursor loss to other competitive mechanisms, reactions with varying Mn:Bi molar amounts were studied. M-H loops of the final MnBi nanoalloys with

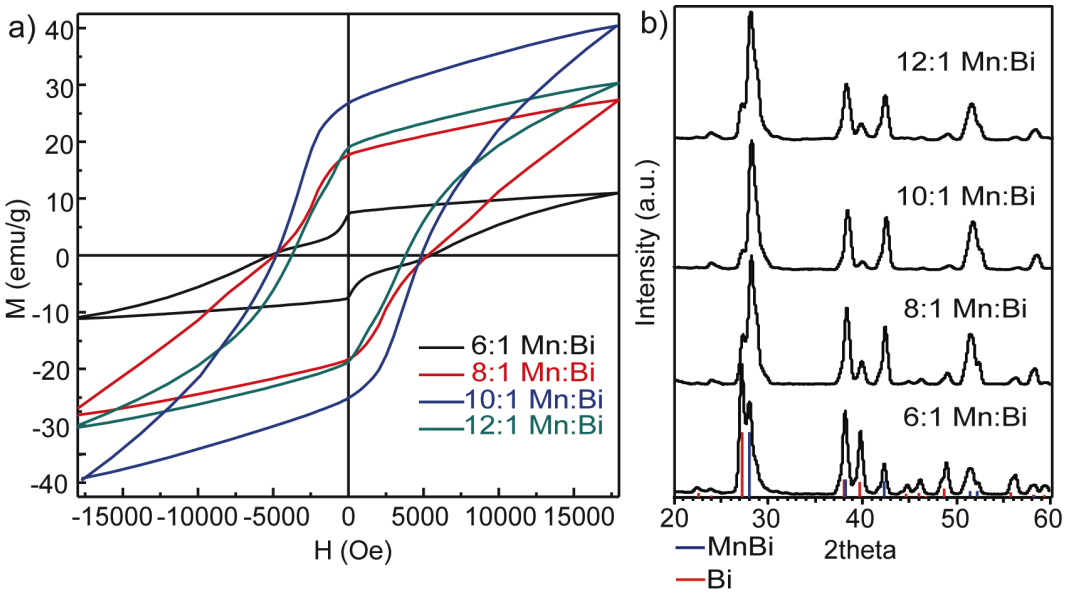

Figure 63. a) M-H loops of MnBi nanoalloys dependent on precursor loading. b) XRD of MnBi alloys dependent of stoichiometry.

different molar ratios are presented in Figure 63a. When using the lowest 6:1 Mn:Bi ratio, the particles only exhibit a M_s of 11 emu/g. XRD presented in Figure 63b shows very high Bi diffraction within this sample, explaining the lower M_s. Once the ratios are raised to 8:1 and 10:1 Mn:Bi the M_s increases to 27 emu/g and 40 emu/g respectively. XRD shows less Bi phase in these samples, indicating that the Bi phase is indeed responsible for the lower M_s than bulk MnBi. When increasing the ratio to 12:1, the M_s drops back down to 31 emu/g most likely due to increased Mn concentration starting to inhibit alloying by depositing on the surface too quickly, much like above in the rapid ramp rate

studies. An optimized stoichiometry is determined to be a 10:1 Mn:Bi molar ratio, producing high quality MnBi nanoalloys.

Temperature of the reaction also played a vital role in proper MnBi nanoalloy formation. Various reaction temperatures were studied to examine their effect on the final magnetic properties of the MnBi. Figure 64a displays the M-H loops of the MnBi particles created using a 10:1 Mn:Bi molar ratio. XRD of each of the nanoalloys are presented in Figure 64b. At 230 °C, a relatively high M_s is made, but coercivity is low, indicative of poor annealing throughout the particles. When the temperature is raised to 240 °C, particles with the highest M_s and H_c are produced, indicating this temperature allows an ideal balance between decomposition and alloying processes. Upon further increase of temperature the M_s of the particles rapidly drops off, with saturations of 28 emu/g, 18 emu/g and 12 emu/g for 250 °C, 260 °C and 270 °C temperatures respectively.

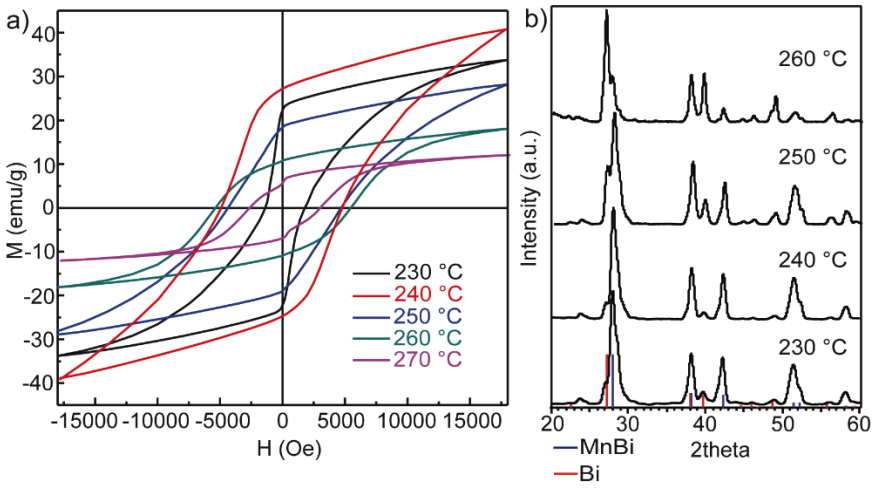

Figure 64. a) M-H loops of MnBi nanoalloys dependent on reaction temperature. b) XRD of MnBi nanoalloys with different reaction temperatures.

To confirm this temperature dependence, the same temperatures were used for a 8:1 Mn:Bi with the same results found in Figure 65. This indicates that the higher reaction temperatures does not allow for proper alloying of the MnBi phase. These results show that care must be taken to control ramp rate, stoichiometry of precursors and reaction temperatures to produce high quality MnBi alloys.

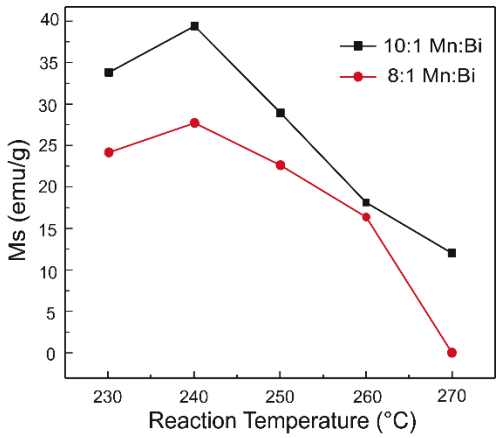

Figure 65. Graph of M_s values obtained with different stoichiometry and reaction temperatures.

4.5 Conclusion

In conclusion, a new synthetic strategy to synthesize nanoalloy particles deemed metal redox is presented. This strategy utilizes the inherent reducing power of zero-valent metal molecules to reduce metal salts, achieving nanoalloys without the use of ligands or excess harsh reducing agents. Its versatility is shown by the creation of many different bi-metallic nanoalloys, and can be expanded to many more systems. Stoichiometry of the final particles can be easily controlled by both precursor loading amounts and temperature to manipulate the equilibrium constant of the redox reaction. Tri-metallic alloys are also achievable, which open the door to studies of many different magnetic or catalytic applications. Reactions with lower spontaneity (Ecell < 0), it is also shown that

thermal energy can be used to push a non-spontaneous reaction backwards, allowing for even more alloy systems to use this method. If needed, reducing ligands can also be used to an extent to help control stoichiometry, and stabilizing ligands have been shown to not completely disrupt the redox reactions, allowing for size control. Finally, MnBi nanoalloys have been created for the first time via solution processing utilizing the metal redox strategy. The magnetic properties of the MnBi alloys exhibit near bulk properties after optimization, making this a promising, scalable method to create MnBi for practical high temperature hard magnet applications.

4.6 Materials and Methods

Standard Schlenk-line synthesis was used, first loading 8 mL of ODE (degassed with argon) was loaded into a 3-neck round bottom flask that has been through 3 vacuum/purge cycles with argon. This flask was heated to desired temperature for injection. While heating, air-tight vials with septum were loaded with the desired pre-cursors. For the metal salts, 0.25 mmol was loaded and then dissolved in 2 mL of ODE and this solution was then bubbled with argon for 10 min. The vial is then heated to 85 °C to help solubility of the metal salt. Same treatment was used for all of the zero-valent metal precursors (except for $Fe(CO)_5$ which was used neat, and the $Mn_2(CO)_{10}$ that is described later). Once desired temperature was reached in the 3-neck flask, both precursor solutions were injected into the hot solution (making sure to have the back bubbler open to release any gas formation). The reaction was then allowed sit at desired reaction temperature for 1 hour. After this time, the solutions were cooled to room temperature and cleaned via centrifugation at 4000 rpms for 10 min with toluene/acetone mixture. This wash was repeated 2 more times. Samples are then either dried or re-

dissolved in toluene, depending on characterization desires, and moved to a nitrogen drybox for storage. All annealing processes were done at 550 °C and in a 10/90 H_2/N_2 atmosphere for 4 hours, except for the FeGa case, where 12 hours was needed to generate desired crystallinity. An important note, the pre-annealed NiPd and NiPt samples auto-ignited in air, so care should be used when handling these alloys.

In the case of FeGa synthesis, if TOPO or oleylamine was used, the proper amount was loaded into the initial 3-neck flask with the ODE. For MnBi synthesis, $Mn_2(CO)_{10}$ locks up the syringe during injection, so a hot cannula transfer was required. To do this, a second 3 neck flask was loaded with proper amount of $Mn_2(CO)_{10}$ and then the flask is subjected to 3 vacuum/purge cycles with argon. 4 mL of ODE was then loaded, and the flask was heated to 100 °C to dissolve all of the $Mn_2(CO)_{10}$. A large-bore cannula was extensively heated to avoid clogging and then rapidly used to cannula transfer the $Mn_2(CO)_{10}$ solution into the ODE containing flask, then the bismuth precursor is injected. In the case of the bismuth precursor, it was not heated on a hotplate as it formed a solution ODE readily, and it needed to be room temperature to get the proper temperature drop desired at injection.

The iron-nickel nanoparticles were analyzed for both iron and nickel content using ICP-AES. The solid reaction material was centrifuged down and supernatant decanted off. The individual samples were then digested at 90^{o}C in concentrated high purity nitric acid for 3.0 hours and then allowed to stand for 12 hours prior to analysis. Samples were then diluted using high purity water and 7% nitric acid solution to a final volume with final nitric acid concentration at 5% nitric acid. Standards were prepared from a commercially purchased prepared mixed standard containing iron and nickel at

approximately 1000ug/mL each (Inorganic Ventures). Standards were prepared in the working range from 1 to 100ug/mL. The instrument was operated in the radial mode with a 20 second sample time and Automax for wavelength and S/N optimization. Flow rate was set at 1.0mL/min and samples were randomized for run order. Samples were then analyzed using the best fit calibration line and all results reported as µg/mL of the solution. Original concentrations were then calculated based on sample volumes and comparative mole ratios.

In the catalytic measurements 1 mg of catalyst was sonicated into 20 mL of an aqueous 1.4 $x10^{-4}$ M P-Nitrophenol solution and 32 mg of sodium borohydride was added (creating a 4.2 $x10^{-2}$ M concentration) and immediately transferred to cuvette for absorbance measurements. Measurements were repeated 5 times for each synthesis. For recycling studies, a strong magnet was held up to the solution to separate all the catalyst and washed with water to remove any excess sodium borohydride or product. A new solution is then added and the measurement repeated.

Room temperature X-ray powder patterns were obtained on a Bruker proteum diffraction system equipped with Helios multilayer optics, an APEX II CCD detector and a Bruker MicroStar microfocus rotating anode X-ray source operating at 45 kV and 60 mA. Transmission electron microscope (TEM) images were obtained using a Field emission FEI Tecnai F20 XT. Scanning electron microscope (SEM) images were obtained on a FEI Versa 3D Dual Beam. ICP-AES was done on a Varian (Agilent) 725 ICP-AES with a peristaltic pump, autosampler, computer and software. The magnetic hysteresis (M-H) loops were taken on a Microsense EZ7 vibrating sample magnetometer.

A MTI GSL-1100X tube furnace was used for reductive sintering. Absorbance measurements were taken on a Cary 100 Bio UV-Vis spectrophotometer.

5 Conclusion and Outlook

In conclusion, I have shown novel nanosynthesis of different iron-based materials to further their use in green renewable-energy applications. In the second chapter the nanosynthesis and discussion on the earth-abundant, non-toxic semiconductor Iron Pyrite was presented. Shape control of the FeS_2 nanoparticles was achieved simply by modifying the injection temperature and iron precursor. It was discovered that the {100} surface was more active and stable for a basic photocatlytic reaction when compared to the {111} surface. Upon closer investigation of particle formation, it was found that the FeS_2 nanoparticles did not grow by the standard Ostwald ripening mechanism. In fact, the orientated attachment pathway was observed for all FeS_2 crystal shapes obtained. Taking advantage of this growth mechanism, the achievable shapes for FeS_2 nanoparticles was expanded. Not only were more shapes realized, but the ability to tune the size and crystallinity of the final Iron Pyrite nanoparticles was also accomplished. However, defects are an inherent result from orientated attachment, which lead to the development of a method to create high quality micron-sized Iron Pyrite crystals with a solid-state sulfurization of a novel FeS nanowire precursor. The dominant growth direction of the large FeS_2 crystals could be readily controlled by both sulfurization temperature and time. These high quality Iron Pyrite crystals show promise for in-depth characterization to further elucidate the issues that have deterred FeS_2 from realizing it's potential as a cheap non-toxic semiconductor. Further work should be focused on mitigation of defects within the FeS_2 nanocrystals. If the issue for pyrite's poor performance is due to surface defects, it may prove valuable to coat the surface with another proper semiconductor.

This could simultaneously passivate the defect sites, while creating a donor-acceptor junction allowing for separation of generated exitons. If the problem lies within the particles, due to internal defects or improper phase formation, a method to overcome these obstacles must be created. To achieve a better understanding of the problems pyrite faces, the Pyrite field should focus on the extensive study of high quality Pyrite crystals to determine the exact problem. If these issues could be addressed, the Pyrite material system could prove extremely valuable to solar cell energy generation.

Within the third chapter, a new synthetic strategy for the generation of FePd nanoparticles was achieved via interdiffusion of Fe into Pd nanocores. Upon further addition of Fe above the 1:1 stoichiometric ratio, a Fe_2O_3 shell could be deposited. These FePd/Fe_2O_3 core/shell particles provided an excellent foundation to create an exchange-coupled $L1_0$FePd/α-Fe nanocomposite that presented superior magnetic properties than its single phased FePd counterpart. However, due to the stabilizing phosphine ligand required for size control, a FeP_2 phase was observed to form which lead to the degradation of the final magnetic properties. Future work for this system should be focused on replacing the phosphine ligand with a suitable ligand that will provide the required control for generation of well-optimized nanocomposites. Moreover, controlling the critical annealing step of the nanoparticles to produce the exchange-coupled nanocomposite should be investigated. A method to quickly reduce the Fe_2O_3 and convert the FePd to $L1_0$ ordering could prove advantageous to avoid the merging into larger size domains. Quenching or matrix annealing methods may be able to achieve superior magnetic results for the nanocomposites. This synthetic method provides a valuable step

on the way to creating new powerful magnetic systems for the use in green energy applications.

Finally, in the fourth chapter a new synthetic strategy was developed to overcome known issues within general nanoparticle synthesis. The Metal Redox method makes use of the inherent reducing power of zero-valent metals to reduce metal salts, generating nanoalloys. In utilizing the zero-valent metal reduction, the need for excess reducing agents and ligands are eliminated. Many different metal alloy systems were shown to be obtainable, proving the versatility of this method. The stoichiometry of the final alloys could be controlled by temperature and easily explained with simple equilibrium concepts. Tri-metallic alloys were also achieved and yielded intriguing results in magnetic and catalytic performance. To provide additional utility to the method, it was found that non-spontaneous reactions could be thermally pushed forward to generate alloy systems. Moreover, extra reducing power and stabilizing ligands were shown to help tune stoichiometry and size where applications require it. Finally, a MnBi nanoalloy with near magnetic bulk properties was created for the first time via solution processing. The MnBi alloy's magnetic properties were be modified by reaction temperature, ramp rate, and initial precursor stoichiometry. The introduction of the Metal Redox methodology could be expanded to control nanoalloys and find uses in many different practical applications. More extensive sampling of nanoalloys could be generated including Au, Ag, and Cu systems. Van't Hoff plots then could be generated for these alloys, providing a comprehensive guide to other researchers for the facile generation of ligandless nanoalloy systems. Trimetallic alloys could prove interesting to examine for cooperative catalytic effects to improve performance. The hard magnetic MnBi

nanoalloys could be coated with a soft magnetic system such as Co or FeCo generating a high-energy density nanocomposite without the need for RE elements, which could help lower the cost of green energy.

6 List of Publications

A.Kirkeminde, S. Spurlin, L. Draxler-Sixta, J. Cooper, S. Ren, *Angewandte Chemie International Edition*, 2015**, 54**, 4203.

A. Kirkeminde, S. Ren, *Nano Letters*, 2014**, 14***,* 4493.

A. Kirkeminde, P. Gingrich, M. Gong, H. Cui, S. Ren, "Iron Sulfide Ink for the Growth of Pyrite Crystals", *Nanotechnology*, 2014, **25**, 205603.

A. Kirkeminde, M. Gong, S. Ren, *Scientific Reports*, 2013, **3**, 2092.

A. Kirkeminde, B. A. Ruzicka, R. Wang, S. Puna, H. Zhao and S. Ren, *ACS Applied Materials & Interfaces*, 2012, **4**, 1174.i

A. Kirkeminde and S. Ren, *Journal of Materials Chemistry A*, 2013, **1**, 49.

A. Kirkeminde, R. Scott, and S. Ren, *Nanoscale,* 2012, **4**, 7649.

M. Gong, A. Kirkeminde, M. Wuttig, S. Ren, *Nano Letters*, 2014, **14**, 6493.

M. Gong, A. Kirkeminde, R. Skomski, J. Cui, S. Ren, *Small*, 2014, **10**, 4118.

M. Gong, A. Kirkeminde, K. Nardeep, H. Zhao, S. Ren, *Chemical Communications*, 2013, **49**, 9260.

M. Gong, A. Kirkeminde, Y. Xie, R. Lu, J. Liu, J Wu, S. Ren, *Advanced Optical Materials*, 2013, **1**, 78.

8 Bibliography:

1. J. Goldemberg, *Science*, 2007, **315**, 808.
2. C. Baird and M. Cann, *Environmental Chemistry*, W.H. Freeman and Company, New York, 2008.
3. A. Kojima, K. Teshima, Y. Shirai and T. Miyasaka, *Journal of the American Chemical Society*, 2009, **131**, 6050.
4. C. Wadia, A. P. Alivisatos and D. M. Kammen, *Environmental Science & Technology*, 2009, **43**, 2072.
5. W. Musial, S. Butterfield and B. McNiff, in *European Wind Energy Conference, Milan, Italy*, 2007, pp. 7.
6. W. D. Callister and D. G. Rethwisch, *Materials Science and Engineering: An Introduction*, Wiley, 2013.
7. J. P. Liu, E. Fullerton, O. Gutfleisch and D. J. Sellmyer, *Nanoscale Magnetic Materials and Applications*, Springer US, 2009.
8. W. M. Haynes, *CRC Handbook of Chemistry and Physics*, CRC Press, 2014.
9. K. R. Long, B. S. Van Gosen, N. K. Foley and D. Cordier, ed. U. S. G. Survey, 2010, p. 96.
10. L. Brus, *The Journal of Physical Chemistry*, 1986, **90**, 2555.
11. D. V. Talapin, J.-S. Lee, M. V. Kovalenko and E. V. Shevchenko, *Chemical Reviews*, 2009, **110**, 389.
12. W. U. Huynh, J. J. Dittmer and A. P. Alivisatos, *Science*, 2002, **295**, 2425.
13. N. C. Greenham, X. Peng and A. P. Alivisatos, *Physical Review B*, 1996, **54**, 17628.
14. S. Günes, H. Neugebauer and N. S. Sariciftci, *Chemical reviews*, 2007, **107**, 1324.
15. I. Gur, N. A. Fromer, M. L. Geier and A. P. Alivisatos, *Science*, 2005, **310**, 462.
16. G. I. Koleilat, L. Levina, H. Shukla, S. H. Myrskog, S. Hinds, A. G. Pattantyus-Abraham and E. H. Sargent, *ACS Nano*, 2008, **2**, 833.
17. E. H. Sargent, *Advanced Materials*, 2008, **20**, 3958.
18. W. Ma, J. M. Luther, H. Zheng, Y. Wu and A. P. Alivisatos, *Nano letters*, 2009, **9**, 1699.
19. P. Brown and P. V. Kamat, *Journal of the American Chemical Society*, 2008, **130**, 8890.
20. I. Robel, V. Subramanian, M. Kuno and P. V. Kamat, *Journal of the American Chemical Society*, 2006, **128**, 2385.
21. R. Vogel, P. Hoyer and H. Weller, *The Journal of Physical Chemistry*, 1994, **98**, 3183.
22. X. R. Wang, Z. Z. Sun and J. Lu, in *Nanoscale Magnetic Materials and Applications*, eds. J. P. Liu, E. Fullerton, O. Gutfleisch and D. J. Sellmyer, Springer US, 2009, pp. 1.
23. R. P. Cowburn, in *Nanoscale Magnetic Materials and Applications*, eds. J. P. Liu, E. Fullerton, O. Gutfleisch and D. J. Sellmyer, Springer US, 2009, pp. 219.
24. C. Bárcena, A. Sra and J. Gao, in *Nanoscale Magnetic Materials and Applications*, eds. J. P. Liu, E. Fullerton, O. Gutfleisch and D. J. Sellmyer, Springer US, 2009, pp. 591.

25. Y.-w. Jun, J.-w. Seo and J. Cheon, *Accounts of Chemical Research*, 2008, **41**, 179.
26. J. P. Liu, in *Nanoscale Magnetic Materials and Applications*, eds. J. P. Liu, E. Fullerton, O. Gutfleisch and D. J. Sellmyer, Springer US, 2009, pp. 309.
27. H. Zeng, J. Li, J. P. Liu, Z. L. Wang and S. Sun, *Nature*, 2002, **420**, 395.
28. V. K. LaMer and R. H. Dinegar, *Journal of the American Chemical Society*, 1950, **72**, 4847.
29. C. B. Murray, C. R. Kagan and M. G. Bawendi, *Annual Review of Materials Science*, 2000, **30**, 545.
30. R. L. Penn and J. F. Banfield, *Science*, 1998, **281**, 969.
31. R. L. Penn, *Journal of Physical Chemistry B*, 2004, **108**, 12707.
32. C. J. Dalmaschio, C. Ribeiro and E. R. Leite, *Nanoscale*, 2010, **2**, 2336.
33. J. F. Banfield, S. A. Welch, H. Zhang, T. T. Ebert and R. L. Penn, *Science*, 2000, **289**, 751.
34. C. B. Murray, D. J. Norris and M. G. Bawendi, *Journal of the American Chemical Society*, 1993, **115**, 8706.
35. Z. A. Peng and X. G. Peng, *Journal of the American Chemical Society*, 2001, **123**, 183.
36. Z. A. Peng and X. G. Peng, *Journal of the American Chemical Society*, 2001, **123**, 1389.
37. Z. A. Peng and X. G. Peng, *Journal of the American Chemical Society*, 2002, **124**, 3343.
38. A. L. Rogach, T. Franzl, T. A. Klar, J. Feldmann, N. Gaponik, V. Lesnyak, A. Shavel, A. Eychmüller, Y. P. Rakovich and J. F. Donegan, *The Journal of Physical Chemistry C*, 2007, **111**, 14628.
39. J. Turkevich, P. C. Stevenson and J. Hillier, *Discussions of the Faraday Society*, 1951, **11**, 55.
40. P. K. Jain, X. Huang, I. H. El-Sayed and M. A. El-Sayed, *Accounts of Chemical Research*, 2008, **41**, 1578.
41. M. E. Stewart, C. R. Anderton, L. B. Thompson, J. Maria, S. K. Gray, J. A. Rogers and R. G. Nuzzo, *Chemical Reviews*, 2008, **108**, 494.
42. X. Lu, M. Rycenga, S. E. Skrabalak, B. Wiley and Y. Xia, *Annual Review of Physical Chemistry*, 2009, **60**, 167.
43. E. V. Shevchenko, D. V. Talapin, H. Schnablegger, A. Kornowski, Ö. Festin, P. Svedlindh, M. Haase and H. Weller, *Journal of the American Chemical Society*, 2003, **125**, 9090.
44. J. Emsley, *Nature's Building Blocks: An A-Z Guide to the Elements*, Oxford University Press, USA, 2011.
45. P. Chapman and F. Roberts, *Metal Resources and Energy*, Buttersworths, London, 1983.
46. A. Ennaoui and H. Tributsch, *Solar Cells*, 1984, **13**, 197.
47. A. Ennaoui, S. Fiechter, C. Pettenkofer, N. Alonsovante, K. Buker, M. Bronold, C. Hopfner and H. Tributsch, *Solar Energy Materials and Solar Cells*, 1993, **29**, 289.
48. R. Sun, M. K. Y. Chan and G. Ceder, *Physical Review B*, 2011, **83**.

49. L. Yu, S. Lany, R. Kykyneshi, V. Jieratum, R. Ravichandran, B. Pelatt, E. Altschul, H. A. S. Platt, J. F. Wager, D. A. Keszler and A. Zunger, *Advanced Energy Materials*, 2011, **1**, 748.
50. M. Bronold, Y. Tomm and W. Jaegermann, *Surface Science*, 1994, **314**, L931.
51. M. Cabán-Acevedo, N. S. Kaiser, C. R. English, D. Liang, B. J. Thompson, H.-E. Chen, K. J. Czech, J. C. Wright, R. J. Hamers and S. Jin, *Journal of the American Chemical Society*, 2014, **136**, 17163.
52. A. S. Barnard and S. P. Russo, *The Journal of Physical Chemistry C*, 2007, **111**, 11742.
53. A. S. Barnard and S. P. Russo, *Journal of Materials Chemistry*, 2009, **19**, 3389.
54. S. Fiechter, J. Mai, A. Ennaoui and W. Szacki, *Journal of Crystal Growth*, 1986, **78**, 438.
55. J. G. Fleming, *Journal of Crystal Growth*, 1988, **92**, 287.
56. T. A. Bither, R. J. Bouchard, W. H. Cloud, P. C. Donohue and W. J. Siemons, *Inorganic Chemistry*, 1968, **7**, 2208.
57. G. Chatzitheodorou, S. Fiechter, R. Konenkamp, M. Kunst, W. Jaegermann and H. Tributsch, *Materials Research Bulletin*, 1986, **21**, 1481.
58. C. Wadia, Y. Wu, S. Gul, S. K. Volkman, J. Guo and A. P. Alivisatos, *Chemistry of Materials*, 2009, **21**, 2568.
59. D. Wang, Q. Wang and T. Wang, *Crystengcomm*, 2010, **12**, 3797.
60. X. Chen, Z. Wang, X. Wang, J. Wan, J. Liu and Y. Qian, *Inorganic Chemistry*, 2005, **44**, 951.
61. H. A. Macpherson and C. R. Stoldt, *ACS Nano*, 2012, **6**, 8940.
62. B. Yuan, W. Luan and S.-t. Tu, *Dalton Transactions*, 2012, **41**, 772.
63. N. Poudyal, G. S. Chaubey, C. Rong and J. P. Liu, *Journal of Applied Physics*, 2009, **105**, 07A749.
64. J. Puthussery, S. Seefeld, N. Berry, M. Gibbs and M. Law, *Journal of the American Chemical Society*, 2010, **133**, 716.
65. A. Kirkeminde and S. Ren, *Journal of Materials Chemistry A*, 2013, **1**, 49.
66. J. H. L. Beal, P. G. Etchegoin and R. D. Tilley, *Journal of Solid State Chemistry*, 2012, **189**, 57.
67. J. T. Zhang, Y. Tang, K. Lee and O. Y. Min, *Science*, 2010, **327**, 1634.
68. A. Kirkeminde, B. Ruzicka, R. Wang, S. Puna, H. Zhao and S. Q. Ren, *ACS Applied Materials & Interfaces*, 2012, **3**. 1174..
69. P. Sullivan, J. Yelton and K. Reddy, *Environmental Geology*, 1988, **11**, 289.
70. J. M. Guevremont, D. R. Strongin and M. A. Schoonen, *American Mineralogist*, 1998, **83**, 1246.
71. J. Zhang, F. Huang and Z. Lin, *Nanoscale*, 2010, **2**, 18.
72. R. L. Penn and J. F. Banfield, *American Mineralogist*, 1999, **84**, 871.
73. R. L. Penn, G. Oskam, T. J. Strathmann, P. C. Searson, A. T. Stone and D. R. Veblen, *The Journal of Physical Chemistry B*, 2001, **105**, 2177.
74. P. D. Cozzoli, M. L. Curri, A. Agostiano, G. Leo and M. Lomascolo, *The Journal of Physical Chemistry B*, 2003, **107**, 4756.
75. C. Ricolleau, L. Audinet, M. Gandais and T. Gacoin, *European Physical Journal D*, 1999, **9**, 565.

76. M. Klokkenburg, A. J. Houtepen, R. Koole, J. W. J. de Folter, B. H. Erné, E. van Faassen and D. Vanmaekelbergh, *Nano Letters*, 2007, **7**, 2931.
77. X. Wen, Y.-T. Xie, W. C. Mak, K. Y. Cheung, X.-Y. Li, R. Renneberg and S. Yang, *Langmuir*, 2006, **22**, 4836.
78. A. Halder and N. Ravishankar, *Advanced Materials*, 2007, **19**, 1854.
79. J. P. Wilcoxon, P. P. Newcomer and G. A. Samara, *Solid State Communications*, 1996, **98**, 581.
80. M. Gong, A. Kirkeminde and S. Ren, , *Scientific Reports*, 2013, **3**.
81. C. Schliehe, B. H. Juarez, M. Pelletier, S. Jander, D. Greshnykh, M. Nagel, A. Meyer, S. Foerster, A. Kornowski, C. Klinke and H. Weller, *Science*, 2010, **329**, 550.
82. S. Seefeld, M. Limpinsel, Y. Liu, N. Farhi, A. Weber, Y. Zhang, N. Berry, Y. J. Kwon, C. L. Perkins, J. C. Hemminger, R. Wu and M. Law, *Journal of the American Chemical Society*, 2013, **135**, 4412.
83. M. Limpinsel, N. Farhi, N. Berry, J. Lindemuth, C. L. Perkins, Q. Lin and M. Law, *Energy & Environmental Science*, 2014, **7**, 1974.
84. C. Steinhagen, T. B. Harvey, C. J. Stolle, J. Harris and B. A. Korgel, *Journal of Physical Chemistry Letters*, 2012, **3**, 2352.
85. D. Rickard and G. W. Luther, III, *Chemical Reviews*, 2007, **107**, 514.
86. X. Y. Chen, J. R. Li, L. Jiang, X. Y. Chen and J. R. Li, *Nanotechnology*, 2000, **11**, 108.
87. C. Yue, L. Zhang, S. Liao and H. Gao, *Journal of Materials Engineering and Performance*, 2010, **19**, 112.
88. C. Höpfner, K. Ellmer, A. Ennaoui, C. Pettenkofer, S. Fiechter and H. Tributsch, *Journal of Crystal Growth*, 1995, **151**, 325.
89. R. Skomski and J. M. D. Coey, *Physical Review B*, 1993, **48**, 15812.
90. N. Sakuma, T. Ohshima, T. Shoji, Y. Suzuki, R. Sato, A. Wachi, A. Kato, Y. Kawai, A. Manabe and T. Teranishi, *ACS Nano*, 2011, **5**, 2806.
91. T. Teranishi, A. Wachi, M. Kanehara, T. Shoji, N. Sakuma and M. Nakaya, *Journal of the American Chemical Society*, 2008, **130**, 4210.
92. Y. Yu, K. Sun, Y. Tian, X. Z. Li, M. J. Kramer, D. J. Sellmyer, J. E. Shield and S. Sun, *Nano Letter*, 2013, **13**, 4975.
93. A. Dong, J. Chen, P. M. Vora, J. M. Kikkawa and C. B. Murray, *Nature*, 2010, **466**, 474.
94. A. Dong, Y. Jiao and D. J. Milliron, *ACS Nano*, 2013, **7**, 10978.
95. Y. Hou, H. Kondoh, T. Kogure and T. Ohta, *Chemistry of Materials*, 2004, **16**, 5149.
96. S. Kang, Z. Jia, D. E. Nikles and J. W. Harrell, *Journal of Applied Physics*, 2004, **95**, 6744.
97. Z. Yang and K. J. Klabunde, *Journal of Organometallic Chemistry*, 2009, **694**, 1016.
98. C. Wang, S. Peng, L.-M. Lacroix and S. Sun, *Nano Research*, 2009, **2**, 380.
99. A. Kirkeminde and S. Ren, *Nano Letter*, 2014, **14**, 4493.
100. C. J. Smithells, *Smithells Metal Reference Book*, Butterworth-Heinemann, Oxford, 1992.

101. J. Park, B. Koo, K. Y. Yoon, Y. Hwang, M. Kang, J.-G. Park and T. Hyeon, *Journal of the American Chemical Society*, 2005, **127**, 8433.
102. H. Zeng, J. Li, Z. L. Wang, J. P. Liu and S. Sun, *Nano Letter*, 2003, **4**, 187.
103. D. Li, C. Wang, D. Tripkovic, S. Sun, N. M. Markovic and V. R. Stamenkovic, *ACS Catalysis*, 2012, **2**, 1358.
104. J.-I. Park and J. Cheon, *Journal of the American Chemical Society*, 2001, **123**, 5743.
105. W.-r. Lee, M. G. Kim, J.-r. Choi, J.-I. Park, S. J. Ko, S. J. Oh and J. Cheon, *Journal of the American Chemical Society*, 2005, **127**, 16090.
106. D. Chen, J. Li, C. Shi, X. Du, N. Zhao, J. Sheng and S. Liu, *Chemistry of Materials*, 2007, **19**, 3399.
107. M. Bersani, L. Conte, A. Martucci, M. Guglielmi, G. Mattei, V. Bello, R. Rosei and M. Centazzo, *Nanoscale*, 2014, **6**, 1560.
108. A. Kirkeminde, S. Spurlin, L. Draxler-Sixta, J. Cooper and S. Ren, 2015, *Angewandte Chemie International Edition,* 2015, **DOI: 10.1002/anie.201411460**
109. R. L. Moss, D. Pope and H. R. Gibbens, *Journal of Catalysis*, 1977, **46**, 204.
110. J. Ahmed, S. Sharma, K. V. Ramanujachary, S. E. Lofland and A. K. Ganguli, *Journal Colloid Interface Science*, 2009, **336**, 814.
111. T. Horiuchi, M. Igarashi, F. Abe, K. Ohkubo, S. Miura and T. Mohri, *Metallurgical and Materials Transactions A*, 2005, **36**, 1999.
112. W. Zhu, R. Michalsky, Ö. Metin, H. Lv, S. Guo, C. J. Wright, X. Sun, A. A. Peterson and S. Sun, *Journal of the American Chemical Society*, 2013, **135**, 16833.
113. M. Schrinner, M. Ballauff, Y. Talmon, Y. Kauffmann, J. Thun, M. Möller and J. Breu, *Science*, 2009, **323**, 617.
114. J. Zeng, Q. Zhang, J. Chen and Y. Xia, *Nano Letter*, 2009, **10**, 30.
115. B. Roberts, *Physical Review*, 1956, **104**, 607.
116. R. Heikes, *Physical Review*, 1955, **99**, 446.
117. P. A. Albert and W. J. Carr, *Journal of Applied Physics*, 1961, **32**, S201.
118. S. Saha, R. T. Obermyer, B. J. Zande, V. K. Chandhok, S. Simizu, S. G. Sankar and J. A. Horton, *Journal of Applied Physics*, 2002, **91**, 8525.
119. K. Koyama, T. Onogi, Y. Mitsui, Y. Nakamori, S.-i. Orimo and K. Watanabe, *Materials Transactions*, 2007, **48**, 2414.
120. J. B. Yang, W. B. Yelon, W. J. James, Q. Cai, S. Roy and N. Ali, *Journal of Applied Physics*, 2002, **91**, 7866.
121. J. B. Yang, W. B. Yelon, W. J. James, Q. Cai, M. Kornecki, S. Roy, N. Ali and l. H. Ph, *Journal of Physics: Condensed Matter*, 2002, **14**, 6509.